Nanostructured light metal hydride: Fabrication strategies and hydrogen storage performance

Yongfeng Liu[a,b,1]*, Wenxuan Zhang[a,1], Xin Zhang[a,1], Limei Yang[c], Zhenguo Huang[c], Fang Fang[d]**, Wenping Sun[a], Mingxia Gao[a], Hongge Pan[a,b]***

[a]State Key Laboratory of Silicon and Advanced Semiconductor Materials, Key Laboratory of Advanced Materials and Applications for Batteries of Zhejiang Province and School of Materials Science and Engineering, Zhejiang University, Hangzhou 310027, China.

[b]Institute of Science and Technology for New Energy, Xi'an Technological University, Xi'an, 710021, China.

[c]School of Civil & Environmental Engineering, University of Technology Sydney, 81 Broadway, Ultimo, NSW, 2007, Australia

[d]Department of Materials Science, Fudan University, Shanghai, 200433 China.

*Corresponding author.

**Corresponding authors.

***Corresponding authors.

Email: mselyf@zju.edu.cn (Y. F. L.); f_fang@fudan.edu.cn (F. F.); hgpan@zju.edu.cn (H.G.P.)

[1]These authors contributed equally to this work: Yongfeng Liu, Wenxuan Zhang and Xin Zhang.

Highlights

- Physical and chemical properties of light metal hydrides are discussed.
- Research advances in nanostructured light metal hydrides are summarized.
- Breakthroughs in nanoscaled MgH_2 and $LiBH_4$ are highlighted.
- Challenges and the future research directions are discussed.

Graphical Abstract

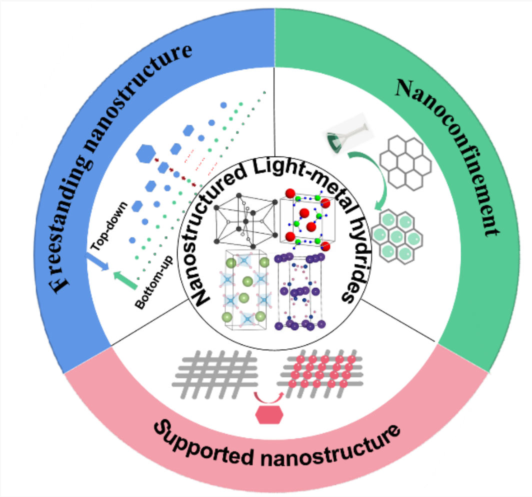

Word Count: ~ 14000 words for main text.

Nomenclature		RF	Radio frequency
		CNFs	Carbon nanofibers
Symbols		$MgBu_2$	Dibutylmagnesium
		rGO	Reduced graphene oxide
ΔG	Gibbs free energy	NCs	Nanocrystals
T	Temperature	NPs	Nanoparticles
P_{eq}	Plateau pressure	PMMA	Poly(methyl methacrylate)
ΔH	Changes in enthalpy	CNF_{ox}	Surface–oxidized carbon nanofiber
ΔS	Changes in entropy	GNs	Graphene nanosheets
R	Gas constant	MC	Mesoporous carbon
E_a	Activation energy	MOFs	Metal–organic framework
$\Delta_f H^0$	Standard formation enthalpy	AC	Activated carbon
χ_P	Pauling electronegativity	B_2H_6	Diborane
		CNC	Carbon nanocages
Abbreviations		MCHSs	Mesoporous carbon hollow spheres
		DLCB	Double-layered carbon bowl
PCIs	Pressure–composition isotherms	MTBE	Methyl tert–butyl ether
THF	Tetrahydrofuran	TGA	Thermogravimetric analysis
HPMR	Hydrogen plasma–metal reaction	FFT	Fast Fourier transform
HCVD	Hydriding chemical vapor deposition	BMAS	Ball milling with aerosol spraying

Abstract

Hydrogen can play an important role in the development of a sustainable energy system. However, storing hydrogen in a safe, efficient and economical manner remains a huge challenge. Light metal hydrides have attracted considerable attention for hydrogen storage owing to their high gravimetric and volumetric hydrogen densities. However, the strong covalent and/or ionic bonds between metal atoms and hydrogen result in slow kinetics, poor reversibility, and temperatures too high for dehydrogenation, hence delaying their practical large–scale applications. Considerable efforts have been toward tailoring the thermodynamic and kinetic properties of light metal hydride–based hydrogen storage materials for performance improvement, with the fabrication of nanoscale particles being a key and effective strategy. This review covers the preparation methods and hydrogen storage performance of nanostructured light metal hydrides. The physical and chemical properties and hydrogen storage behaviors of reversible light metal hydrides are first summarized, including MgH_2, borohydrides, aluminum hydrides, amide–hydride systems, and hydride composites. The second section focuses on the research progress in nanostructuring for enhancing the reversible hydrogen storage properties of these hydrides. Finally, the main challenges and the future research prospects are discussed. The combination of nanostructuring and nanocatalysis can significantly enhance the performance of these hydrides and make them practical hydrogen carriers.

Keywords: energy storage; hydrogen; metal hydrides; nanostructures; thermodynamics; kinetics

1. Introduction

Renewable energy with net-zero emissions is highly desirable for a clean and sustainable society [1–8]. Hydrogen, the lightest element in the universe, has the highest chemical energy density in mass (142 $MJ \cdot kg^{-1}$) among all the common fuels [1], consequently attracting intense interests as an ideal energy carrier. Moreover, hydrogen is abundant on Earth typically in combination with O and C, and it is pollution-free when used as a power fuel. However, hydrogen gas at ambient condition has an extremely low volumetric energy density, making its safe, efficient, and economical storage a significant challenge [9,10].

Compression and liquefaction have been widely employed to store hydrogen [11–13], but they have high energy costs and the volumetric density is still low. A more viable approach is hydride-based solid state hydrogen storage, which originates from the fact that some metals and alloys can reversibly react with hydrogen [14–16]. Hydride formation provides an important safety advantage over pressurized gas and liquid hydrogen storage methods since gas leakage is no longer a concern. Ideal hydrides should reversibly store enough hydrogen (> 6.5 wt.% H) at moderate conditions (≤ 80 °C) for on–board applications [17]. To address these requirements, a variety of hydrides have been explored, particularly interstitial metal hydrides and light metal hydrides [18–21]. Most interstitial metal hydrides store hydrogen atoms in their lattice interstitial sites via metallic bonding, which readily proceeds at moderate temperatures and pressures, but offer a significantly limited hydrogen capacity (< 3 wt.% H) owing to their primarily heavy transition metal (e.g., Ti, Zr, V, Cr, Mn, Fe, Co, and Ni) or rare earth metal (e.g., La, Ce, Pr, Nd, etc.) composition [22]. Concerning the gravimetric density of stored hydrogen, light metal hydrides have a reasonable probability of fulfilling the practical requirements, including binary hydrides such as MgH_2 and complex hydrides such as alanates, borohydrides, amides/imides [10,15,18,19,23,24]. Fig. 1 summarizes and compares their theoretical hydrogen capacities. They are typically higher than 7.0 wt.% H_2. However, the high thermodynamic stability and kinetic barriers of these materials require high temperatures and pressures, making hydrogen cycling impractical for mobile applications. In the last two decades, studies have focused on customizing the thermodynamics and kinetics of the hydrogen storage reactions of light metal hydrides. In this review, the recent research progress in light metal hydrides for reversible hydrogen storage is summarized with a focus on nanostructuring. It is begun with a brief introduction to the hydriding mechanism of light metals, particularly the reaction thermodynamics and kinetics. And then, the synthesis, hydrogen storage behaviors, and mechanisms of nanostructured light metal hydrides are examined. Finally, the upcoming challenges are discussed and the ideas on future research strategies are conveyed.

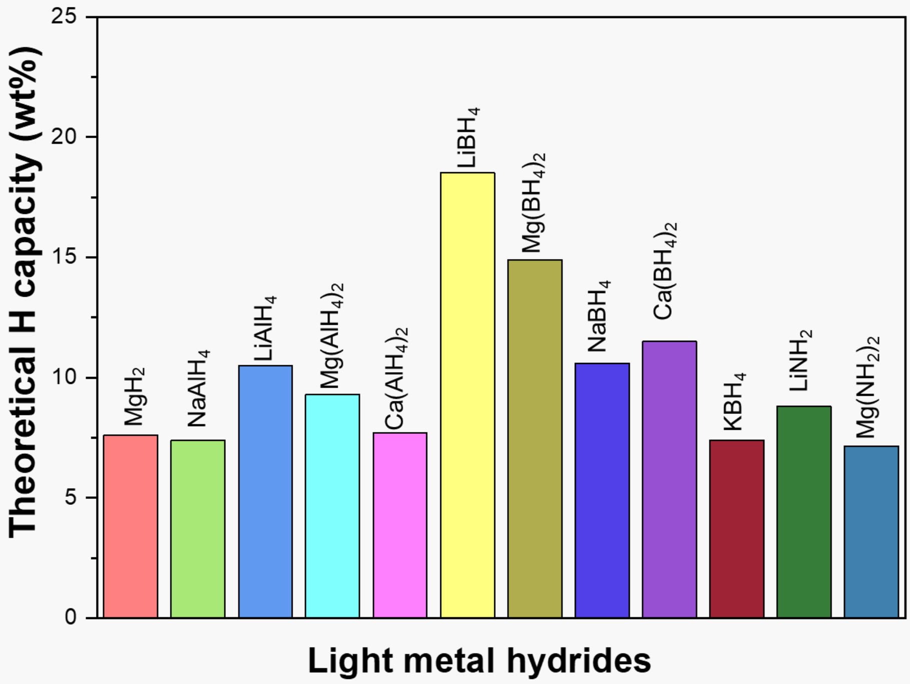

Fig. 1. Theoretical hydrogen capacities of light metal hydrides for reversible hydrogen storage.

2. Hydriding/dehydriding mechanisms of light metal hydrides

The hydrogen storage performance of materials is strongly related to their physical and chemical properties, particularly the thermodynamic and kinetic properties [25]. Fig. 2 illustrates schematically the hydrogen storage process of a material and the corresponding energy change. In general, the hydriding process includes molecular H_2 adsorption, molecular H_2 dissociation to atomic H, atomic H absorption, bulk diffusion, and M–H bonding (Fig. 2a) [1,13], whereas dehydriding occurs through a reverse process commencing with the breaking of M–H bonds. Such a process must overcome a range of activation energy barriers, as depicted by the Lennard–Jones potential energy curve (Fig. 2b) [1,25,26]. Specifically, molecular H_2 dissociation can occur only when the energy input exceeds the activation energy. This is not a concern for interstitial metal hydrides, because they mainly comprise 3d transition metals with high catalytic activity. However, for light metal hydrides, this is critical because of their low reactivity toward H_2 owing to the lack of d–electrons in light metals, resulting in harsh conditions, such as high temperatures and pressures, for hydriding and dehydriding. Typically, the reported formation temperature of $LiBH_4$ from LiH and B is 600 °C under 350 bar H_2 or 700 °C under 150 bar H_2, and the $LiBH_4$ dehydriding temperature exceeds 400 °C [27,28]. Therefore, it is critical to minimize the activation energy barriers for hydriding and dehydriding.

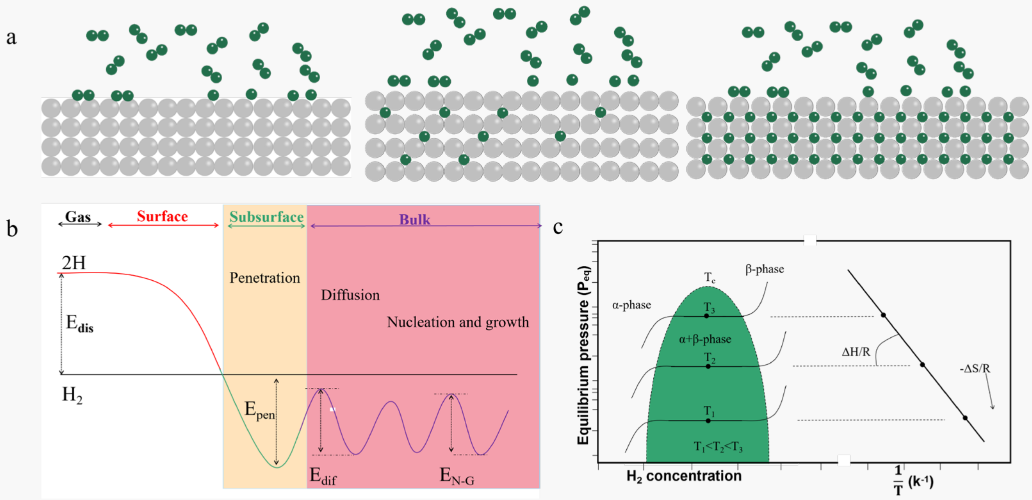

Fig. 2. (a) Schematic hydrogen storage process of a material (green: H_2, gray: Metal). Adapted with permission from ref. [1], (b) Lennard–Jones potential energy curve for

hydrogen binding to a metal. Adapted with permission from ref. [1,25,26,30], (c) Typical van't Hoff plot for the calculation of enthalpy and entropy changes of a hydrogen desorption reaction. Adapted with permission from ref. [1,30].

The primary thermodynamic driving force for the hydriding reaction is the Gibbs free energy (ΔG) at certain temperatures and pressures. The hydriding reaction for reversible hydrides is typically exothermic (releasing heat), whereas the dehydriding reaction is endothermic (requiring heat) [29]. The difference in the internal energy between the initial and hydride states is directly proportional to the heat released during hydriding, which is reasonably related to the bond energy of H–X (X = metal or non–metal atom) in the system [26]. In stark contrast to interstitial hydrides, hydrogen is ionically or covalently bound to metals such as in MgH_2 and alanates or non-metals such as borohydrides and amides/imides in the light metal hydrides [10]. Strong chemical bonds induce the high temperatures necessary for releasing hydrogen. The hydriding and dehydriding processes can be thermodynamically studied by analyzing the pressure–composition isotherms (PCIs) at various temperatures (Fig. 2c) [1,29,30]. The van't Hoff equation relates the plateau pressure (P_{eq}) to the changes in enthalpy (ΔH) and entropy (ΔS) of the hydriding reaction at a given temperature (T) [15,29].

$$\ln P_{eq} = \frac{\Delta H}{RT} - \frac{\Delta S}{R} \qquad (1)$$

where, R represents the gas constant. Thus, plotting $\ln P_{eq}$ vs. $1/T$ results in a straight line with a slope of $\Delta H/R$ and an intercept of $-\Delta S/R$. For P_{eq} = 1 atm, the desorption temperature can be determined as follows:

$$T = \frac{\Delta H}{\Delta S} \qquad (2)$$

The entropy change (ΔS) of the hydrogen storage reaction primarily originates from the generation and disappearance of dihydrogen molecules, which equals approximately 130 $J{\cdot}K^{-1}{\cdot}mol^{-1}$ H_2 for metal–hydrogen systems [9,30]. Theoretically, MgH_2 dehydriding ($\Delta H \approx 76$ $kJ{\cdot}mol^{-1}$ H_2) requires a temperature as high as 311 °C at 1 atm of equilibrium pressure, which surpasses the limit for practical applications. From a thermodynamic perspective, weakening of the M–H bond is particularly useful for reducing dehydriding temperatures.

3. Nanoengineering to tailor thermodynamics and kinetics

In general, a practical hydrogen storage material should operate at or near ambient conditions, specifically 1–10 atm and 0–100 °C [29]. However, owing to their high thermodynamic stability and kinetic barriers, light metal hydrides often desorb hydrogen at high temperatures and absorb hydrogen at high pressures, which are unsuitable for practical applications. Thus, developing effective approaches to balance thermodynamic and kinetic improvements against high hydrogen capacity targets is a key challenge [5]. This problem can be mitigated in part by decreasing the particle sizes. The thermodynamics and kinetics of hydrogen adsorption, diffusion, and bonding are improved by nanosizing [6,31–34]. Particle size reduction enhances surface-to-volume ratios and decreases diffusion lengths of mass, charge, and heat, yielding a variety of intriguing physical and chemical properties [35]. As a result, numerous studies have been conducted on nanostructured light metal hydrides, including MgH_2, $NaAlH_4$, $LiBH_4$, $Mg(BH_4)_2$, and metal–N–H (M–N–H), to improve the reversible hydrogen storage properties. These studies are summarized in the following sections.

3.1 Nanostructured Mg/MgH₂

MgH_2, having 7.6% of H content (in mass ratio) and 110 kg·H·m^{-3} of volumetric density, has been extensively studied as a promising hydrogen storage candidate [16,36]. More importantly, Mg is the eighth most abundant element in the Earth's crust, with 23% of abundance, and therefore, inexpensive [37]. Unlike LiH and NaH, which are treated as ionic hydrides, MgH_2 was found to bear both ionic and covalent bonds with a charge distribution of $Mg^{+1.91}H^{-0.26}$ [38]. Considerable theoretical calculations have been carried out to explore the size effects on the thermodynamic stability of MgH_2 [39–47]. An early study predicted a 15% reduction in the formation enthalpy for ~3–nm sized MgH_2 particles owing to the large surface effect (surface atoms: >50%) [39]. Chenug et al. indicated a change in the formation heat of MgH_2 from –79 kJ mol^{-1} to –67 kJ mol^{-1} of H_2 when the particle size was reduced from 2 nm to 0.6 nm [40]. In particular, a desorption enthalpy of 37.55 kJ mol^{-1} of H_2 for MgH_2 nanowires with ~1 nm in diameter was predicted, which is only half of the bulk (74 kJ mol^{-1} of H_2) [41]. The desorption temperature of 0.63 nm MgH_2 nanowire was reduced by 164 ºC with respect to the bulk counterpart [42]. Similarly, the decomposition temperature of MgH_2 thin film was theoretically determined to be lower than 100 ºC when its thickness was reduced to 1 nm [43]. Furthermore, a 1.3–nm critical size was predicated to achieve a significant decrease in the hydrogen desorption energy of MgH_2 [44]. For Mg_nH_{2n} nanoclusters, the average dehydriding temperature was calculated to be ~200 ºC when $n \leq 8$, 100 ºC lower than that of the bulk MgH_2 [45]. Also, a linear behavior in adsorbing the H_2 molecules and the binding energy values was recently demonstrated for the nanoparticle clusters of MgH_2 [46]. With increasing the adsorbing H_2 molecules from 1 to 6, the binding energy per H_2 molecule decreased uniformly from 0.15 to 0.12 eV. All these results unambiguously indicate that both Mg and MgH_2 become much more unstable with decreasing size, especially below 1 nm [47]. However, the preparation of small nanoparticles for MgH_2 or Mg is challenging. Table 1 summarizes the synthesis processes and hydrogen storage properties of nanostructured MgH_2/Mg.

3.1.1 Synthesis methods and hydrogen storage properties of freestanding MgH_2/Mg nanostructures

Mechanical milling is the most frequently employed technique to decrease MgH_2 and Mg particle sizes. The sample powders are placed into a milling jar with milling balls and then sealed. The mechanical milling operations are conducted on a planetary ball mill or a vibration ball mill. In 1999, Zaluska et al. demonstrated the effectiveness of ball milling in improving the hydrogen storage properties of MgH_2 [50]. Schulz et al. reported a 10-times increase in the MgH_2 specific surface area after 20 h of milling using the SPEX 8000 apparatus [51]. The desorption activation energy decreased from 156 to 120 kJ·mol^{-1}, enabling significant desorption at 300 °C for the milled sample, whereas no desorption was observed for the pristine sample. Unfortunately, mechanical milling cannot produce particles below 100 nm in size. This limitation is mainly attributed to the continuous fracturing, agglomeration, and cold-welding during ball milling [52].

Moreover, the collision force during mechanical milling is of the order of gigapascals, which can initiate chemical reactions and produce ultrafine nanoparticles via mechanochemical synthesis [53]. Paskevicius et al. obtained MgH_2 nanoparticles below 7 nm in size by mechanically milling an LiH–$MgCl_2$ mixture in a 2:1 molar ratio, and the following metathesis reaction occurred owing to favorable thermodynamics ($\Delta G \approx -75.06$ kJ·mol^{-1}) [54].

$$2LiH + MgCl_2 \rightarrow MgH_2 + 2LiCl \tag{3}$$

The resultant MgH_2 nanoparticles exhibited a 2.84–kJ·mol^{-1} H_2 decrease in the decomposition enthalpy change, which is responsible for the 6 °C reduction in the desorption temperature operating at a 1–atm equilibrium pressure. On introducing graphene nanosheets as a support, Zhang et al. obtained well-dispersed ~3–nm MgH_2 nanoparticles, which displayed a 255 °C of onset dehydrogenation temperature and released 5.1 wt.% H in 20 min at 325 °C [55]. Notably, Zhang et al. reported a unique ultrasound-driven liquid–solid reaction (3) to fabricate freestanding ultrafine MgH_2 nanoparticles [56]. Using THF as the reaction medium, reaction (3) was readily initiated using ultrasound at 30 ºC. The turbulence and microstreaming arising from ultrasonic wave exposures enhanced reactant collisions and simultaneously deterred excess crystal growth, which facilitated ultrafine particles formation. In addition, the produced MgH_2 did not react with THF but was surrounded by it, which disrupted the agglomeration. The high solubility of LiCl in THF and the higher density of MgH_2 (1.45 g·cm^{-3}) than that of THF (0.89 g·cm^{-3}) eventually induced the precipitation of as-formed MgH_2 from the solution. Fig. 3 shows the morphology and hydrogen storage properties of the final products. The resultant MgH_2 comprises monodispersed nanoparticles with diameters of 4–5 nm diameter, featuring reversible hydrogen storage with a 6.7 wt.% capacity at 30 °C and 50 atm H_2. This was the first experiment observing that MgH_2 can desorb hydrogen at ambient temperature, albeit with very sluggish kinetics, thus making MgH_2 usable as a potential hydrogen storage medium. Moreover, a 10–nm critical size is required to simultaneously tailor the thermodynamics and kinetics of hydrogen storage in MgH_2.

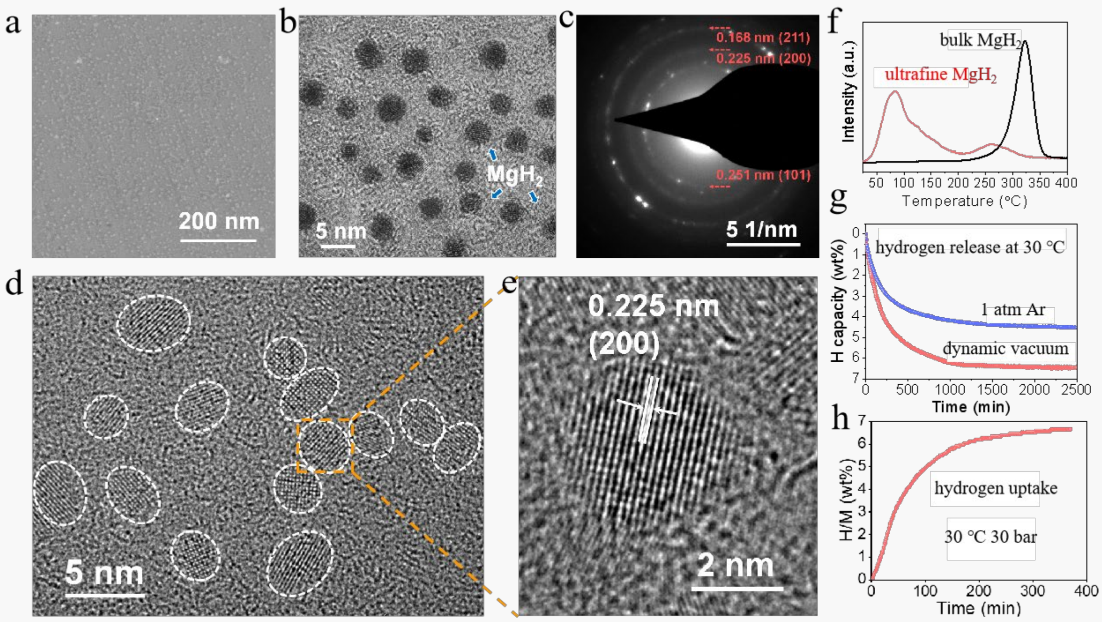

Fig. 3. Morphology and hydrogen storage properties of non-confined ultrafine MgH_2. (a) SEM image, (b) TEM image, (c) SAED pattern, (d–e) HRTEM images, (f) TPD, (g) isothermal dehydrogenation, and (h) isothermal hydrogenation. Reprinted with permission from ref. [56].

MgH_2 nanoparticles were also produced using the thermal decomposition of Grignard reagents, which exhibit a strong dependence of morphology and hydrogen storage properties on the precursors and reaction conditions. In 1952, Wiberg and Bauer first demonstrated the MgH_2 preparation from diethylmagnesium pyrolysis under high vacuum [57]. Subsequently, Becker and Ashby synthesized MgH_2 by hydrogenolysis of Grignard reagents as described as follows [58]:

$$2RMgX + 2H_2 \rightarrow 2RH + MgX_2 + MgH_2 \tag{4}$$

Where X is a halide. In 2012, Setijadi et al. studied the possibility of generating MgH_2 nanoparticles using Grignard reagents [59]. Fig. 4 displays the TEM images, desorption curves and XRD patterns of the hydrogenolysis products. It was observed that di-*n*-butylmagnesium produced ~30–nm MgH_2 nanoparticles, which released hydrogen without any catalyst within 2 h at 250 °C. Hexagonal Mg nanoparticles were synthesized by chemically reducing ethyl magnesium chloride and methyl magnesium chloride, *n*–butyl magnesium chloride, and phenyl magnesium chloride with lithium naphthalide in anhydrous THF under Ar [60]. MgH_2 nanoparticles exhibiting different morphologies and sizes were also obtained using liquid–phase thermal decomposition of Grignard compounds such as diethylmagnesium, dipropylmagnesium, diisopropylmagnesium, di–*n*–butylmagnesium, di–*tert*–butylmagnesium, and dihexylmagnesium, which adopted spherical shapes, hexagonal structurs,e or nano–tubes/rods [61]. More importantly, the nanostructured MgH_2 synthesized from di–*tert*–butylmagnesium precursor could release hydrogen at 100 °C, indicating its potential for mobile hydrogen storage applications.

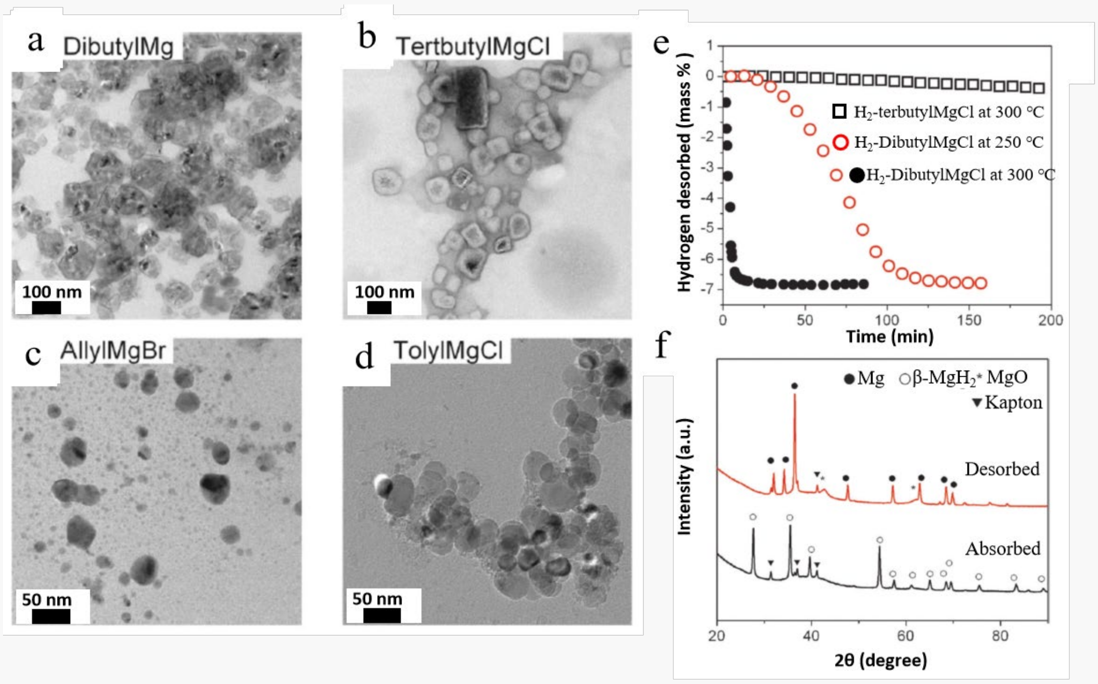

Fig. 4. TEM images of the materials obtained via hydrogenolysis of (a–d) the Grignard reagents. (e) Hydrogen desorption kinetics of H_2–TertbutylMgCl and H_2–DibutylMg measured under isothermal conditions and at a pressure of 0.1 bar. (f) XRD patterns of H_2–DibutylMg after hydrogen absorption and desorption. Reprinted with permission from ref. [59].

Nanostructured Mg was successfully synthesized by reducing magnesium precursors in organic solutions with alkali or alkaline earth metals (Li, Na, K, Ca, etc.) as reducing agents in the presence of electron carriers (e.g., naphthalene and phenanthrene). Norberg et al. prepared 25–38 nm magnesium nanocrystals by chemically reducing magnesia using potassium and aromatics as reducing agents [62]. The H_2 absorption rates of the 25–nm particles were more than seven times higher than those of the 38–nm particles. Similarly, Liu et al. obtained 8–nm Mg particles by the lithium–assisted reduction of di–*n*–butylmagnesium in the presence of naphthalene as an electron carrier [63]. This material was observed to absorb hydrogen at temperatures below 150 °C. Thermodynamically, the enthalpy and entropy changes were decreased to 63.5 ± 1.8

kJ·mol^{-1} H_2 and 118.4 ± 3.1 J·K^{-1}·mol^{-1} H_2, respectively, demonstrating remarkable thermodynamic alterations. Mg particle morphology can be modified by regulating the reaction medium. For example, well–defined Mg nanofibers having 0.4–4 μm length and 40–nm width were obtained by the direct reduction of dibutylmagnesium with calcium [64]. The Mg nanofibers exhibited fast absorption kinetics at both 300 and 350 °C (> 90% hydrogen absorption in 20 min), with a slightly lower enthalpy change compared with bulk Mg.

Physical and chemical vapor deposition techniques, such as hydrogen plasma-metal reaction (HPMR), pulsed laser deposition, and magnetron sputtering, are typically utilized to prepare 1D and 2D nanostructures of Mg/MgH_2. In 2007, Li et al. prepared Mg nanowires with the diameters of 30–50 nm, 80–100 nm, and 150–170 nm using the vapor–transport method, which remarkably enhanced the hydrogen absorption/desorption kinetics [65]. Fig. 5 compares their TEM images and hydrogenation/dehydrogenation performance. The 30–50 nm nanowires absorbed 2.93 wt.% hydrogen at 100 °C within 30 min, and hydrogen uptake increased to 7.6 wt.% at 300 °C within 30 min. During desorption, approximately 3.28 wt.% H was liberated from the 30–50 nm sample within 30 min at 200 °C, much rapidly than the 150–170 nm sample, which released only 0.5 wt.% H under the same conditions. Therefore, thinner Mg/MgH_2 nanowires are assumed to possess a significantly lower desorption energy than thicker nanowires or bulk Mg/MgH_2. Zhu et al. reported MgH_2 nanofiber synthesis via hydriding chemical vapor deposition (HCVD) and observed a strong dependence of the product shape, size, and purity on the experimental conditions

[66,67]. Their studies revealed the shape-controlled growth mechanism of MgH_2/Mg nanostructures, which can aid mass production for hydrogen storage applications.

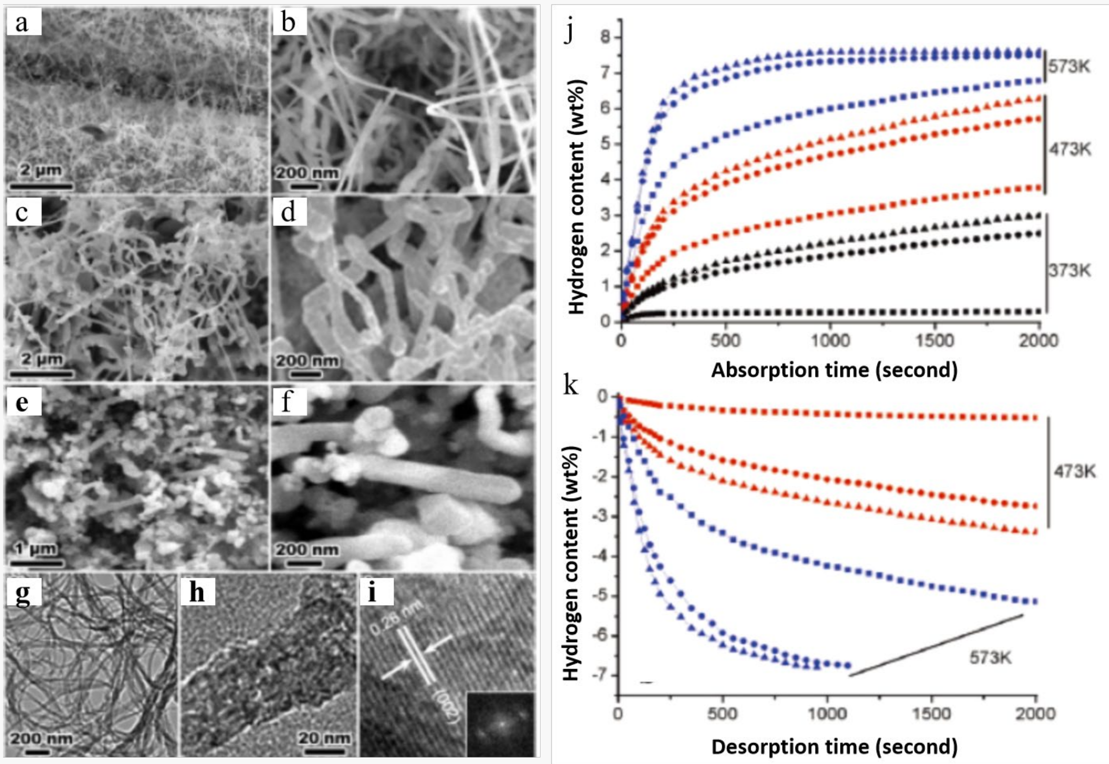

Fig. 5. Mg nanowires with different diameters were obtained at different Ar flow rates: 200 cm^3 min^{-1} for sample 1, 300 cm^3 min^{-1} for sample 2, and 400 cm^3 min^{-1} for sample 3. SEM images of the Mg nanowires: (a–b) sample 1, (c–d) sample 2, and (e–f) sample 3. (g–h) TEM and (i) HRTEM images of sample 1 with the corresponding fast Fourier transform (FFT) pattern (inset). (j–k) Hydrogen absorption and hydrogen desorption of the Mg nanowires (sample 1, triangle; sample 2, circle; sample 3, square). Reprinted with permission from ref. [65].

Moreover, nanostructured Mg/MgH_2 thin films have been widely studied as model systems for understanding hydrogen sorption kinetics [68,69]. It is facile to control thin film crystal structures, such as amorphous structure, nanocrystalline, and columnar structures. Consequently, thin films are more suitable than other nanostructures for studying the influence of thickness, microstructure, and surface state on hydrogen absorption/desorption [70]. In 2002, Léon et al. successfully prepared 30–μm thick Mg thin films using thermal evaporation deposition, which evidently exhibited a columnar structure and absorbed hydrogen at 350 °C under 10 atm H_2 [71]. Furthermore, they observed that the [002]–direction Mg films exhibited significantly faster absorption/desorption kinetics [72]. In particular, the hydrogen sorption kinetics of Mg films prepared using an electron beam source under a high vacuum was nearly twice as fast compared with those obtained using resistive heating under low vacuum. Barawi et al. studied the influence of the initial thickness and substrate on the hydrogen absorption/desorption process in Mg films [70]. Compared with bulk MgH_2, films with thicknesses <150 nm exhibited slightly reduced temperatures for complete hydriding and dehydriding. Shimizu et al. recently reported the epitaxial growth process of single–phase MgH_2 thin films on MgO(100) substrates using reactive magnetron sputtering [73]; MgH_2 decomposition was observed when the substrate temperatures exceeded 100 °C. Using the same approach, they obtained MgH_2(100) and MgH_2(001) epitaxial thin films on Al_2O_3(001) and MgF_2(001) substrates, respectively. These findings indicate the possibility of adjusting the thermodynamics and kinetics of hydrogen storage by MgH_2 epitaxial thin films.

To obtain enhanced hydrogen sorption properties, other studies have focused on Pd–capped Mg films because the Pd layer serves not only as a protective layer against Mg oxidation but also as a catalyst for hydriding/dehydriding. In 1990, Krozer et al. prepared 7.5-nm thick Pd film-coated Mg thin films (380–800 nm) through ultrahigh vacuum evaporation deposition [74]. These Pd/Mg films allowed hydrogen sorption within the pressure range of 0.01–0.6 Torr, i.e., at 10^5 times lower pressure than bulk

Mg and within the temperature range of 17–97 °C. The enthalpy changes of hydride formation and decomposition were determined to be 60.7 ± 6.3 kJ·mol^{-1} H_2 and 71 ± 4.2 kJ·mol^{-1} H_2, respectively. Similarly, Higuchi et al. observed the absorption of 2.9–6.6 wt.% H at 100 °C using Pd (25 nm) –capped Mg (200 nm) films prepared by radio frequency (RF) sputtering on glass substrates under various sputtering conditions [75]. The hydrogenated films accomplished dehydrogenation at temperatures above 190 °C. A significant reduction in hydrogen sorption temperature from 397 to 202 °C was demonstrated for the Pd–capped Mg thin films prepared using plasma sputter and pulsed laser deposition [76]. Two distinct types of films absorbed 4–7.5 wt.% H at ~197 °C between 2.5–10 atm H_2. However, the hydrogen capacity rapidly decreased within only a few of cycles, possibly owing to the partial delamination of the topmost Pd layer. The three–layered Pd/Mg/Pd films desorbed hydrogen at ~187 °C, but the hydrogen capacity decreased to 5 wt.% [77]. Notably, Pd–Mg–Pd thin films prepared via magnetron sputtering could absorb hydrogen even at room temperature [78]. The cooperative effect of the double Pd layer was responsible for the improved absorption and desorption properties. Furthermore, multilayer films, such as Pd/MgAl/Mg/Pd, Pd/Mg/Ni/Pd, Pd/Mg/Mg_2Ni/Pd, Pd/Ni/Mg/Pd, and Pd/Ti/Mg/Ti, were also prepared and evaluated [79–83]. Here, the interlayer served as a catalyst and blocking layer, facilitating hydrogenation properties, providing additional diffusion pathways, and preventing Mg–Pd intermetallic phase formation. A similar phenomenon was also observed in the Cr– and V–interlayers–comprising Pd/Mg/Pd films [84].

Although the Pd–capped Mg films exhibited the best hydrogen sorption kinetics, the high economic cost of Pd hinders its scalability. To mitigate this issue, Zhu's group studied a series of Mg/(rare earth alloy) multilayer films and demonstrated that the Mg/Mm–Ni multilayer allowed hydrogen absorption commencing at 100 °C and desorption at 200 °C [85–88]. The improved hydrogen storage properties were primarily attributed to the catalytic role of Nd(La)Ni_3 in the Mm–Ni layer and Mg_2Ni phases [87]. Other metals, including Mn– and Cu–capped Mg films, have been studied and reported [89–91]. Notably, the Mg phase in the Mg/Cu multilayer films could be completely converted into MgH_2 below 200 °C [91]. Recently, a new Mg/polymer thin film system demonstrated promising hydrogen sorption properties at low temperatures (< 150 °C) with high air stability [92]. However, the presence of polymers significantly reduced the hydrogen storage capacity of the film [93], which is unfavorable for practical applications.

3.1.2 Synthesis methods and hydrogen storage properties of nanoconfined and supported MgH_2/Mg

Generally, isolated Mg nanoparticles tend to agglomerate during cycling. Moreover, the cost- and energy–efficient production of large quantities of nanostructured materials remains challenging [16]. Confining nanoparticles within a scaffold is a feasible strategy to maintain stability and prevent agglomeration and sintering during cycling [31]. Porous materials, including ordered mesoporous silicas, metal organic frameworks, and porous carbon materials, have been extensively utilized as scaffolds to confine MgH_2 [94–100]. For instance, de Jongh et al. successfully prepared 2–5 nm Mg nanoparticles by infiltrating nanoporous carbon with molten Mg [101]. The resultant sample exhibited a 15 wt.% loading of Mg on carbon with a good air stability because the majority of Mg remained unoxidized after preparation. Similar results were observed by infiltrating the carbon aerogel using the dibutylmagnesium ($MgBu_2$) precursor solution [99]. MgH_2 was obtained by further hydrogenation of the incorporated $MgBu_2$. The dehydrogenation kinetics of the incorporated MgH_2 nanoparticles was more than 5 times faster than that of ball–milled MgH_2, which remained constant over four cycles. Furthermore, Nielsen et al. reported a strong dependence of hydrogen sorption kinetics on the pore size distribution of scaffold materials [96]. When confining MgH_2 into 5–10 nm SBA–15 ordered mesoporous silicas using solution impregnation followed by freeze drying and hydrogenation treatment, the desorption temperature decreased by 146 and 65 °C relative to that of bulk MgH_2 and nanoparticles without confinement, respectively [94]. Au et al. further confirmed the findings by fabricating 6–20 nm carbon aerogels-supported MgH_2 nanoparticles and demonstrated the size dependence of the hydrogen mobility and sorption kinetics [98]. The lowest desorption peak temperature (~275 °C) was observed for the 6–nm sample, which was reduced by ~145 °C compared with bulk MgH_2. Also, Zhao-Karger et al. reported that the nanoconfined MgH_2 nanoparticles having diameters between 0.7 and 1 nm offered a 52 and 22–$kJ \cdot mol^{-1}$ reduction in the activation barrier compared with those of the bulk and the ball milled MgH_2, respectively [103]. Jia et al. successfully realized low temperature hydrogen release at 50 °C by utilizing a high surface area ordered mesoporous carbon scaffold (CMK–3)–confined MgH_2 system with 37.5 wt.% loading efficiency [103]. Furthermore, they significantly increased the hydrogen storage capacity and kinetics by functionalizing the ordered mesoporous carbon scaffolds using N doping or Ni decoration. The major desorption peak shifted from 430 to 350 °C for the N–doped sample [104]. Recently, Ma et al. synthesized a novel CoS nanobox–confined MgH_2 wherein MgH_2 particles were controlled between 5 and 10 nm in size [105]. Their morphology, component and hydrogen storage performance are shown in Fig. 6. The nanosizing effects, catalysis effects, and multifunctional role of the CoS scaffold are assumed to synergistically contribute to the remarkable reduction in the activation energy (E_a) to 57.4 ± 2.2 and 120.8 ± 3.2 $kJ \cdot mol^{-1}$ for hydrogen absorption and desorption, respectively. At 200 °C, the reversible hydrogen capacity was determined to be 2.98 wt.%, significantly lower than the theoretical value for pristine MgH_2. The limitation of nanoconfinement is the massive decrease in the practically usable hydrogen capacity of entire systems owing to the dead weight of scaffold materials and the low loading efficiency.

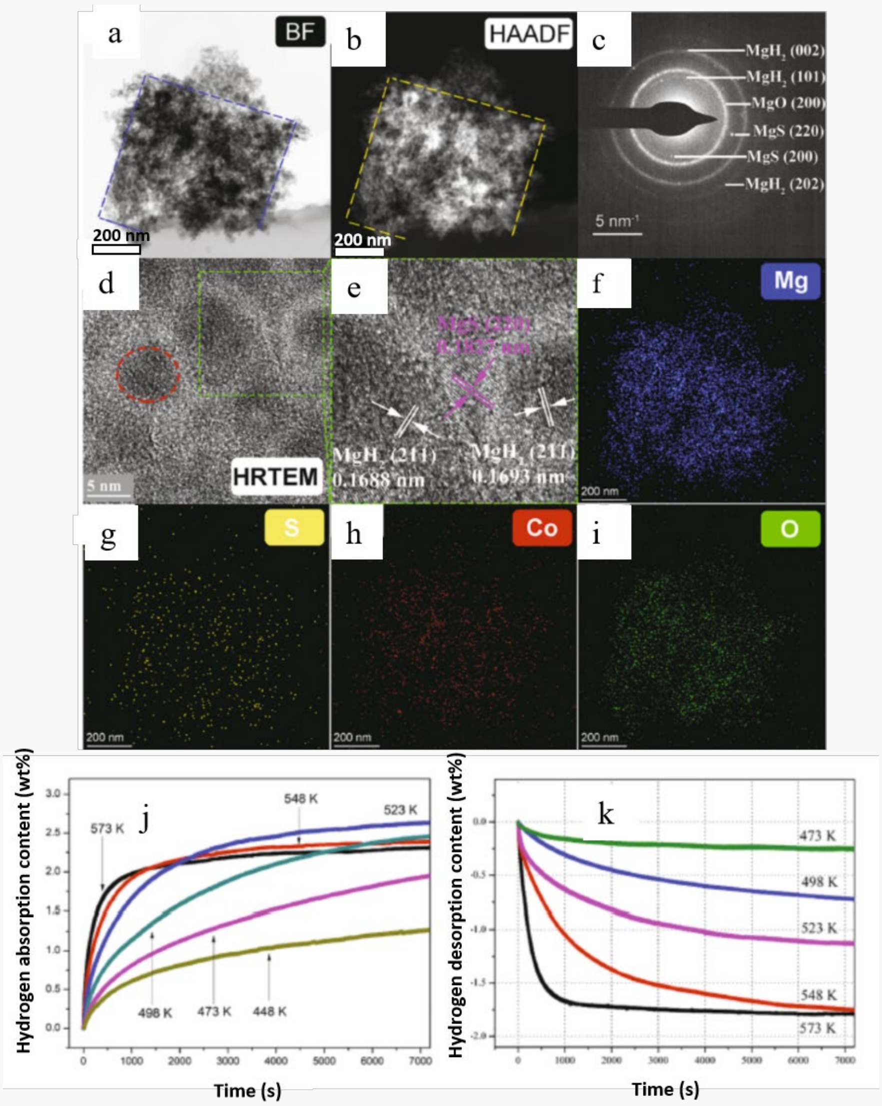

Fig. 6. (a) Typical bright field TEM image, (b–c) HAADF image and the corresponding SAED patterns, (d–e) HRTEM micrographs, (f–i) the corresponding elemental mapping of HRTEM micrographs, (j–k) isothermal hydrogenation and dehydrogenation for the MgH_2@CoS–NBs composite. Reprinted with permission from ref. [105].

When considering the practical hydrogen capacity, graphene should be utilized as an optimal support because of its light weight, large specific surface area, and stable thermal properties owing to a single layer of carbon atoms. This conjecture was supported by Xia et al., who demonstrated that monodispersed Mg nanoparticles uniformly self-assembled on graphene [106]. Fig. 7 presents the morphology and hydrogen storage properties of the resultant Mg nanoparticles. Graphene–supported MgH_2 nanoparticles were fabricated through di–butylmagnesium hydrogenolysis in cyclohexane at 200 °C. The average particle diameter of MgH_2 was determined to be ~5.7 nm and the loading amount was dramatically increased to 75 wt.% with 5.7 wt.% of practical hydrogen capacity. Specifically, the desorption peak temperature was reduced to 247 °C, which was 121 °C lower than that of bulk MgH_2. Introducing the Ni catalyst further decreased the desorption peak temperature to ~201 °C with 5.4 wt.% of practical hydrogen capacity. The significant improvement primarily originated from the synergistic effects of nanostructuring and catalytic activity of both the graphene and Ni nanoparticles homogeneously distributed within the composite. Saturated hydrogenation was achieved at 200 °C under 10 min, and the hydrogenation capacity attained a value of ~ 5.1 wt.% when held at room temperature for 300 min. Furthermore, a capacity retention of up to 99.2 wt.% was measured within 100 cycles when operating at 200 °C, for Ni–containing graphene-supported MgH_2 nanoparticles. Cho et al. synthesized ~3.26–nm Mg nanocrystals encapsulated by atomically thin and gas selective reduced graphene oxide (rGO) sheets, which delivered 6.5 wt.% H and 105 g H_2 per liter at 300 °C with a stable cyclability [107]. Air–stable Mg nanocrystals (NCs) encapsulated in poly(methyl methacrylate) (PMMA) were also synthesized via solution impregnation and in situ hydrogenation [108]. Fig. 8 shows high–resolution TEM images and hydrogen absorption properties. The average diameter of Mg NCs was observed to be 4.9 ± 2.1 nm with 61 wt.% of loading amounts. At 35–atm H_2 and 200 °C, the prepared Mg NCs/PMMA absorbed ~4 wt.% H in the overall composite mass. The activation energy values were measured to be 25 and 79 kJ·mol^{-1} for absorption and desorption, respectively, which are comparable to those obtained using highly active metal catalysts. Similarly, Makridis et al. reported a polymer–stabilized Mg nanocomposite prepared using the laser ablation method [109]. TEM observations revealed the nanoparticle sizes to be below 7 nm, enabling 5.5 wt.% of hydrogen uptake within 20 min at 250 °C, which is comparable to the kinetics and hydrogen capacity of Mg NCs/PMMA. In addition, the laser–ablated nanoparticles exhibited excellent reversibility under vacuum and at 250 °C, which is a lower temperature than ~330 °C corresponding to bulk Mg materials. Liu et al. observed rapid hydrogen desorption of 5.7 wt.% from bamboo–shaped carbon nanotubes–confined MgH_2 nanoparticles at 275 °C, which is remarkably superior to traditional commercial carbon nanotubes [110]. Additionally, densification treatment under 750 MPa enabled a high volumetric capacity of up to 65.90 g·L^{-1}, which exceeds that of the DOE targets (5.5 wt.% and 40 g·L^{-1}, 2025) [17]. Recently, Zhu et al. successfully synthesized MgH_2 nanoparticles (NPs) anchored on annealed 3D $Ti_3C_2T_x$ MXene with 60 wt.% MgH_2 NPs loading [111]. Their morphology and hydrogen storage behaviors are shown in Fig. 9. Superior hydrogen sorption performances, including dehydriding from 140 °C and 4 wt.% of reversible capacity after 60 cycles at 200 °C, were obtained owing to the nanosizing effect resulting from the nanoconfinement and multiphase interfaces between MgH_2(Mg) and Ti–based MXene, particularly the in situ formed catalytic TiH_2. These findings shed light on how support materials can improve the hydrogen storage performance through nanoconfinement and nanocatalysis.

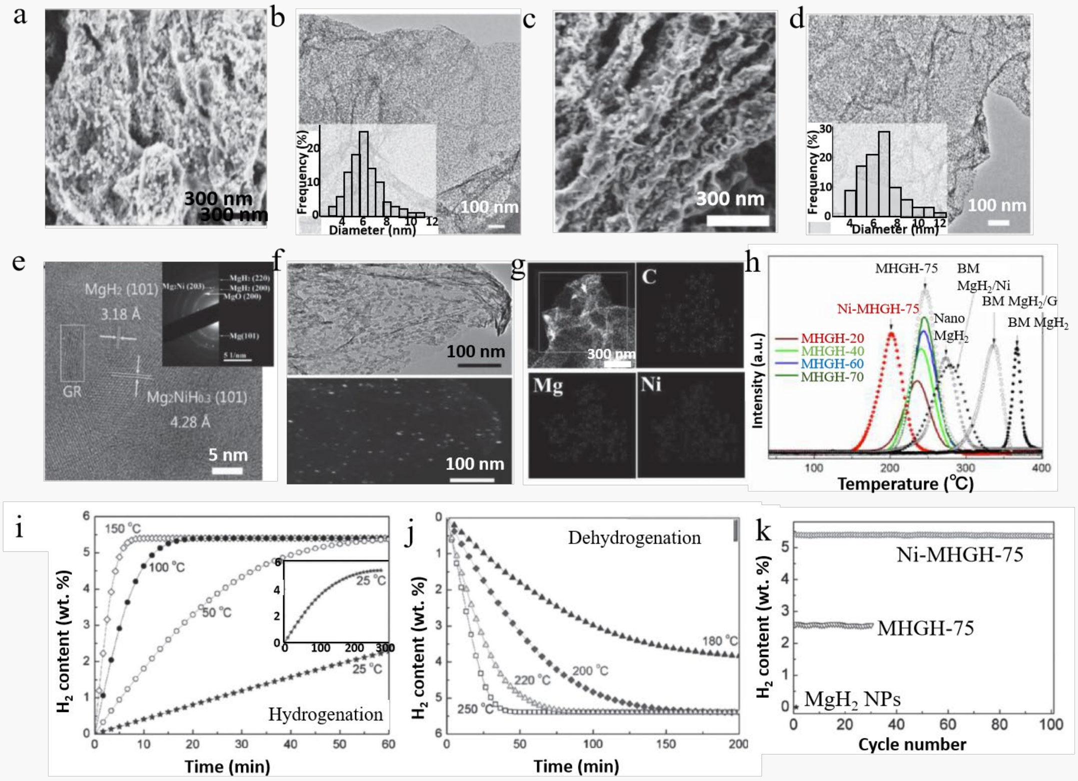

Fig. 7. (a–b) SEM and TEM images of MHGH–75, (c-d) SEM and TEM images of Ni–MHGH–75, (e) HRTEM image of Ni–MHGH–75, (f) bright field and dark field images of Ni–MHGH–75, (g) scanning TEM image of Ni–MHGH–75 and corresponding elemental mapping images of carbon (C), magnesium (Mg), and nickel (Ni) in the selected area, (h) mass spectra of the as–prepared MHGH in comparison with the reference samples, (i–j) hydrogenation and dehydrogenation of Ni–MHGH–75 at various temperatures, (k) hydrogen cycling capacities for reversible hydrogen storage of Ni–MHGH–75, MHGH–75, and MgH_2 NPs at 200 °C. Reprinted with permission from ref. [106].

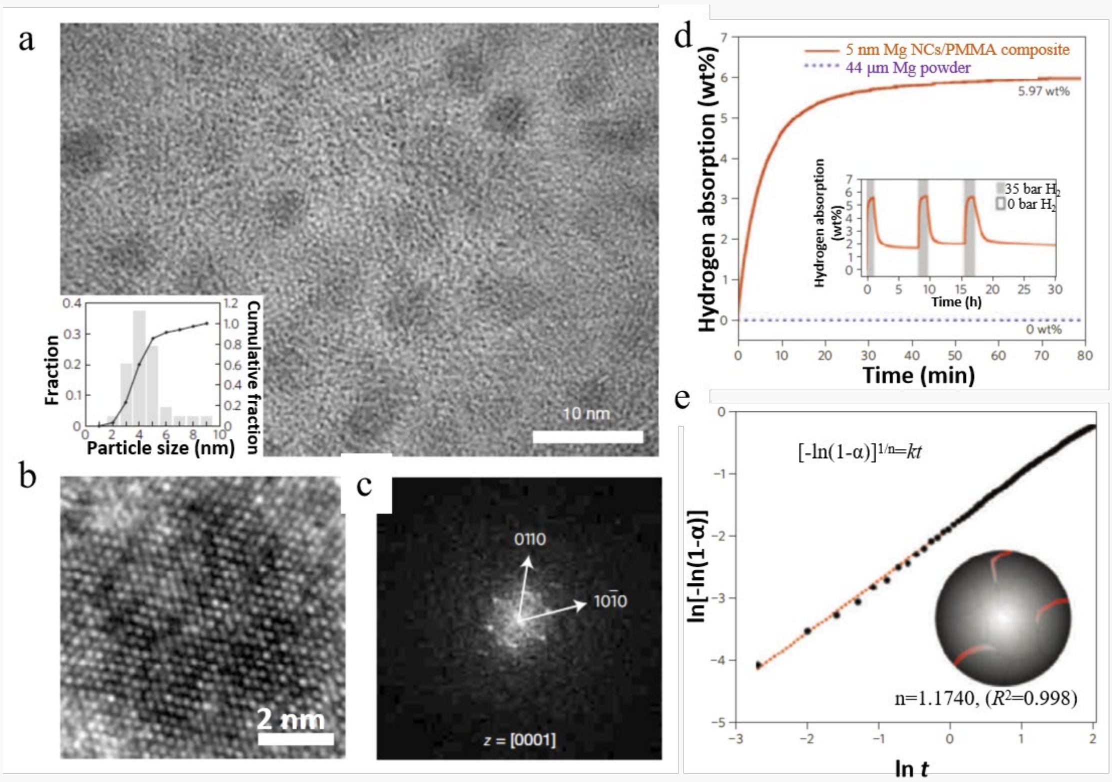

Fig. 8. (a) High–resolution TEM image of the as-synthesized Mg nanocrystals/PMMA composites. Inset: Histogram and cumulative distribution of Mg particle sizes, (b) atomic–resolution image of a single Mg nanocrystal, (c) digital diffractogram of the Mg nanocrystal in b, (d) hydrogen absorption properties of Mg nanocrystals/PMMA composites (absorption at 200 °C and 35 bar) in comparison with bulk Mg, (e) the initial growth mechanism of MgH_2 in Mg nanocrystals/PMMA composites. Reprinted with permission from ref. [108].

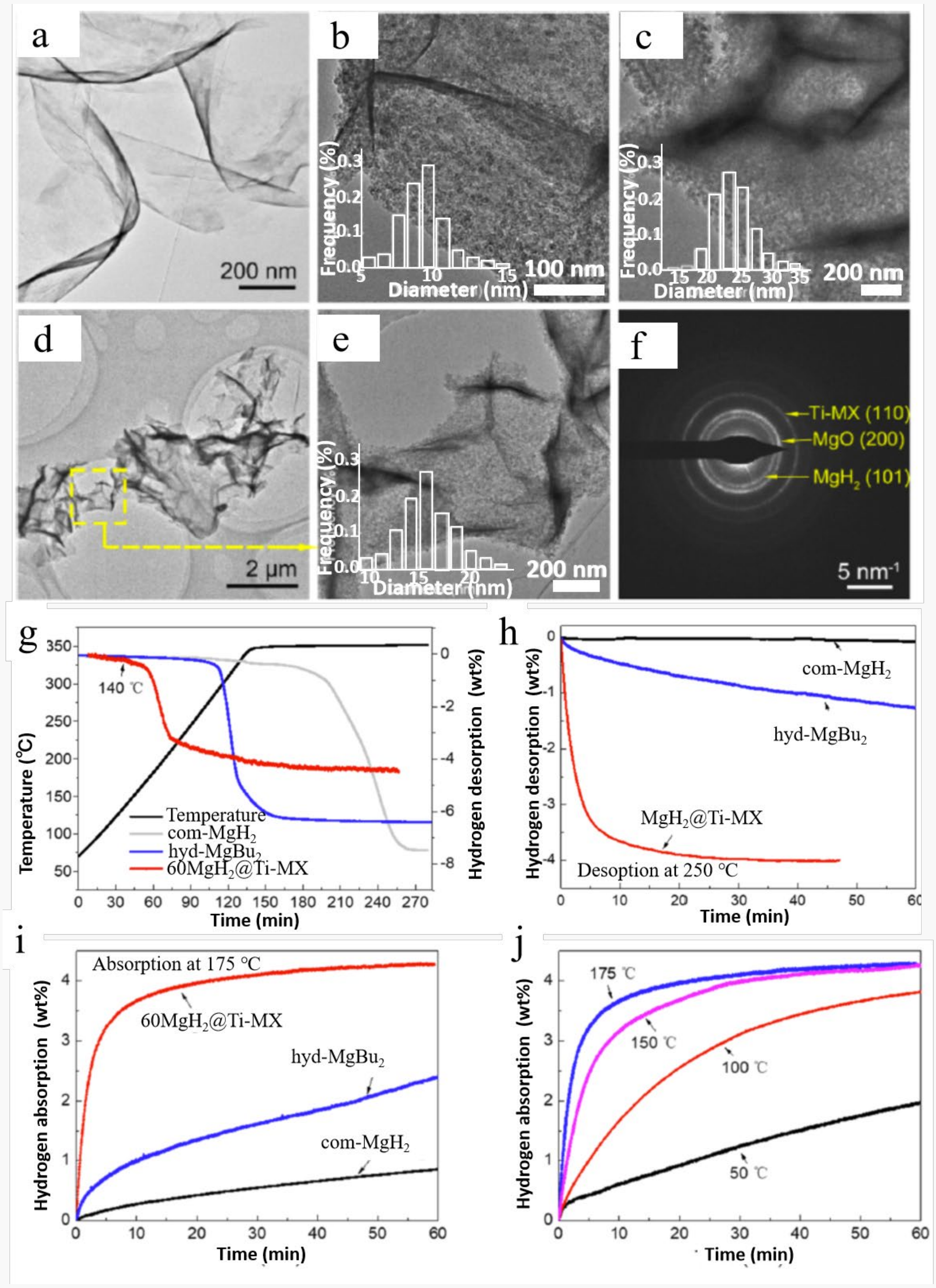

Fig. 9. TEM images of (a) the as–synthesized Ti–MXene, (b) $35MgH_2$@Ti–MXene, (c) $75MgH_2$@Ti–MXene, and (d, e) $60MgH_2$@Ti–MXene, and (f) corresponding SAED pattern of $60MgH_2$@Ti–MXene. (g) TPD curves of commercial–MgH_2, hydriding-$MgBu_2$, and $60MgH_2$@Ti-MXene, (h) isothermal dehydrogenation curves of commercial MgH_2, hyd–$MgBu_2$, and $60MgH_2$@Ti–MXene at 250 °C. (i) Isothermal hydrogenation curves of commercial MgH_2, hyd–$MgBu_2$, and $60MgH_2$@Ti–MXene at 175 °C. (j) Isothermal hydrogenation curves of $60MgH_2$@Ti–MXene at different temperatures. Reprinted with permission from ref. [111].

3.2 Nanostructured metal alanates

As the typical light metal complex hydrides, alanates, especially $NaAlH_4$, have been extensively studied for hydrogen storage applications since Bogdanović and Schwickardi reported that $NaAlH_4$ could reversibly absorb/desorb hydrogen under mild conditions following doping using trace amounts of Ti–based catalysts [112]. $NaAlH_4$ is a white solid having a 7.4 wt.% of hydrogen content. Hydrogen desorption from $NaAlH_4$ was a stepwise process. The change in enthalpy was estimated to be 39.9 $kJ \cdot mol^{-1}$ H_2 for the first-step decomposition of $NaAlH_4$, which corresponds to ~34 °C of operation temperature at 1 atm of equilibrium pressure, therefore being thermodynamically favorable [113]. However, the high kinetic barrier (E_a ~120–159 $kJ \cdot mol^{-1}$) induces high desorption temperatures, which hinders practical applications. Therefore, reducing the activation energy barrier through nanoengineering is of great scientific and practical importance. As predicted theoretically, the hydrogen release energy of $NaAlH_4$ decreases by 68.3% after being confined inside carbon nanotubes [114]. Calculations by Mueller and Ceder revealed that $NaAlH_4$ nanoparticles below a certain size decomposed within a single step directly to NaH, Al, and H_2, which is in stark contrast to the typical two-step reaction for bulk $NaAlH_4$ [115]. More importantly, the nanoparticles with 52 nm in size commenced releasing hydrogen at temperatures as low as 65 °C. Table 2 summarizes the synthesis process and hydrogen storage properties of nanostructured alanates.

3.2.1 Nanostructured $NaAlH_4$

It is generally accepted that the high kinetic barrier of the $NaAlH_4$ system primarily originates from the lengthy mass transport distance owing to macroscopic phase segregation upon dehydrogenation [117]. Therefore, reducing particle/crystallite sizes to the nanoscale should provide an efficient solution for mitigating this issue. In 2000, Zaluska et al. demonstrated the effects of mechanical milling on the hydrogen storage kinetics and observed that milled $NaAlH_4$ could reversibly store hydrogen at lower temperatures in the range of 80–140 °C, with a capacity of between 2.5 and 3.0 wt.% [118]. Since then, considerable attention has been given to the use of high–energy ball milling to prepare catalyst–modified $NaAlH_4$ because of its unique advantages, including the formation of nanocrystalline materials and simultaneous incorporation of selective additives [53,119]. Substantial efforts have been focused on supporting and nanoconfinement with high–specific–surface–area scaffolds, with no reports on the preparation of freestanding $NaAlH_4$ nanostructures possibly due to its high solubility in most organic solvents.

In 2006, Baldé et al. prepared nanosized $NaAlH_4$ particles supported on a surface–oxidized carbon nanofiber (CNF_{ox}) and investigated their hydrogen desorption and absorption behaviors corresponding to their structural properties [120]. Fig. 10 compares their morphology and hydrogen desorption performance. Nanosized $NaAlH_4/CNF_{ox}$ reversibly absorbed and desorbed hydrogen at 160 °C without a catalyst. The $NaAlH_4$ loading amount on CNFs was 9 wt.%. By decreasing the loading to 2 wt.%, 2–10 nm–sized $NaAlH_4$ on carbon nanofibers (CNF) were attained, which demonstrated significant lowering of desorption peak temperature and activation energy from 186 °C and 116 kJ·mol^{-1} to 70 °C and 58 kJ·mol^{-1}, respectively [121]. In addition, decreasing the particle size also lowered the pressures required for rehydriding. Similar effectiveness was observed by synthesizing Ti–doped nanosized $NaAlH_4$ (~20 nm) supported on carbon nanofibers owing to the synergistic effect of the small size and higher catalytic activity [122]. By utilizing various carbon materials such as graphene nanosheets (GNs), fullerene (C60), and mesoporous carbon (MC), Li et al. altered $NaAlH_4$ morphologies from scale–like continuous structures (GN–assisted samples) to flower–like structures (C60–assisted samples) and uniform particles (MC–assisted sample) [123]. Importantly, the onset temperature for $NaAlH_4$ dehydrogenation was reduced to approximately 160 °C for the MC–assisted sample. Ko et al. demonstrated an even lower onset decomposition temperature of 111 °C when depositing $NaAlH_4$ on Ni–containing porous carbon sheets [124]. This was attributed to stronger interactions between the Ni catalyst and $NaAlH_4$.

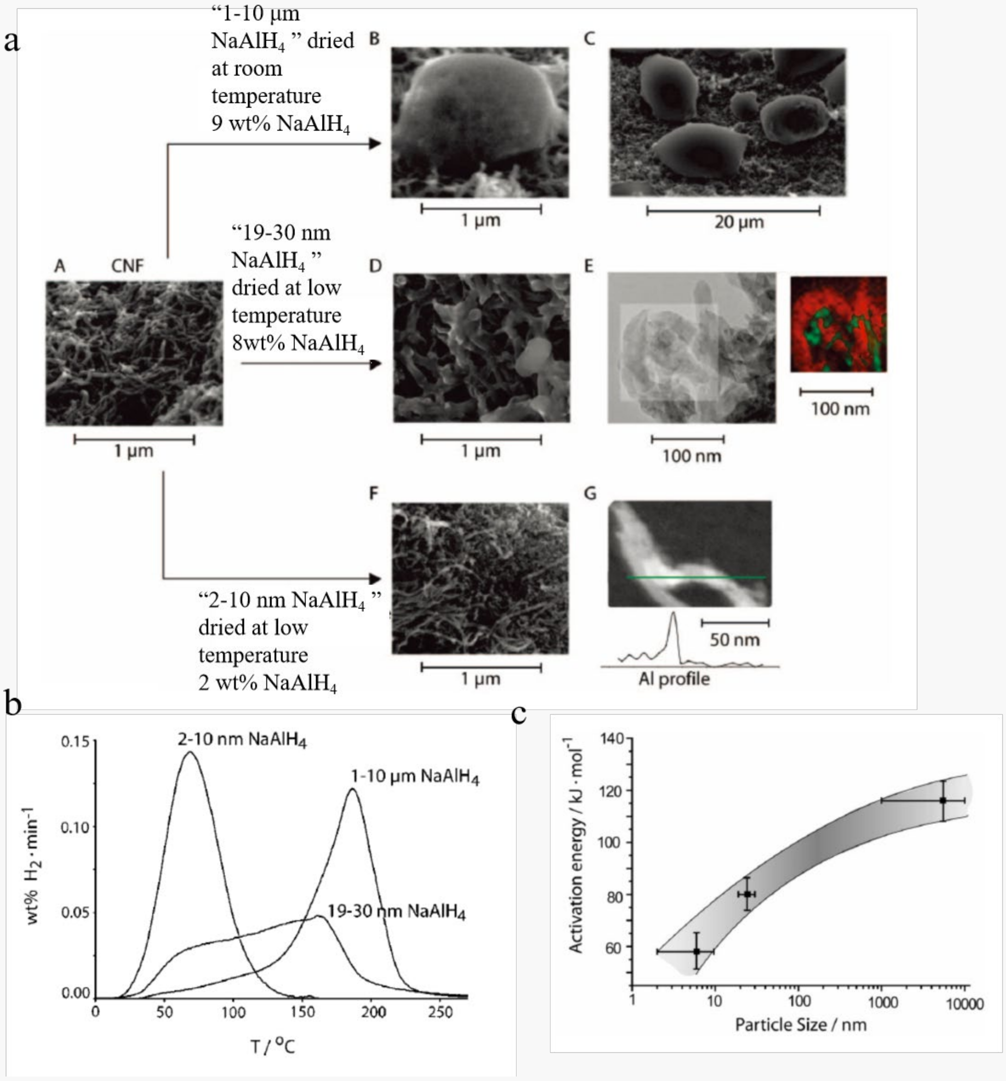

Fig. 10. (a) Overview of $NaAlH_4$/CNF samples. SEM micrographs of (A) CNF skin prior to impregnation, (B–C) SEM micrographs of "1–10 µm $NaAlH_4$" and (D) SEM micrograph of "19–30 nm $NaAlH_4$". (E) TEM and an EDX elemental mapping of a highlighted region (C in red and Al in green) for "19–30 nm $NaAlH_4$" after desorption, (F) SEM micrograph of "2–10 nm $NaAlH_4$", (G) TEM micrographs with Al profile of "2–10 nm $NaAlH_4$" after desorption. (b) Temperature programmed desorption profiles of H_2 of $NaAlH_4$/CNF samples under Ar. Heating rate is 5 °C min^{-1}. (c) Relation between particle size and activation energy for hydrogen desorption from $NaAlH_4$/CNF. The spread in the particle size reflects the results from different characterization techniques, and the error bars in activation energies were obtained from linear regression analysis. Reprinted with permission from ref. [122].

Owing to its high THF–solubility and low melting point (T_m = 181 °C), nanoconfinement through melt infiltration and solution impregnation is frequently resorted to prepare nanostructured $NaAlH_4$. In the solution impregnation process, $NaAlH_4$ dissolved in THF is soaked into the porous host materials through the capillary effect [31]. Melt infiltration is often operated above the melting point under hydrogen backpressure. In 2008, Zheng et al. demonstrated ordered mesoporous silica–confined $NaAlH_4$ prepared by solution impregnation [126]. Compared with the bulk sample, the confined $NaAlH_4$ exhibited a lower temperature and faster kinetics for dehydriding, and rehydriding was achieved at 125–150 °C and 35–55 atm H_2 owing to the space confinement effect. Alternatively, $NaAlH_4$ melt infiltration in microporous activated carbon was conducted at 190 °C under 170 bar H_2 to prevent its decomposition [39]. A decrease of 90 °C was observed between the main decomposition of the nanocomposite to that of bulk $NaAlH_4$. Subsequently, a variety of nanoporous scaffolds have been investigated, including carbon aerogels [126–128], ordered mesoporous carbon [129,130], high specific area carbon [131–135], activated carbon fibers [136], carbon nanotubes [137], graphene nanosheets [138,139], metal–organic frameworks (MOFs) [140], CeO_2 hollow nanotubes [141], and nanoporous Raney Ni [142]. Stephens et al. observed reasonable dehydriding kinetics at 150 °C after melt infiltration of $NaAlH_4$ into 13–nm pore–sized carbon aerogel and ~85% of rehydrogenation at ~160 °C and 100 bar H_2 [127]. Nielsen et al. revealed a linear correlation between the pore size and crystalline domain size when melt–infiltrating $NaAlH_4$ in resorcinol formaldehyde carbon aerogels (pore size: 4–100 nm), which induced a ~90 °C of reduction in the peak dehydrogenation temperature [127]. Interestingly, the hydrogen desorption onset temperature was further reduced to 33 °C, and the hydrogen desorption attained a maximum rate at 125 °C when doping resorcinol formaldehyde carbon aerogels with 3 wt.% $TiCl_3$ [128]. This can be ascribed to the favorable synergetic effects between nanoconfinement and catalyst addition. When using high specific surface area carbons as scaffolds, $NaAlH_4$ loading was increased to 20 wt.%, which also presented a significantly improved dehydrogenation behavior with H_2 release commencing at approximately 110 °C, and attaining its maximum rate at approximately 180 °C [131]. N–doping induced a further lowering of the activation energy for H_2 desorption by nearly 70 $kJ \cdot mol^{-1}$ [135]. Similarly, $NaAlH_4$ embedded in ordered mesoporous carbon exhibited a reduction in activation energy by ~70 $kJ \cdot mol^{-1}$ and > 80% high–capacity retention after 15 cycles [129]. The activation energies for confined $NaAlH_4$ dehydrogenation were further decreased to ~22 and 40 $kJ \cdot mol^{-1}$ when N–doped ordered mesoporous carbon with 1–2 nm and 8–10 nm pores were used as scaffolds, respectively [130]. This triggered hydrogen desorption commencing at below 50 °C, and the peak temperature was approximately 80 °C, which was lowered by 100 °C compared with that of bulk $NaAlH_4$. With active carbon fibers and graphene nanosheets as host matrices, $NaAlH_4$ loading increased to 48 wt.% and 50 wt.%, respectively. Huang et al. successfully encapsulated $NaAlH_4$ nanoparticles in graphene nanosheets through a facile solvent evaporation induced deposition method [138]. Results on morphology observation, EDS analysis and hydrogen storage performance are shown in Fig. 11. Exploiting the uniform distribution of $NaAlH_4$ on graphene with intimate contact and the significant reduction of particle size down to ~12.4 nm, the nanoconfined sample exhibited an onset temperature of 100 °C, which is 80 °C below that of its bulk counterpart, and hydrogen desorption was significantly accomplished below 200 °C [138]. Although a 90 wt.% of $NaAlH_4$ loading was also reported, the desorption peak temperature was found to be ~230 °C, significantly higher than that of known low–loaded samples [139].

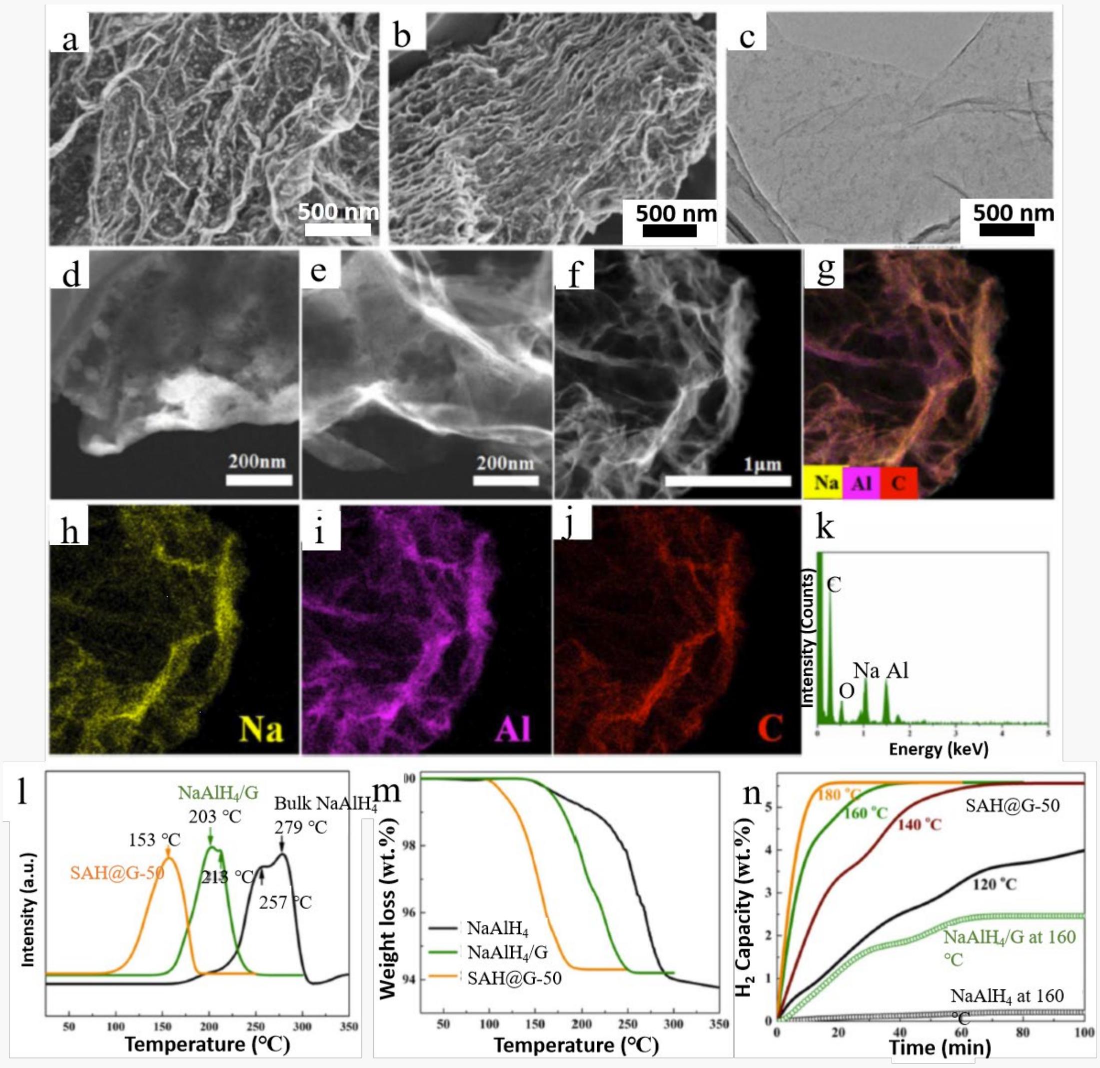

Fig. 11. (a–b) FE-SEM images, (c) TEM images, (d–f) STEM images of $NaAlH_4$ encapsulated in 50% graphene (SAH@G–50). (g) Elemental mapping, (h–j) the corresponding elemental mapping of Na, Al, and C, and (k) the EDX spectrum of SAH@G–50 composite. (l) Mass spectra and (m) thermogravimetric analysis curves of the as-prepared SAH@G–50 compared with bulk $NaAlH_4$ and the ball–milled composite of $NaAlH_4$ and graphene ($NaAlH_4$/G). (–) Isothermal dehydrogenation of SAH@G–50 in comparison with $NaAlH_4$ and the ball–milled $NaAlH_4$/G composite at various temperatures. Reprinted with permission from ref. [138].

Nanoporous metal–organic frameworks (MOFs) were also employed as scaffolds to confine $NaAlH_4$. Using the MOF HKUST–1 as a template, Bhakta et al. reported that $NaAlH_4$ nanoclusters as small as eight formula units were synthesized, which dramatically accelerated the desorption kinetics, leading to decomposition occurring at ~100 °C lower than for bulk $NaAlH_4$ [143]. The desorption activation energy is barely 53 $kJ\cdot mol^{-1}$, which is 60 $kJ\cdot mol^{-1}$ lower than that of its bulk counterpart [140]. Stavila et al. demonstrated that $NaAlH_4$ confined within the Ti–functionalized MOF template MOF–4(Mg) nanopores achieved loadings close to 21 wt.% and a hydrogen desorption onset of ~50 °C [144]. In particular, Ti is necessary to achieve fully reversible rehydriding. Recently, Gao et al. employed CeO_2 hollow nanotubes prepared using a simple electrospinning technique as functional scaffolds to support $NaAlH_4$ nanoparticles towards advanced hydrogen storage performance [141]. Fig. 12 illustrates the morphology, element distribution and desorption performance of the resultant sample. The onset dehydrogenation temperature was reduced to below 100 °C, exhibiting only one main dehydrogenation peak appearing at 130 °C. This remarkable improvement was mainly attributed to the role of CeO_2 hollow nanotubes, which functioned not only as a structural scaffold for confining $NaAlH_4$ NPs, but also as an effective catalyst for enhancing hydrogen storage performance. Moreover, Li et al. synthesized porous Raney Ni with a 3–nm pore size incorporated with $NaAlH_4$ [142], enabling one step dehydrogenation commencing at approximately 85 °C with an activation energy of barely ~20 $kJ\cdot mol^{-1}$. The dehydrogenated products were readily regenerated back to $NaAlH_4$ at 150 °C and 70 atm H_2. Again, these remarkable enhancements were ascribed to the shorter diffusion routes by confining the nanoporous supports and abundant catalytic sites of metallic Ni.

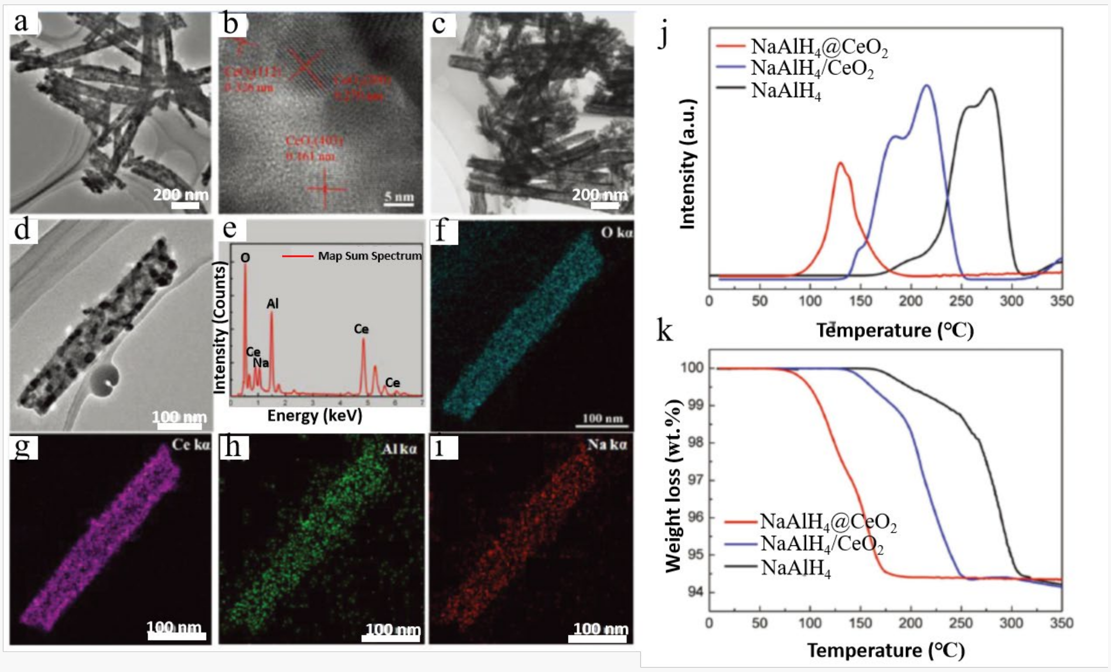

Fig. 12. (a) TEM images of CeO_2 nanotubes, (b) HRTEM image of CeO_2, (c–d) $NaAlH_4@CeO_2$, (e–i) EDS spectrum and the corresponding EDS maps of O, Ce, Al and Na elements for (d) image. (j) MS curves and (k) TG curves for bulk $NaAlH_4$, $NaAlH_4/CeO_2$, and $NaAlH_4@CeO_2$, with a heating rate of 5 °C min^{-1}. Reprinted with permission from ref. [141].

3.2.2 Other nanostructured alanates

In addition to $NaAlH_4$, other alanates such as $LiAlH_4$, $Mg(AlH_4)_2$, and $Ca(AlH_4)_2$ have attracted attention owing to their high gravimetric hydrogen density. In 2014, Wahab et al. impregnated $LiAlH_4$ into homogeneously dispersed Ni–containing mesoporous carbon scaffolds, which decreased the onset desorption temperature by 84 °C to 66 °C [145]. Zhao et al. also reported an enhanced $LiAlH_4$ dehydrogenation performance for supported TiO_2/hierarchically porous carbon nanocomposites prepared using a one–step solvent method, which commenced releasing hydrogen at 64 °C, approximately 100 °C lower than the corresponding temperature of pure $LiAlH_4$ [146]. More encouragingly, the partial reversibility of hydrogen storage in $LiAlH_4$ was realized when confined to high–surface–area graphite [148] and N–doped CMK–3 carbon [148]. Notably, the resultant $LiAlH_4$@NCMK–3 released H_2 at temperatures as low as 126 °C with complete decomposition below 240 °C, bypassing the usual Li_3AlH_6 intermediate observed in the bulk. More importantly, $LiAlH_4$ exceeding 80% was regenerated under 100 bar H_2 at 50 °C, which is usually perceived to be impossible, consequently representing a crucial breakthrough in reversible hydrogen storage using $LiAlH_4$. Nitrogen sites are assumed to be critical for these improvements, as no reversibility was observed for N–free CMK–3.

In 2007, Varin et al. synthesized 18-nm nanocrystalline $Mg(AlH_4)_2$ via mechanochemical reaction between $NaAlH_4$ and $MgCl_2$, enabling hydrogen desorption at 125 °C [149]. Using a similar preparation strategy, $Mg(AlH_4)_2$ nanoparticles with a particle size below 10 nm were successfully synthesized using $LiAlH_4$ and $MgCl_2$ as raw materials, together with a LiCl buffering additive [150]. The resultant nanoparticles exhibited faster hydrogen desorption kinetics and lower desorption temperatures than bulk $Mg(AlH_4)_2$. Hydrogen desorption commenced at 80 °C for the $Mg(AlH_4)_2$ nanoparticles, which is approximately 65 °C lower than that for $Mg(AlH_4)_2$ microparticles. Similar changes were observed for $Ca(AlH_4)_2$ [151]. Alternatively, Pang et al. demonstrated a unique mechanical–force–driven physical vapor deposition method for preparing 20–40 nm $Mg(AlH_4)_2$ nanorods without any scaffolds or supports [152]. Fig. 13 illustrates schematically the preparation process, morphology and hydrogen cycling of the resultant Mg(AlH4) nanorods. The onset dehydrogenation temperature of $Mg(AlH_4)_2$ nanorods was reduced by 30 °C. Approximately 4.7 wt.% of hydrogen was liberated from the $Mg(AlH_4)_2$ nanorods within 30 min at 120 °C. In contrast, only 0.7 wt.% of hydrogen was released from the microrods under identical conditions. Further cycling measurements identified the stability with a 2.2 wt.% reversible capacity of the dehydrogenated $Mg(AlH_4)_2$ nanorods over the first five cycles. Consequently, the reversible hydrogen storage properties of $LiAlH_4$, $Mg(AlH_4)_2$ and $Ca(AlH_4)_2$ require enhancement.

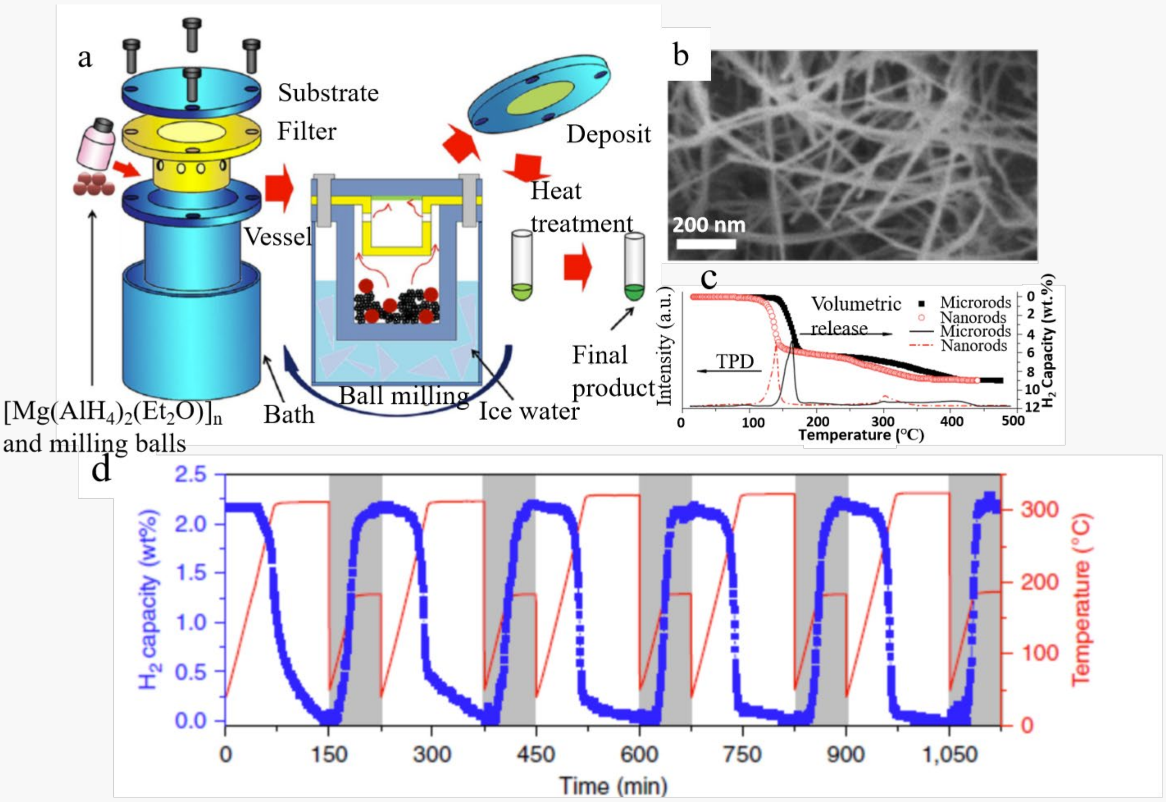

Fig. 13. (a) A schematic diagram of the $Mg(AlH_4)_2$ nanorod preparation process. (b) SEM image of the resultant product. (c) Hydrogen desorption performance of $Mg(AlH_4)_2$ microrods and nanorods. (d) Hydrogen desorption/absorption cycle curves of $Mg(AlH_4)_2$ nanorods. Reprinted with permission from ref. [153].

3.3 Nanostructured metal borohydrides

Compared with alanates, metal borohydrides are preferable for hydrogen storage applications because of their higher hydrogen content. However, stronger B–H binding and lower reactivity of B toward H_2 lead to harsher conditions for reversible hydrogen storage. Lithium borohydride, $LiBH_4$, occurs as a white solid at room temperature with 18.5 wt.% H; therefore, it is regarded as a highly promising solid–state material [20,153,154]. However, its standard formation enthalpy ($\Delta_f H^0$) is –190.8 kJ·mol^{-1} [155], representing a high thermodynamic stability owing to the strong and highly directional covalent and ionic bonds within $LiBH_4$ structure [156,157]. This induces $LiBH_4$ decomposition only above 400 °C. The reported $LiBH_4$ formation from LiH and B requires harsher conditions, for example, 600 °C/350 bar H_2 or 700 °C/150 bar H_2 [27,28]. This primarily originates from the low reactivity of elemental B toward H_2, making it very challenging to form B–H bonds. It is necessary to reduce the reaction temperature, enhance the kinetics, and improve reversibility by tailoring the thermodynamics and kinetics of hydrogen storage in $LiBH_4$ before it can be practically used. A considerable number of studies have been conducted to address this problem using nanostructuring. Theoretical studies pointed out that the removal of hydrogen from the surface of the $LiBH_4$ clusters and nano–whiskers is relatively easier than from bulk crystals [158]. The predicted critical sizes of the nano-cluster and nano-whisker for α-$LiBH_4$ were 1.75 and 1.5 nm, respectively. Further reaction–energy calculations also indicated that only very small clusters (<1 nm) were significantly destabilized in comparison with the bulk [159]. In contrast to bulk systems, the calculated pressure–composition isotherms displayed sloping plateaus for the $LiBH_4$ nanoclusters, possibly due to finite size effects on reaction thermodynamics [160]. Table 3 summarizes the synthesis process and hydrogen storage properties of nanostructured borohydrides.

3.3.1 Nanostructured $LiBH_4$

Generally, nanostructured $LiBH_4$ is readily obtained by confining it to host porous structures. In 2008, Gross et al. reported enhanced kinetics by incorporating $LiBH_4$ into a nanoporous carbon aerogel with a 13–nm average pore size [164]. Dehydrogenation rates up to 50 times faster than those of the bulk material were observed at 300 °C. The measured activation energy for hydrogen desorption was reduced from 146 $kJ \cdot mol^{-1}$ for bulk $LiBH_4$ to 103 $kJ \cdot mol^{-1}$ for nanostructured $LiBH_4$, which resulted in 75 °C reduction in desorption temperature. Using the solution impregnation method, Fang et al. demonstrated that $LiBH_4$ incorporated into an activated carbon (AC) scaffold having a pore size of ~3.2 nm desorbed hydrogen at 220 °C, which was 150 °C lower than when bulk $LiBH_4$ did [164]. Moreover, the $LiBH_4$/AC sample desorption rate was one order of magnitude higher than that of the bulk $LiBH_4$. Cahen et al. observed a hydrogen release of 3.4 wt.% in 90 min at 300 °C for $LiBH_4$ confined in mesoporous carbon having a pore diameter of approximately 4 nm, whereas bulk $LiBH_4$ decomposition was insignificant at identical temperature [165]. In stark contrast to bulk $LiBH_4$, hydrogen release proceeded in a single step without intermediate formation, such as in dodecaborane. Such a modification of the hydrogen release mechanism has never been reported for confined $LiBH_4$ nanoparticles.

Ngene et al. demonstrated that hydrogen melt infiltration is an effective method for synthesizing $LiBH_4$ incorporated into ordered mesoporous SiO_2 (SBA–15) [166]. The confined $LiBH_4$ exhibits enhanced hydrogen desorption properties, with desorption commencing at 150 °C. Sun et al. observed rapid hydrogen release of $LiBH_4$ at ~100 °C after confining $LiBH_4$ into SBA–15 with ~9 nm pore sizes [167]. Unfortunately, hydrogen uptake was undetected in this case. Liu et al. revealed the pore-size effects of nanoconfinement on the structural phase transition, H_2 release and uptake, and emission of toxic diborane (B_2H_6) on $LiBH_4$ desorption [168]. Calorimetry signals of both the structural phase transition and melting of the nanoconfined $LiBH_4$ shifted to lower temperatures and finally vanished below a pore size of approximately 4 nm. With decreasing pore size, a monotonic decrease in the desorption temperature was observed along with a gradual reduction in B_2H_6 partial pressure. This represents a breakthrough in the reversibility of B–based hydrogen storage systems. A loading of up to 40 wt.% of $LiBH_4$ was achieved through melt infiltration into mesoporous aerogel–like carbon, which enabled partial rehydrogenation under relatively mild conditions (300 °C under 100 bar H_2 for 3 h) [169]. $LiBH_4$ supported by surface–oxidized single-walled carbon nanotube was synthesized using ultrasonication–assisted wet impregnation [170]. When hydrogen adsorption/desorption experiments were performed at 100 °C under 5 atm H_2, the highest hydrogen adsorption capacity of 4.0 wt.% was measured in the desorption temperature range of 153–368 °C. Melt infiltration of $LiBH_4$ into activated carbon nanofibers yielded considerable reductions in the onset and main dehydrogenation temperatures to 275 and 305 °C, respectively [171]. Moreover, carbon nanocages (CNCs)–confined $LiBH_4$ commenced releasing hydrogen at 200 °C, with a desorption peaked at approximately 320 °C [172]. The total hydrogen desorption capacity at 550 °C attained 7.18 wt.% of the composite. At 400 °C, 78% of the initial hydrogen capacity was absorbed after five dehydrogenation/hydrogenation cycles. The H_2–desorption rate of $LiBH_4$@CNCs system was nearly 13.3 times higher at 350 °C during isothermal hydrogen desorption, compared with pristine $LiBH_4$. Notably, the actual $LiBH_4$ loading was 50%.

$LiBH_4$ nanoconfinement in the hollow carbon spheres was also tested to assess the effectiveness of melt infiltration and solvent impregnation under identical experimental conditions [173]. Solvent impregnation could lower hydrogen desorption temperatures, and some hydrogen release reversibility was also observed at 300 °C under 6 MPa of H_2 pressure. The desorption peak temperature of nanoconfined $LiBH_4$ decreased to 109 °C, and $LiBH_4$ capacity remained nearly constant after 10 cycles. Wang et al. achieved loading up to 70 wt.% $LiBH_4$ with an onset dehydrogenation temperature as low as 200 °C [174]. The total desorption capacity was measured to be 8.3 wt.% when heated to 400 °C. Approximately 8.1 wt.% H_2 was rapidly released within 25 min at 350 °C. The activation energy was determined to be 129.7 $kJ\cdot mol^{-1}$, which is far below the 179.1 $kJ\cdot mol^{-1}$ for the bulk $LiBH_4$. Moreover, a unique double-layered carbon nanobowl (DLCB)–confined $LiBH_4$ composite with 80 wt.% loading was successfully prepared using melt infiltration, which readily desorbed and absorbed ~8.5 wt.% of H at 300 °C and 100 bar H_2 [175]. Fig. 14 illustrates schematically the melt infiltration process, morphology and dehydrogenation properties of the confined products. Benefiting from carbon's nanoconfinement and catalytic function, this composite released hydrogen at 225 °C, peaking at 353 °C, with a hydrogen release of up to 10.9 wt.%. The dehydriding peak temperature was lower by 112 °C compared with that of bulk $LiBH_4$. Xia et al. designed a solid–liquid followed by solid–gas reaction process and prepared ~4–nm thick $LiBH_4$ nanolayers anchored on graphene, which demonstrated a fast dehydrogenation at 340 °C with a 9.7 wt.% H capacity [176]. A 7.5 wt.% hydrogen capacity was observed after five cycles at 320 °C, corresponding to an 80% capacity retention, which was nearly twice that of $LiBH_4$/G mixture after three cycles. Furthermore, Zhang et al. synthesized a Ni–decorated graphene–supported $LiBH_4$ nanocomposite ($LiBH_4$ nanoparticles: 5–10 nm, Ni nanocrystals: 2–4 nm) and achieved reversible desorption and absorption of ~9.2 wt.% hydrogen at 300 °C under 100 bar H_2 [177]. Fig. 15 indicates TEM image, EDS mapping and hydrogen storage behaviors of the nano–$LiBH_4$ with 10 wt.% Ni and 20 wt.% graphene, which was named as nano–$LiBH_4$/10Ni@20G. The presence of ultrafine Ni nanocrystals effectively prevented a stable $B_{12}H_{12}^{2-}$ cluster formation during hydrogen cycling. After 100 cycles, the hydrogen capacity was approximately 8.5 wt.%, corresponding to 92.4% of capacity retention, representing stable cyclability. This represents an important breakthrough in the long–term cycling of metal borohydrides under mild conditions. This remarkable improvement was mainly attributed to the successful suppression of B_2H_6 by–product evolution and enhanced physical contact between LiH and B after dehydrogenation owing to the synergistic effect of nanostructuring and nanocatalysis.

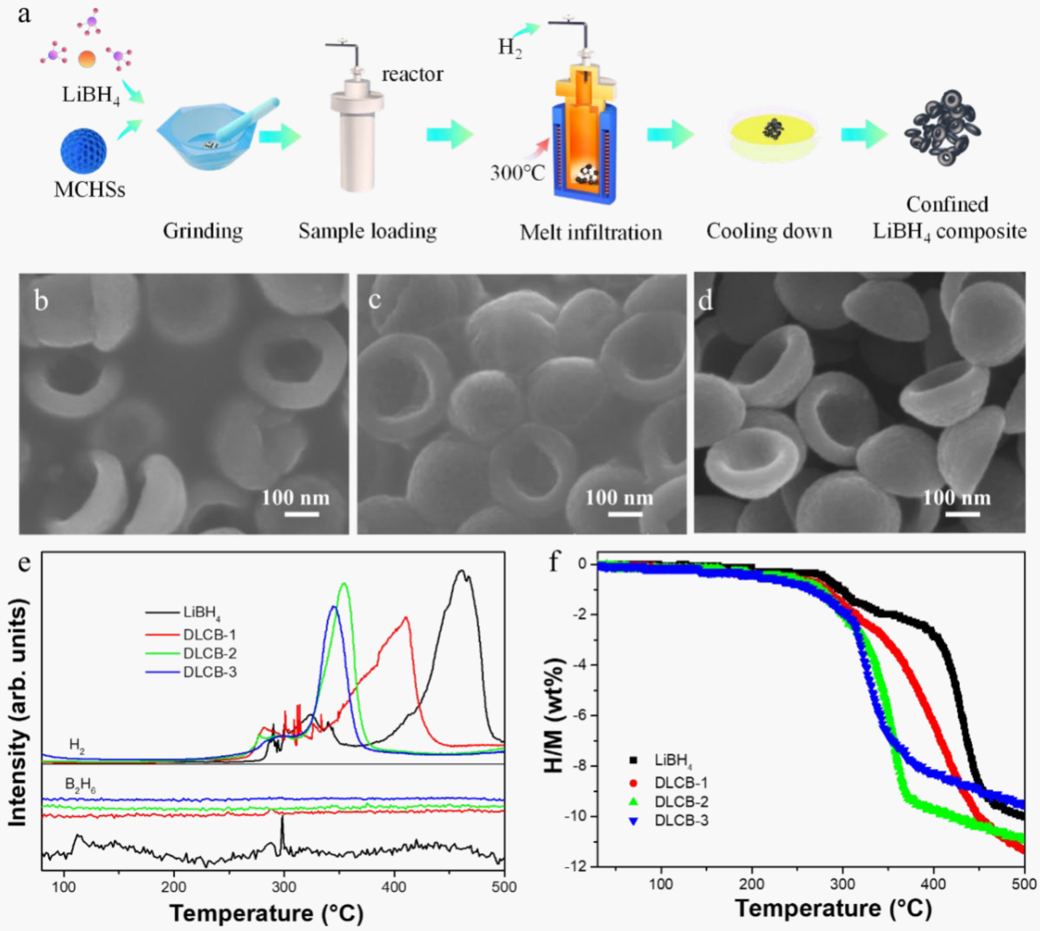

Fig. 14. (a) Schematic illustration of the melt infiltration procedure. (b–d) SEM images of samples with weight ratios of 9:1, 8:2, and 7:3 for $LiBH_4$ to mesoporous carbon hollow spheres (denoted as DLCB–1, DLCB–2 and DLCB–3). (e) TPD-MS and (f) volumetric release curves of samples with different weight ratios of $LiBH_4$ to mesoporous carbon hollow spheres. Reprinted with permission from ref. [175].

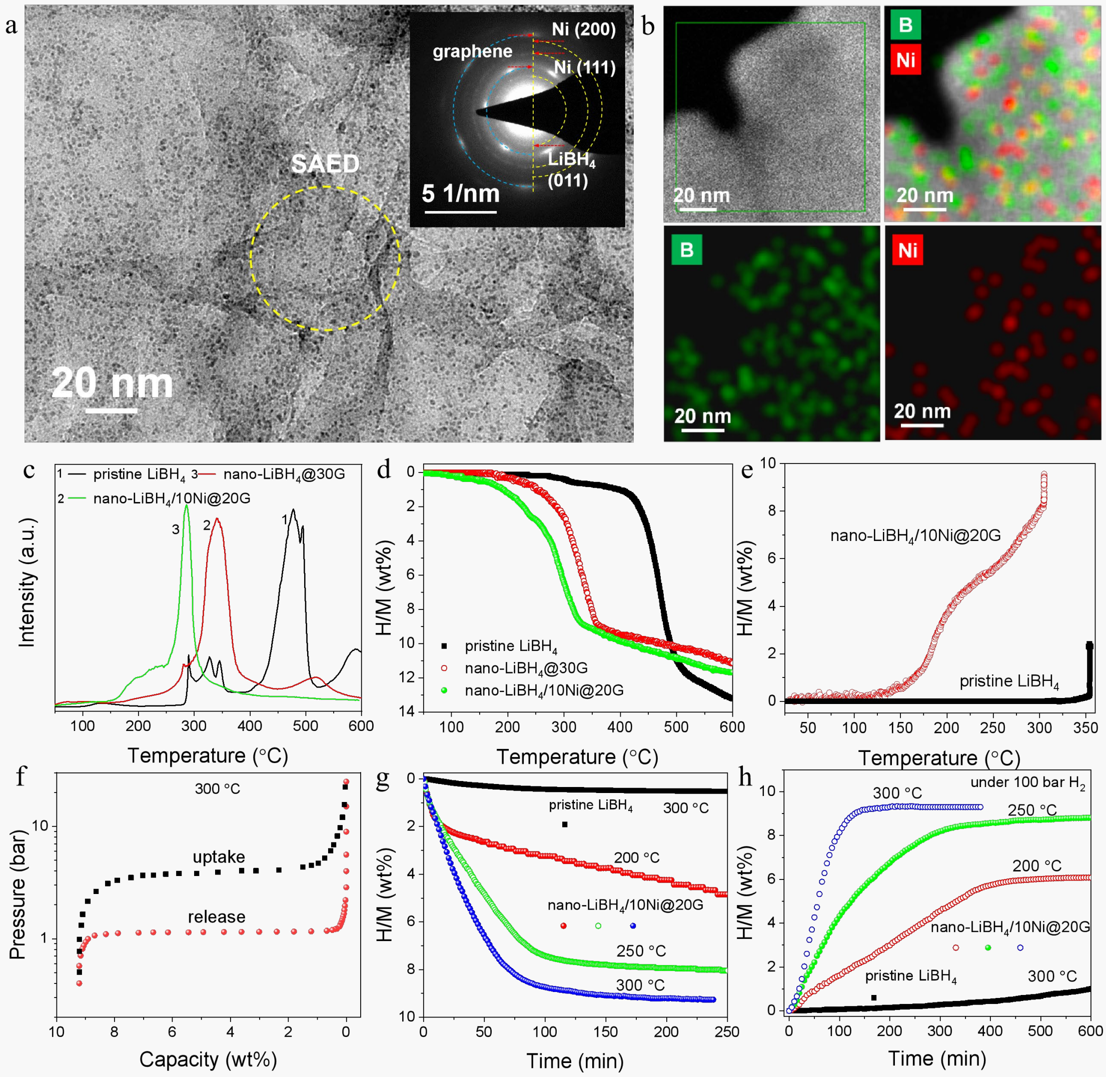

Fig. 15. (a) TEM image and (b) EDS mapping images of nano–LiBH4/10Ni@20G. The insert in (a) is the SAED pattern. (c) TPD–MS, (d) volumetric hydrogen release, (e) non–isothermal hydrogenation, (f) PCI, (g) isothermal dehydrogenation and (h) isothermal hydrogenation curves of nano–LiBH4/10Ni@20G and pristine LiBH4. Reprinted with permission from ref. [177].

Moreover, metal–organic frameworks and 2D MXene have also been used as scaffolds for the nanoconfining $LiBH_4$. Sun et al. reported copper metal–organic frameworks (Cu–MOFs) as scaffolds for loading $LiBH_4$, and nanoconfining $LiBH_4$ in the Cu–MOF pores resulted in a significantly reduced dehydrogenation temperature compared with that of pristine $LiBH_4$. $LiBH_4$@Cu–MOF dehydrogenation commenced around 60 °C, and a total gas release of 0.0048 mol·g^{-1} was measured after heating up to 200 °C [178]. Zang et al. demonstrated significantly enhanced hydrogen storage properties after confining $LiBH_4$ into a novel two–dimensional layered Ti_3C_2 MXene [179]. The initial desorption temperature of $LiBH_4@2Ti_3C_2$ hybrid decreased to 172.6 °C and released 9.6 wt.% hydrogen at 380 °C within 1 h, whereas pristine $LiBH_4$ only released 3.2 wt.% hydrogen under identical conditions. More importantly, the dehydrogenated products were partially rehydrogenated at 300 °C under 95 bar H_2. The nanoconfinement effect resulting from the unique layered structure of Ti_3C_2 prevented $LiBH_4$ particle growth and agglomeration. Ti_3C_2 offered a superior effect in destabilizing $LiBH_4$; the synergetic effect of destabilization and nanoconfinement contributed to the remarkably lowered desorption temperature and improved de–/rehydrogenation kinetics. Similar results were also reported by Fan et al. [180], who discovered that the onset dehydrogenation temperature of $LiBH_4$ + 40 wt.% Ti_3C_2 composite was 120 °C, and approximately 5.37 wt.% hydrogen was liberated within 1 h at 350 °C.

Various novel scaffolds have been synthesized and evaluated to confine $LiBH_4$, including porous metal oxides, porous metal sulfides, and even porous metals and alloys. In 2013, Guo et al. incorporated $LiBH_4$ nanoparticles into mesoporous TiO_2 scaffolds using a chemical impregnation method [181]. The resultant nanocomposites commenced releasing hydrogen at 220 °C, and the maximum desorption peak occurred at approximately 330 °C. Moreover, the composite exhibited excellent dehydrogenation kinetics, with 11 wt.% of hydrogen liberated from $LiBH_4$ at 300 °C within 3 h. Xian et al. prepared a nano–TiO_2 decorated porous amorphous carbon-confined $LiBH_4$ having a 60 wt.% loading, which released 7.3 wt.% H within 60 min at 320 °C, and delivered 5.1 wt.% of reversible capacity after 20 cycles [182]. Wang et al. employed a carbon–wrapped ultrafine Fe_3O_4 skeleton to confine $LiBH_4$, which initiated dehydrogenation at 175 °C and rapidly desorbed 7.8 wt.% H at 350 °C within 30 min [183]. Xu et al. demonstrated that porous bimetal oxide as a template significantly reduced $LiBH_4$ hydrogen desorption temperature and improved its kinetics [184]. The onset desorption temperature of nanoconfined $LiBH_4$ in hierarchical porous $ZnO/ZnCo_2O_4$ was reduced to 169 °C, and the majority of the hydrogen released appeared at 275 °C. In addition, 8.7 wt.% H was released below 500 °C, and the apparent activation energy (E_a) decreased to ~120 $kJ \cdot mol^{-1}$. The improved dehydrogenation properties were attributed to the synergistic effect of nanoconfinement and destabilization by $ZnO/ZnCo_2O_4$ nanoparticles. Similarly, the nanoconfined $LiBH_4$ in porous $NiMnO_3$ microspheres released hydrogen at 150 °C, with a maximum desorption temperature of 300 °C [185]. Also, the $LiBH_4$@$NiMnO_3$ composites exhibited excellent dehydrogenation kinetics as 2.8 wt.% hydrogen was released within 1 h at 300 °C with a 129.8 $kJ \cdot mol^{-1}$ of apparent activation energy. With CuS hollow nanospheres as scaffolds, the sample commenced hydrogen release below 100 °C, and 80% capacity for $LiBH_4$@CuS was attained within ~20 min [186]. A novel porous Mg scaffold was synthesized to confine and destabilize $LiBH_4$ [187]. The sample exhibited a desorption onset temperature at 100 °C, 250 °C lower compared with bulk $LiBH_4$. The melt–infiltrated $LiBH_4$ in porous Al scaffold with 56 ± 20–nm pore size exhibited a low onset hydrogen desorption temperature of 100 °C and enhanced hydrogen desorption kinetics [188]; when heated to 550 °C, it released 5.86 wt.% H. Chen et al. prepared a nanoporous Ni–based alloy by immersing $Mn_{70}Ni_{30}$ alloy in $(NH_4)_2SO_4$ solution, and then incorporated $LiBH_4$ to construct an $LiBH_4$/np–Ni composite at a mass ratio of 1:5 [189]. The composites desorbed hydrogen at approximately 70 °C and concluded before 400 °C. The apparent dehydrogenation activation energy was found to be only 11.4 kJ·mol^{-1}. However, the practical hydrogen capacity was reduced to below 2 wt.% due to the scaffold. Graphene entanglement in a mesoporous resorcinol–formaldehyde matrix has also been applied to confine $LiBH_4$ [190,191]. The desorption temperature was reduced to 253 °C in graphene's presence, which was further lowered by 10 °C by N–doping. Naresh Muthu et al. demonstrated 2.3 wt.% of hydrogen storage capacity at 100 °C for activated hexagonal boron nitride supported $LiBH_4$ ($LiBH_4$@Ah–BN) nanocomposite [192]. The E_a values were measured to be 19.91 kJ·mol^{-1} at the desorption temperatures, which is sufficiently small for hydrogen desorption. In addition, the onset dehydrogenation temperature for $LiBH_4$ decreases by 190 °C when $LiBH_4$ was confined to CeF_3–modified activated carbon (AC-CeF_3) [194]. The maximum dehydrogenation rate of $LiBH_4$–AC–CeF_3 was 288 times higher than that of pristine $LiBH_4$ at 350 °C.

To maximize the reversible hydrogen capacity, attempts have been made to synthesize freestanding $LiBH_4$ nanostructures [153,195–198]. For instance, $LiBH_4$ nanobelts with widths of 10–40 nm were successfully synthesized using $[LiBH_4(MTBE)]_n$ (MTBE: methyl tert-butyl ether) as the precursor via the mechanical force-driven physical vapor deposition method [153]. Hydrogen desorption commenced at 60 °C during temperature-programmed desorption measurements, indicating a significant reduction in the dehydrogenation temperature. Using the solvent evaporation strategy, $LiBH_4$ nanoparticles with sizes ranging from 10.6 to 147.4 nm, stabilized by poly(methl methacrylate), were obtained [194]. The particle size strongly depends on $LiBH_4$ concentration in THF. The main peak for dehydrogenation shifted from 488 °C for bulk sample to 72 °C for the ∼10–nm sample. These results link the dehydriding properties to $LiBH_4$ particle sizes. Wang et al. reported the synthesis of $LiBH_4$ nanoparticles through solvent evaporation, which were stabilized using surfactants [195]. The growth and stabilization of the $LiBH_4$ nanoparticles were reasonably related to the chain length, steric hindrance, and ability of the surfactant head group to bind strongly to $LiBH_4$. Although no drastic reduction in hydrogen desorption temperatures was observed upon surfactant usage, much hydrogen release was achieved below 400 °C, which is an improvement compared with pristine $LiBH_4$. Furthermore, using a modified ternary anti–precipitation method, $LiBH_4$ nanoparticles were successfully synthesized [196]. Here, the carbon chain length of stabilizing surfactant was found to help with particle size control because of the resulting steric hindrance. A remarkable decrease in hydrogen release temperature, while transitioning from > 500 to 360–440 °C, was observed. Interestingly, Zhang et al. recently reported 12 wt.% reversible hydrogen storage at 400 °C for $LiBH_4$ hierarchical nanostructures prepared using single-pot solvothermal synthesis [197]. The hierarchical nanostructured $LiBH_4$ primarily comprised 50–60 nm–sized primary nanoparticles. The considerably reduced particle sizes and porous agglomeration structure resulted in the dehydrogenation prior to melting and effectively suppressed foaming, consequently facilitating cyclability.

3.3.2 Nanostructured $Mg(BH_4)_2$

$Mg(BH_4)_2$, which has a high gravimetric hydrogen density (14.9 wt.%) and volumetric hydrogen density (112 $g\cdot H_2\cdot L^{-1}$), is also regarded as a promising candidate for hydrogen storage. According to first-principles calculations, the higher the Pauling electronegativity (χ_p), the weaker the B–H bond strength in $M(BH_4)_n$. It is therefore believed that compared with Na, Li, and Ca ions (χ_p = 0.93, 0.98, and 1.00, respectively), Mg ions with greater χ_p (χ_p = 1.31) should effectively weaken the B–H covalent bonds [198]. However, various reports indicated that $Mg(BH_4)_2$ starts releasing hydrogen at approximately 275 °C and attains its hydrogen release peak when the temperature is increased to 375 °C [199,200]. In particular, $Mg(BH_4)_2$ formation through directly hydriding of MgB_2 requires a high temperature of 400 °C and ultrahigh hydrogen pressure of 950 bar [201]. Therefore, it is challenging to achieve reversible hydrogen storage using $Mg(BH_4)_2$ under mild conditions.

In 2007, Li et al. reported the effects of ball milling on the dehydriding behavior of well–crystallized $Mg(BH_4)_2$ [202]. Few changes were observed in the samples after 5 h of ball milling. Furthermore, amorphous $Mg(BH_4)_2$ was synthesized in situ by ball milling MgB_2 under 100 atm H_2 or $LiBH_4$ with $MgCl_2$ [203,204]. The onset dehydrogenation temperature of the sample obtained using the mechanochemical reaction of $LiBH_4$ with $MgCl_2$ was approximately reduced by 156 °C relative to pristine $Mg(BH_4)_2$ [204]. Similar results were observed for a sample prepared from the reaction of $NaBH_4$ with $MgCl_2$ [205]. The dehydriding reaction commenced at approximately

227 °C, and a weight loss of approximately 14.4 wt.% was observed up to 527 °C; only hydrogen was detected during the measurements. When replacing $MgCl_2$ with $MgBr_2$, the reaction time was considerably shorter, and the excess $MgBr_2$ served as an additive, lowering the hydrogen release onset temperature from 290 °C to ~220 °C [207].

Attempts have been made to reduce the $Mg(BH_4)_2$ particle sizes by nanoconfinement. Nanoconfinement not only limits particle growth and aggregation but also generates a shorter diffusion path with a lower energy barrier for hydrogen desorption from $Mg(BH_4)_2$. In 2009, Fichtner et al. reported for the first time the kinetic properties of $Mg(BH_4)_2$ infiltrated into activated carbon [208]. A wet incipient impregnation procedure was employed to infiltrate $Mg(BH_4)_2$ into the voids of pre–treated activated carbon having a pore diameter under 2 nm. The loading amount of $Mg(BH_4)_2$ was estimated to be ~44 wt.%. Thermogravimetric analysis (TGA) together with mass measurements revealed that hydrogen desorption commenced at 170 °C and amounted to 6 wt.% when heated up to 500 °C. Subsequently, ordered mesoporous carbon with uniform pores (~3.5 nm) was utilized as a scaffolds to confine $Mg(BH_4)_2$ [208]. A noticeable low–temperature shift was also observed for desorption, wherein the onset of hydrogen gas evolution took place at approximately 110 °C and attained a maximum rate at approximately 200 °C. By combining nanoconfinement (CMK–3) and Ni catalyst, the onset dehydrogenation temperature was reduced to only 75 °C (measured by TPD) and peaked at 155 °C, but they exhibited values of 270 °C and above 350 °C, respectively, for pure $Mg(BH_4)_2$ [209]. The in situ growth of nanoconfined and highly dispersed Ni nanoparticles throughout the mesoporous carbon framework further decreased the onset dehydrogenation temperature to ~44 °C with a peak temperature of 141 °C, a remarkable reduction of approximately 226 °C relative to pristine $Mg(BH_4)_2$ [210]. With Ni–Pt core–shell nanoparticles as catalysts, Clémençon et al. observed complete hydrogen release from mesoporous carbon–confined $Mg(BH_4)_2$ within 2 h at 350 °C [211]. By ball milling of MgH_2 nanoparticles supported on carbon aerogel in a B_2H_6/H_2 atmosphere, Yan et al. synthesized $Mg(BH_4)_2$/carbon nanocomposites, which exhibited a lower kinetic barrier [212]. The major hydrogen desorption occurred at 160 °C. More importantly, reformation of $Mg(BH_4)_2$ was achieved at 200 °C under 80–150 bar H_2. Han et al. synthesized micro-nanostructured hybrids of $Mg(BH_4)_2$ and carbon nanotubes [213]. The 50 wt.% $Mg(BH_4)_2$ loading sample exhibited a nanosized $Mg(BH_4)_2$–layer coating with a thickness of 2–6 nm on the nanotube surfaces, which commenced releasing hydrogen at 76 °C, approximately 200 °C lower compared with that in pure $Mg(BH_4)_2$. At 117 °C, 3.79 wt.% of H was desorbed from this sample within 10 min. The dehydrogenated sample absorbed 2.5 wt.% of H at 350 °C under 100 bar H_2. These results were recently confirmed by Jiang et al. [214].

Graphene has also frequently been employed as a scaffold to adjust the $Mg(BH_4)_2$ particle sizes. Zhang et al. synthesized $Mg(BH_4)_2$ nanoparticles supported on graphene using a space-confined solid–gas reaction [215]. Considering the effects of particle size reduction and the graphene–assisted catalysis, graphene–supported $Mg(BH_4)_2$ nanoparticles demonstrated an onset dehydrogenation temperature of ~154 °C, and a complete dehydrogenation was achieved at temperatures as low as 225 °C, with MgB_2

as the by–product. More importantly, the dehydrogenated sample absorbed 4.13 wt.% H at 300 °C. Recently, Jeong et al. reported nanocrystalline $Mg(BH_4)_2$ supported on atomically thin reduced graphene oxide (rGO) [216]. The resultant γ–$Mg(BH_4)_2$ product exhibited a two-step decomposition profile, commencing at 150 and 270 °C, respectively, with a total weight loss of 10.1 wt.%. The reversible hydrogen storage performance of $Mg(BH_4)_2$ was effectively improved by uniformly building graphene supported heterostructures inside MgH_2 nanoparticles [217]. Fig. 16 gives the preparation process, morphology observation, component analysis and hydrogen desorption curves. By reacting MgH_2 nanoparticles with B_2H_6, homogeneous $Mg(BH_4)_2$@MgH_2 heterostructures with controllable particle sizes were produced, along with a simultaneous decrease in the MgH_2 particle size, which effectively reduced the kinetic barrier. The hydrogen released from $Mg(BH_4)_2$@MgH_2 heterostructure was found to be 6.2 wt.%, with a lower peak temperature of 191 °C. More importantly, the reversible capacity attained a value of 5.3 wt.%, and the capacity retention was 91.1% after eight cycles. It is believed that building heterostructures provides a good opportunity for discovering high–performance hydrogen storage materials for on–board applications.

In addition, Cu_2S hollow spheres were used to confine $Mg(BH_4)_2$ [218]. After confinement, hydrogen was released at a temperature as low as 50 °C and full hydrogen release was completed at 300 °C. Approximately 0.5 wt.% of hydrogen uptake was measured at 300 °C under 6 MPa H_2 by the dehydrogenated $Mg(BH_4)_2$@Cu_2S. MOFs have shown positive effect on the hydrogen storage performance of $Mg(BH_4)_2$.

Schneemann et al. reported that $Mg(BH_4)_2$ incorporated into the pores of a bipyridine–functionalized MOF, UiO–67bpy, released hydrogen at 120 °C and completed hydrogen release at 200 °C [219]. The onset desorption temperature was reduced by approximately 150 °C with respect to the bulk material.

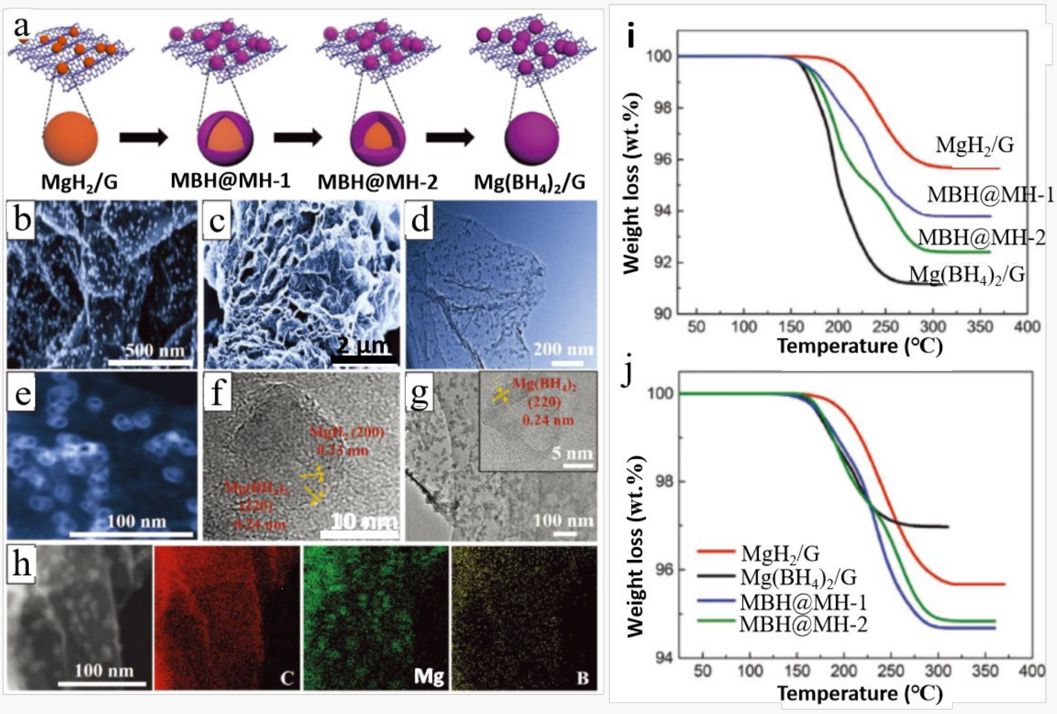

Fig. 16. (a) Schematic illustration of the synthesis of $Mg(BH_4)_2@MgH_2$ NPs on graphene. (b–c) SEM, (d) TEM, (e) STEM, and (f) HRTEM images of MBH@MH-2. (g) TEM image of $Mg(BH_4)_2/G$. (h) Elemental mapping of MBH@MH-2. (i–j) TGA results of MBH@MH–1 and MBH@MH–2 at the first and second dehydrogenation cycles. Reprinted with permission from ref. [217].

3.3.3 Other nanostructured borohydrides

In addition to $LiBH_4$ and $Mg(BH_4)_2$, $NaBH_4$ and $Ca(BH_4)_2$ have recently been studied for their reversible hydrogen storage capabilities. $NaBH_4$ is well–known for its hydrolytic hydrogen evolution properties [220–226]. Millenium Cell Inc. successfully demonstrated an $NaBH_4$–based hydrogen–on–demand prototype system in the Daimler Chrysler's Natrium fuel cell minivan [226]. However, regenerating the hydrolytic product $NaBO_2$ is energy–intensive [227–230]. Recently, Wang et al. reported the synthesis of $NaBH_4$ nanoparticles (approximately 6–260 nm) from $NaOCH_3$ ($NaBH_4$–SUG) [232]. Unfortunately, it is challenging to eliminate these byproducts. Alternatively, $NaBH_4$ nanoparticles can be produced on a carbon support via a mechanochemical reaction between $LiBH_4$ and NaCl [232]. Various carbon–supporting materials including graphite, graphene oxide, and carbon nanotubes have been studied. Major hydrogen desorption from $NaBH_4$ on the carbon supports occurred between 110 and 200 °C, significantly below the corresponding temperature for pure $NaBH_4$ (above 500 °C). Li et al. demonstrated monodispersed $NaBH_4$ nanodots (~6 nm) anchored uniformly onto freshly exfoliated graphitic nanosheets (GNs) using the mechanical force-driven self-printing process [233]. The morphology, microstructure and hydrogen storage performance are shown in Fig. 17. These nano–$NaBH_4$@GNs exhibited favorable thermodynamics (decrease in ΔH by ~45 %), rapid kinetics (beyond six–fold increase) and stable cycling capacity (up to ~5 wt.% for $NaBH_4$) compared with that of micro–$NaBH_4$. Highly–ordered Si–based mesoporous scaffolds and their carbon replicas have also been employed to nanoconfine $NaBH_4$ [234]. The resulting materials displayed two–step gas evolution profiles commencing below 120 °C. The lower desorption temperature is attributed to the morphological conditions and thermodynamic and kinetic improvements achieved via the nanosizing effect. Moreover, $NaBH_4$ nanoconfinement in CuS hollow nanospheres (MBH_4@CuS) induced hydrogen release at room temperature, with a peak at 60 °C, even lower than the desorption temperature observed for confining into carbon nanotubes ($NaBH_4$@CNT, ~100 °C)

[186]. $NaBH_4$@CuS could reversibly store approximately 0.6 wt.% hydrogen at 300 °C with rapid kinetics within approximately 20 min. Surprisingly, $NaBH_4$@CNT required only 150 °C for reversible hydrogen storage, representing the lowest temperature reported for $NaBH_4$ so far.

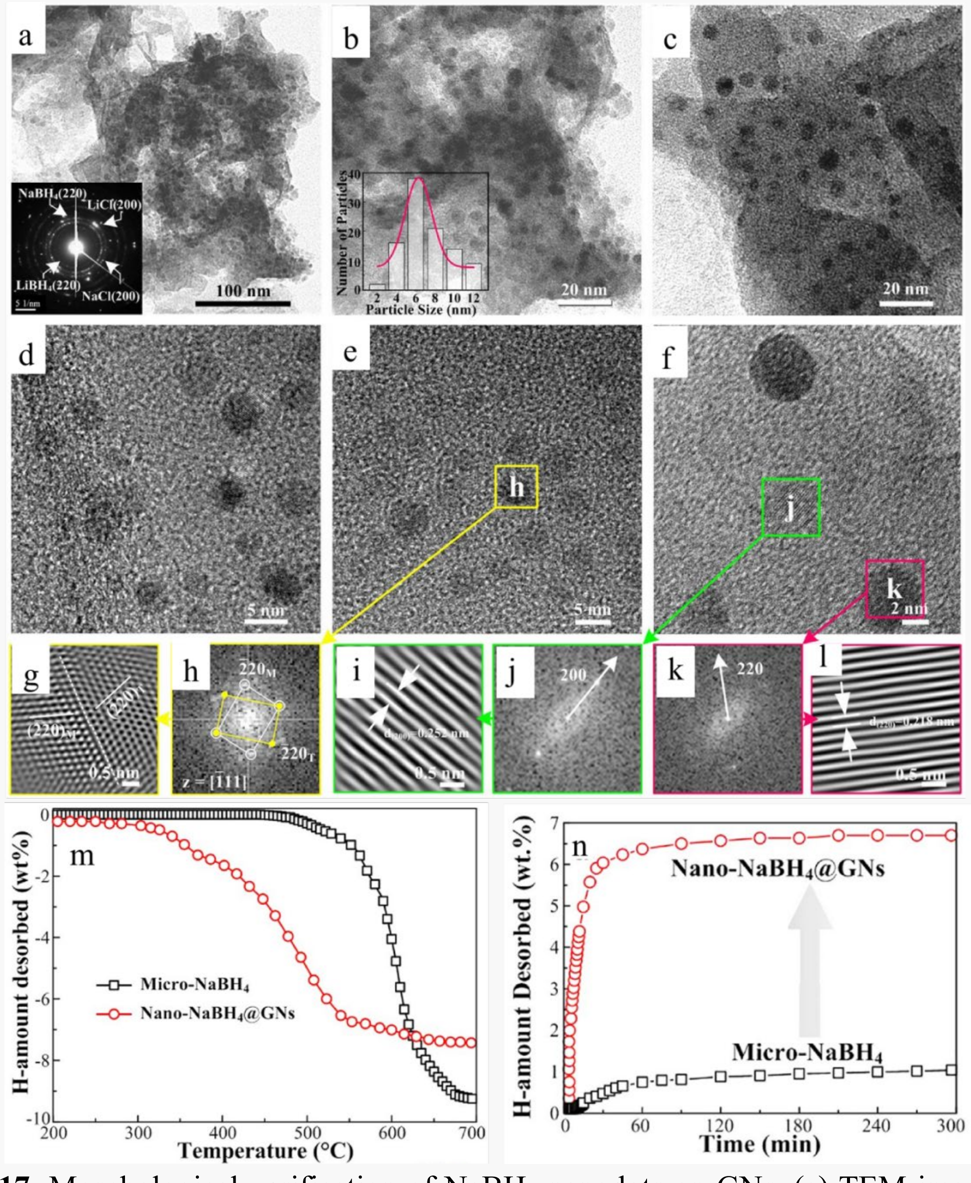

Fig. 17. Morphological verification of $NaBH_4$ nanodots on GNs. (a) TEM image for the nano–$NaBH_4$@GNs and the corresponding selected–area electron diffraction (SAED) pattern (inset of a). (b–c) TEM images of nano–$NaBH_4$@GNs. The corresponding histogram for the particle size distribution of nanodots is shown in the inset of b. (d–f) High–resolution TEM image showing well–dispersed nanodots; (g–l) Atomic lattice image of the square regions in e and f. (h–k) Fast Fourier transform (FFT) digital diffractograms of the nanodomains marked with yellow, green and pink squares in (e,f), respectively. (l) TGA curves for the micro–$NaBH_4$ and nano–$NaBH_4$@GNs

measured at 5 °C min^{-1}. (m) Isothermal hydrogen desorption curves measured at 500 °C. (n) Isothermal hydrogen absorption curves. Reprinted with permission from ref. [233].

As for $Ca(BH_4)_2$, activated mesoporous carbon was often used as a scaffold. $Ca(BH_4)_2$ confined in the CMK–3 ordered mesoporous carbon pores commenced releasing hydrogen at 100 °C [235]. Such improvement was further confirmed by Comănescu et al [236]. Moreover, $Ca(BH_4)_2$ confined into porous Cu_2S hollow spheres commenced releasing hydrogen at 50 °C with a main peak ending at approximately 300 °C and hydrogen release completed at 400 °C, remarkably superior to bulk counterpart.

3.3.4 Nanostructured borohydride–based composites

Use of a $2LiBH_4$–MgH_2 reactive composite as a reversible hydrogen storage material was initiated by Vajo et al. in 2005 [237]. The sample was prepared by ball milling ~1.2 g mixtures for 1 h with a Fritsch Pulversette 6 planetary mill at 400 rpm. The system demonstrated for the first time a 25–kJ·mol^{-1} of H_2 of reduction in the desorption enthalpy change owing to MgB_2 formation instead of pristine B, that is, thermodynamic destabilization. Subsequently, a series of nanostructured $2LiBH_4$–MgH_2 composites were designed and fabricated by taking the advantage of nanosizing and reactive compositing [238–248]. Nielsen et al. obtained a 90 °C reduction in the hydrogen release onset temperature when $LiBH_4$ and MgH_2 nanoparticles were embedded within a nanoporous carbon aerogel scaffold with a D_{max} ~21–nm pore size [238]. Compared with the bulk composite, the $2LiBH_4$–MgH_2 confined within the mesoporous carbon (CMK–3) scaffold host exhibited significantly enhanced dehydrogenation kinetics, but demonstrated a serious loss of hydrogen capacity upon cycling [239]. By direct melt infiltration of bulk $2LiBH_4$–MgH_2 into an inert nanoporous resorcinol–formaldehyde carbon aerogel scaffold, Gosalawit–Utke et al. observed the release of 90% of the total hydrogen storage capacity within 90 min at T = 425 °C and $P_{(H2)}$ = 3.4 bar [240]. The desorption kinetics were further improved by introducing transition–metal catalysts [241–243]. For example, nanoconfined $2LiBH_4$–MgH_2–$TiCl_3$ required only ~1 h to release 95% of the total hydrogen content, whereas nanoconfined $2LiBH_4$–MgH_2 and bulk material required ~ 2.5 and 23 h, respectively [241]. The presence of 0.13 mol $TiCl_4$ significantly lowered the onset dehydrogenation temperature to 140 °C [242].

In 2015, Ding et al. prepared nanostructured $LiBH_4$ and MgH_2 composites using a special ball milling with aerosol spraying (BMAS) [244]. Fig. 18 shows the schematics of the automated BMAS device, SEM image and desorption curves of the resultant samples. The aerosol–sprayed $LiBH_4$ particles were measured to range between 20 and 100 nm. The nanostructured $LiBH_4$–MgH_2 system reversibly released and absorbed ~5.0 wt.% H at 265 °C [245], largely superior to the previously reported results. Three parallel H_2 release mechanisms have been identified: (i) H_2 release from nano-$LiBH_4$ decomposition in addition to the $Li_2B_{12}H_{12}$ decomposition reaction with nano-MgH_2 to produce H_2, (ii) H_2 release from nano-$Mg(BH_4)_2$ decomposition, and (iii) H_2 release from nano-MgH_2 decomposition [246]. Graphene–supported nanostructured $2LiBH_4$–MgH_2 composite with 80% loading was also synthesized and characterized [247]. The well–defined structural features, including even distribution, uniform particle size, excellent thermal stability, and robust architecture, endowed this composite with significantly improved hydrogen storage performance. At temperature of 350 °C, a reversible storage capacity of up to 8.9 wt.% H, without degradation after 25 complete cycles, was achieved for the $2LiBH_4$-MgH_2 anchored on graphene. Recently, a small hydrogen storage tank filled with $2LiBH_4$–MgH_2 nanoconfined in activated carbon was fabricated [248]; a temperature gradient within the tank and poor hydrogen diffusion through the hydride bed were detected. Consequently, further development of hydrogen storage tanks based on $2LiBH_4$–MgH_2 nanoconfined in AC should focus on improving the thermal conductivity, temperature control, and hydrogen diffusion.

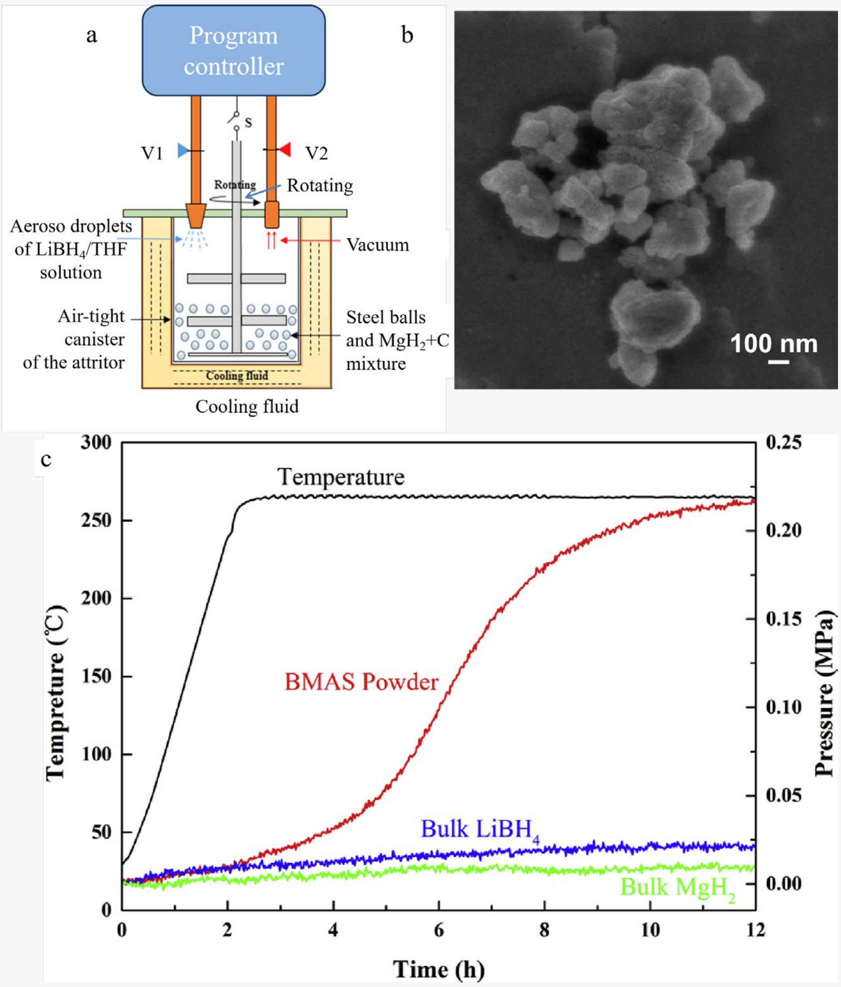

Fig. 18. (a) Schematics of the automated BMAS device. (b) FESEM images of BMAS sample. (c) The dissociation pressure for BMAS sample at 265 °C in comparison with the dissociation pressure of bulk MgH_2 and $LiBH_4$. Reprinted with permission from ref. [245].

Moreover, a ternary $LiBH_4$–MgH_2–$NaAlH_4$ hydride composite confined to a nanoporous carbon host has also been developed for reversible hydrogen storage [249]. The detailed preparation process included three steps: heating the mixture powders to 310 °C at 5 °C/min under 100 bar H_2, dwelling at 310 °C for 45 min, and cooling to room temperature. Nanoconfinement resulted in the one–step decomposition of $LiBH_4$–MgH_2–$NaAlH_4$, and also significantly reduced dehydrogenation temperatures. A $Ca(BH_4)_2$–$LiBH_4$–MgH_2 mixture at a molar ratio of 1 : 2 : 2 also delivered favorable overall hydrogen storage performance, including a relatively narrow temperature range, low dehydrogenation completion temperature, significantly low hydrogenation temperature, and remarkably reduced dehydrogenation temperature after the initial cycle with superior long–term cyclic stability [250]. The hydrogen desorption commenced at 320 °C and concluded at 370 °C, releasing approximately 8.1 wt.% H. Enhanced hydrogen storage properties were discovered for high-loading nanoconfined $LiBH_4$–$Mg(BH_4)_2$ in porous hollow carbon nanospheres [251]. Zhao–Karger et al. observed that the multistep thermal decomposition pattern of the binary $LiBH_4$–$Mg(BH_4)_2$ was altered into a two–step reaction after infiltration into active carbon, and the desorption kinetics were also greatly improved [252]. Similarly, Javadian and Jensen demonstrated the enhanced hydrogen reversibility of nanoconfined $LiBH_4$–$Mg(BH_4)_2$ [253]. In addition, nanoconfined $LiBH_4$–$NaBH_4$, $LiBH_4$–KBH_4, $LiBH_4$–$Ca(BH_4)_2$, $LiBH_4$–$LiAlH_4$ and $LiBH_4$–$NaAlH_4$ were also developed [254–259]. Hydrogen desorption temperature of the $LiBH_4$–$NaBH_4$ nanocomposite was reduced by 100 °C compared with its bulk counterpart [254]. $LiBH_4$–KBH_4 confined in CMK–

3 type carbon exhibited a constant hydrogen uptake of 2.5–3 wt.% for at least five absorption–desorption cycles [256].

3.4 Nanostructured metal–N–H combination systems

In 2002, Chen et al. reported that Li_3N absorbed more than 10 wt.% H to form $LiNH_2$ and 2LiH as potential hydrogen storage systems [260]. Subsequently, a variety of metal amide–hydride (metal–N–H) systems have been studied for hydrogen sorption applications, such as Li–Mg–N–H, Li–Ca–N–H, Li–Al–N–H, Mg–Ca–N–H and Li–B–N–H [261-266]. In contrast to conventional metal hydrides, hydrogen desorption from metal–N–H systems is believed to originate from a direct solid–solid reaction propelled by the strong affinity between $H^{\delta+}$ in amides and $H^{\delta-}$ in hydrides [267]. However, the large kinetic barriers resulted in hydrogen desorption to occur only at temperatures exceeding 200 °C [268]. Through *ab initio* calculations, Yamane et al. reported a strong size dependence for the H_2 desorption reaction between Li_nH_n clusters and NH_3 molecule [269]. The smallest activation energy value was obtained for n = 2. Furthermore, the $Mg(NH_2)_2$ nanoparticles possess remarkably enhanced kinetics for decomposition because there are states filling the band gap of clusters, in addition to the increased surface area [270]. As a result, much effort has been devoted to fabricating nanostructured metal–N–H systems with improved hydrogen storage properties. Table 4 summarizes the synthesis strategies and hydrogen storage properties of nanostructured metal–N–H systems.

3.4.1 Nanostructured Li–N–H systems

Studies have revealed that mechanical ball milling greatly improves the desorption kinetic performance of $LiNH_2$–LiH system because approximately 5 wt.% H is released after 4 h of milling with a lowered on-set hydrogen desorption temperature from 160 to 120 °C [272]. Low–temperature milling, especially at –196 °C, enabled relatively better kinetics compared with ball milling at 20 °C [273]. Further studies indicated 1:1.2 to be optimal molar ratio between $LiNH_2$ and LiH [274]. The nanostructured ($LiNH_2$–1.2LiH) + 5 wt.% Graphite mixture prepared using ball milling for 25 h desorbed/ reversibly absorbed ~5 wt.% H at 325 °C [275]. By using an H_2 plasma–metal reaction followed by nucleation growth, Yang et al. obtained a new ternary $LiNH_2$–LiH–$x$$Mg(BH_4)_2$ nano–composite with particle size range of 200–400 nm and observed a 5.3 wt.% hydrogen desorption at 150 °C [276]. Furthermore, 3D porous carbon–coated Li_3N nanofibers were successfully fabricated via the electrospinning technique, which exhibited significantly enhanced hydrogen storage properties, with a stable reversibility near the theoretical value of 10 dehydrogenation/rehydrogenation cycles at 250 °C [277]. Recently, Wood et al. reported a core–shell Li_3N/[$LiNH_2$+2LiH] nanostructure [278], where nanosizing altered the hydrogenation and dehydrogenation reaction pathways and suppressed undesirable intermediate phases to dramatically improve kinetics and reversibility. Fully reversible hydrogenation/dehydrogenation was observed, with an uptake of ~4 wt.% H at temperatures up to 250 °C.

3.4.2 Nanostructured Li–Mg–N–H systems

The Li–Mg–N–H system composed of $Mg(NH_2)_2$ and LiH exhibited moderate operation temperatures, substantial reversibility, and a relatively high capacity of 5.6

wt.% [261,262]. More importantly, the desorption enthalpy change of the $Mg(NH_2)_2$–2LiH system was found to be ~39 kJ·mol^{-1} H_2, which leads to a desorption temperature of ~90 °C at an equilibrium hydrogen pressure of 1 bar; thereby, it is regarded as a suitable candidate for on–board applications [279,280]. Unfortunately, a reasonable rate of hydrogen desorption was experimentally observed only at temperatures exceeding 200 °C because of the relatively high kinetic barrier. Consequently, numerous studies have been conducted to reduce the activation energy barrier through particle size reduction. In 2009, Liu et al. attempted to understand size–dependent hydrogen storage performance by synthesizing $Li_2MgN_2H_2$ [281]. Fig. 19 displays SEM images and hydrogen storage curves of the resultant $Li_2MgN_2H_2$ after different milling treatments. The 36–h milled sample with 100–200 nm of particle size commenced absorbing hydrogen at only 80 °C, which is 100 °C lower than when hand–milled sample with particle sizes exceeding 800 nm commenced absorbing hydrogen. Furthermore, it was entirely hydrogenated even at a low operating temperature of 160 °C, and the hydrogenated sample exhibited complete dehydrogenation at 215 °C. Xie et al. reported a remarkably reduced activation energy (122.2 kJ·mol^{-1}) when mixing LiH with 100–nm sized $Mg(NH_2)_2$ relative to those measuring 500 and 1000 nm in sizes (134.7 and 182.0 kJ·mol^{-1}, respectively) [282]. Hierarchical porous $Li_2Mg(NH)_2$@C nanowires were successfully fabricated using a single-nozzle electrospinning technique combined with an in situ reaction between the precursors by Xia et al. [283]. The morphology observation and hydrogen storage properties are shown in Fig. 20. The fabricated $Li_2Mg(NH)_2$@C nanowires presented significantly improved thermodynamics and kinetics towards hydrogen storage, e.g., a complete cycle of H_2 uptake and release with a capacity approaching the theoretical value at a temperatures nearing 105 °C. A similar improvement was attained for nanosized $Li_2Mg(NH)_2$ particles inside carbon nanofibers (CNFs) and space–confined into thin–film hollow carbon spheres (THCSs) [284,285]. More importantly, no degradation was observed for $Li_2Mg(NH)_2$/CNFs after 50 de–/hydrogenation cycles at a temperatures as low as 130 °C, indicating excellent reversibility.

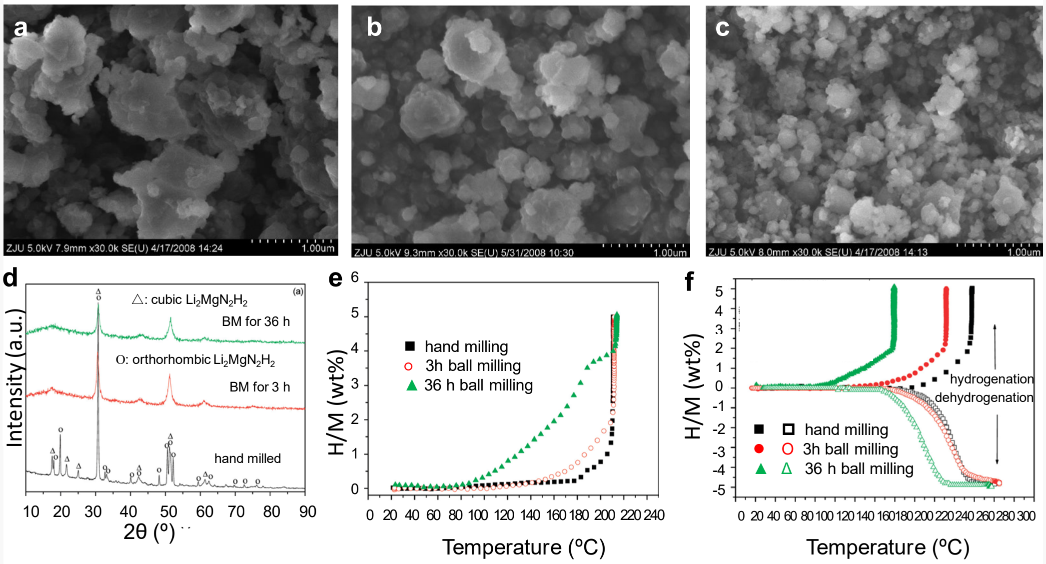

Fig. 19. (a, b, c) SEM images of $Li_2MgN_2H_2$ samples after being hand–milled, and ball–milled for 3 h and for 36 h, respectively. (d) XRD patterns of $Li_2MgN_2H_2$ samples with different treatments. (e) Non–isothermal hydrogenation curves of $Li_2MgN_2H_2$ samples under identical conditions. (f) Hydrogenation/dehydrogenation curves of $Li_2MgN_2H_2$ samples with different milling treatments. Reprinted with permission from ref. [281].

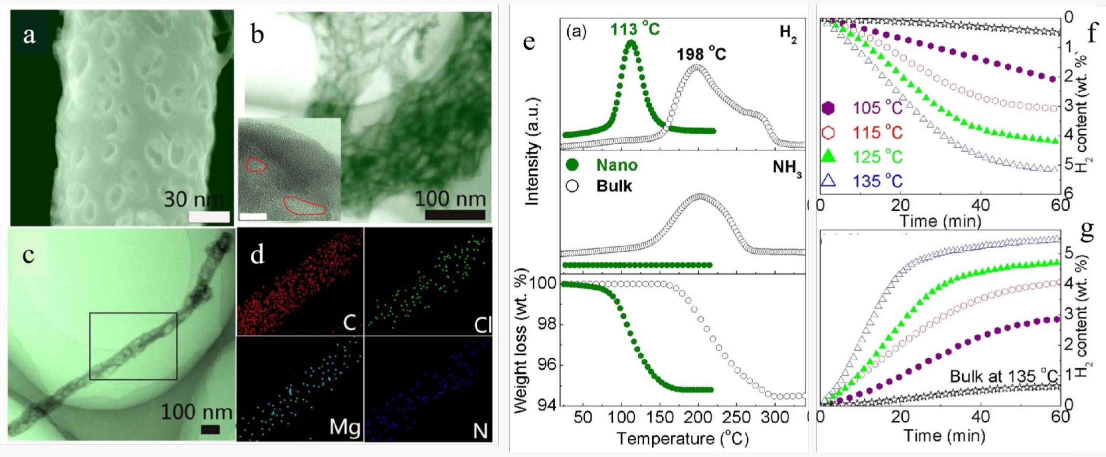

Fig. 20. (a) High–magnification SEM image of a single Li–Mg–N–H nanowire. (b) TEM image of Li–Mg–N–H nanowires (inset: high–magnification TEM image (scale bar 5 nm). (c–d) TEM image and the corresponding elemental mapping of the as-prepared Li–Mg–N–H nanowires. (e) Mass spectra (top) and thermogravimetry curves (bottom) of the carbon–coated Li–Mg–N–H nanowires and bulk $Mg(NH_2)_2/2LiH$ composite after complete hydrogenation. (f–g) Hydrogen desorption and absorption curves of the carbon-coated Li–Mg–N–H nanowires at different temperatures, with the ball-milled $Mg(NH_2)_2/2LiH$ composite at 135 °C included for comparison. Carbon was not considered as an active component for the hydrogen storage measurements. Reprinted with permission from ref. [283].

4. Discussion and future directions

Hydrogen offers a promising solution for the realization of low–carbon and zero–carbon energy systems, especially when hydrogen is produced from renewable resources. However, storage of hydrogen remains challenging, especially when it comes to large–scale demand and long-distance delivery. Taking consideration of the enhanced safety and high energy density, materials–based hydrogen storage is preferred over compression and liquefaction. Light metal hydrides hold great potential for hydrogen storage, but their high thermodynamic stability and kinetic barriers result in high dehydrogenation temperatures, slow kinetics, and poor reversibility. High thermal stability is mainly caused by the strong covalent and ionic bonds, and the kinetic barriers are primarily related to the low catalytic activity of light metals owing to the lack of d electrons.

Nanostructuring effectively enhances the surface-to-volume ratio and reduces the transport distances of mass, charge, and heat. In this review, recent advances in nanostructured light metal hydrides for reversible hydrogen storage are summarized. Nanoconfinement is the most frequently employed approach for controlling the particle size of the resultant hydrides. Graphene sheets–encapsulated Mg nanocrystals with 3.26–nm particle size delivered 6.5 wt.% and 105 g H per liter at 300 °C with a stable cyclability. Ultra–dispersed MgH_2 nanoparticles anchored on 3D $Ti_3C_2T_x$ MXene with a 60 wt.% loading exhibited superior performance, including dehydrogenation from 140 °C and a 4 wt.% of reversible capacity after 60 cycles at 200 °C. Graphene–anchored 4–nm thick $LiBH_4$ nanolayers demonstrated rapid dehydrogenation at 340 °C with a capacity of 9.7 wt.% H. Ni–decorated graphene–supported $LiBH_4$ nanocomposite ($LiBH_4$ nanoparticles: 5–10 nm, Ni nanocrystals: 2–4 nm) displayed reversible desorption and absorption of ~9.2 wt.% hydrogen at 300 °C, superior to those of bulk materials. Nanoconfined hydrides exhibit improved kinetics of hydrogen release and uptake, but dramatic change was only observed when the scaffolds have pore sizes smaller than 2–3 nm. To resolve this problem, isolated ultrafine metal hydride nanoparticles were synthesized. A breakthrough is the formation of freestanding MgH_2 nanoparticles with diameters of 4–5 nm, which delivered reversible hydrogen storage with a capacity of 6.7 wt.% at 30 °C under <50 atm H_2. Moreover, a critical size of 10 nm was experimentally confirmed for the simultaneous alteration of the thermodynamics and kinetics for hydrogen storage in MgH_2. This reveals a new avenue for using MgH_2 as a practical hydrogen storage medium, and also sheds light on the design and development of nanostructured light metal hydrides.

Despite the significantly improved properties through nanostructuring, the operation temperatures, reaction rates, and reversible hydrogen capacities of light metal hydrides cannot satisfy the practical requirements. It remains challenging to balance the thermodynamic and kinetic improvements and to achieve high hydrogen capacities. Therefore, future studies should focus on:

- Fabricating isolated ultrafine nanoparticles (< 10 nm) without scaffolds and supports.
- Understanding the nucleation and growth mechanisms of nanostructures.
- Elucidating the size dependence of hydrogen storage behaviors on cycling.
- Developing new strategies to simultaneously achieve nanosizing and nanocatalysis.

5. Conclusion

This paper reviews the synthesis strategies and hydrogen storage performance of nanostructured light-metal hydrides, including MgH_2, alanates, borohydrides and metal–N–H systems. Mechanical milling is the most frequently used technique to reduce particle sizes. However, only limited sizing effect was obtained because mechanical milling can hardly produce particles below 100 nm owing to the continuous fracturing, agglomeration, and cold-welding. Mechanochemical reaction, hydrogenolysis and thermolysis of Grignard reagents as well as physical and chemical vapor deposition are effective in the formation of different dimensional MgH_2/Mg nanostructures, ranging from 0D, 1D, 2D to 3D. As for complex hydrides, nanoconfinement via solution impregnation and melt infiltration is particularly effective, due to their high solubility in organic solvents and their relatively low melting points. Most importantly, the ultrasound–driven liquid–solid reaction and the hydrogen pressure–assisted solvothermal process have been developed recently for the preparation of isolated ultrafine nanoparticles of MgH_2 and $LiBH_4$, respectively. Compared to their bulk counterparts, the nanostructured light metal hydrides feature simultaneously destabilized thermodynamics and reduced kinetic barriers. The 4–5 nm sized MgH_2 nanoparticles without supports delivered reversible storage of 6.7 wt.% at 30 ºC, representing a significant breakthrough in materials–based solid hydrogen storage. These findings help to develop effective methods to tailor the thermodynamic and kinetics in light metal hydrides, and provide guidance over further exploration of advanced synthesis strategies to improve the hydrogen storage performance, ultimately benefiting the development of a carbon–neutral society.

Data availability

Data sharing is not applicable to this article as no new data were created or analyzed in this study.

Declaration of competing interest

The authors declare that they have no known competing financial interests or personal relationships that could have appeared to influence the work reported in this paper.

CRediT authorship contribution statement

Yongfeng Liu: Conceptualization, Funding acquisition, Investigation, Project administration, Writing – original draft, Writing – review & editing; **Wenxuan Zhang**: Investigation, Data curation, Writing – original draft; **Xin Zhang**: Investigation, Data curation, Writing – review & editing; **Limei Yang**: Writing - review & editing; **Zhenguo Huang**: Formal analysis, Writing - review & editing; **Fang Fang**: Conceptualization, Formal analysis, Writing - review & editing; **Wenping Sun**: Writing - review & editing; **Mingxia Gao**: Formal analysis; **Hongge Pan**: Conceptualization, Supervision, Writing – review & editing.

Acknowledgements

We gratefully acknowledge the financial support received from the National Outstanding Youth Foundation of China (52125104), the Natural Science Foundation of Zhejiang Province (LD21E010002), the National Natural Science Foundation of China (52001277), the Fundamental Research Funds for the Central Universities (2021FZZX001–09), and the National Youth Top–Notch Talent Support Program.

References

[1]Schlapbach L, Züttel A. Hydrogen–storage materials for mobile applications. Nature 2001;414(6861):353–8.

[2]He T, Pachfule P, Wu H, Xu Q, Chen P. Hydrogen carriers. Nat Rev Mater 2016;1(12):16059.

[3]Gupta A, Baron GV, Perreault P, Lenaerts S, Ciocarlan, R–G, Cool P, Mileo PGM,

Rogge S, Van Speybroeck V, Watson G, Van Der Voort P, Houlleberghs M, Breynaert E, Martens J, Denayer JFM. Hydrogen Clathrates: Next Generation Hydrogen Storage Materials. Energy Storage Mater 2021;41:69–107.

[4]Ramprakash B, Lindblad P, Eaton–Rye JJ, Incharoensakdi A. Current strategies and future perspectives in biological hydrogen production: A review. Renew Sus Energy Rev 2022;169:112939

[5]Zheng J, Wang C–G, Zhou H, Ye E, Xu J, Li Z, Loh XJ. Current Research Trends and Perspectives on Solid–State Nanomaterials in Hydrogen Storage. Research 2021;2021:3750689–727.

[6]Lai Q, Wang T, Sun Y. Aguey–Zinsou K–F. Rational Design of Nanosized Light Elements for Hydrogen Storage: Classes, Synthesis, Characterization, and Properties. Adv Mater Technol 2018;3(9):1700298.

[7]Zhang X, Liu Y, Zhang X, Hu J, Gao M, Pan H. Empowering hydrogen storage performance of MgH_2 by nanoengineering and nanocatalysis. Mater Today Nano 2020;9:100064–81.

[8]Farias CB, Barreiros RC, da Silva MF, Casazza AA, Converti A, Sarubbo LA. Use of Hydrogen as Fuel: A Trend of the 21st Century. Energies 2022;15(1):311–30.

[9]Felderhoff M, Weidenthaler C, von Helmolt R, Eberle U. Hydrogen storage: the remaining scientific and technological challenges. Phys Chem Chem Phys 2007;9(21):2643–53.

[10] Yang J, Sudik A, Wolverton C, Siegel D J. High capacity hydrogen storage materials: attributes for automotive applications and techniques for materials discovery. Chem Soc Rev 2010;39(2):656–75.

[11] Rivard E, Trudeau M, Zaghib K. Hydrogen Storage for Mobility: A Review. Materials 2019;12(12):1973–94.

[12] Sreedhar I, Kamani KM, Kamani BM, Reddy BM, Venugopal A. A Bird's Eye view on process and engineering aspects of hydrogen storage. Renew Sus Energy Rev 2018;91:838–60.

[13] Hassan IA, Ramadan HS, Saleh MA, Hissel D. Hydrogen storage technologies for stationary and mobile applications: Review, analysis and perspectives. Renew Sus Energy Rev 2021;149:111311.

[14] Tarasov BP, Arbuzov AA, Volodin AA, Fursikov PV, Mozhzhuhin SA, Lototskyy MV, Yartys VA. Metal hydride – Graphene composites for hydrogen based energy storage. J Alloys Compd 2022;896:162881.

[15] Van den Berg AWC, Areán CO. Materials for hydrogen storage: current research trends and perspectives. Chem Commun 2008;(6):668–81.

[16] Aguey–Zinsou K–F, Ares–Fernández J–R. Hydrogen in magnesium: new perspectives toward functional stores. Energy Environ Sci 2010;3(5):526–43.

[17] United States Department of Energy. Department of Energy Technical Targets for Onboard Hydrogen Storage for Light–Duty Vehicles, https://www.energy.gov/eere/fuelcells/doe–technical–targets–onboard–hydrogen–storage–light–duty–vehicles; 2016.

[18] Sakintuna B, Lamari–Darkrim F, Hirscher M. Metal hydride materials for solid hydrogen storage: A review. Int J Hydrogen Energy 2007;32(9):1121–40.

[19] Kumar S, Jain A, Ichikawa T, Kojima Y, Dey GK. Development of vanadium based hydrogen storage material: A review. Renew Sus Energy Rev 2017;72:791–800.

[20] Zhang W, Zhang X, Huang Z, Li H–W, Gao M, Pan H, Liu Y. Recent Development of Lithium Borohydride–Based Materials for Hydrogen Storage. Adv Energy and Sustainability Res 2021;2(10):2100073–94.

[21] He T, Cao H, Chen P. Complex Hydrides for Energy Storage, Conversion, and Utilization. Adv Mater 2019;31(50):1902757.

[22] Chandra D, Reilly JJ, Chellappa R. Metal hydrides for vehicular applications: The state of the art. JOM 2006;58(2):26–32.

[23] Liu Y, Ren Z, Zhang X, Jian N, Yang Y, Gao M, Pan H. Development of Catalyst–Enhanced Sodium Alanate as an Advanced Hydrogen–Storage Material for Mobile Applications. Energy Technol 2018;6(3):487–500.

[24] Ouyang L, Chen K, Jiang J, Yang X–S, Zhu M. Hydrogen storage in light–metal based systems: A review. Int J Hydrogen Energy 2020;829:154597.

[25] Mao J, Huang Z, Liu HK, Guo Z, Banerjee A, Chakraborty S, Ahuja R, Aguey–Zinsou K–F. Hydrogen Storage Materials for Mobile and Stationary Applications: Current State of the Art. ChemSusChem 2015;8(17):2789–825.

[26] Bérubé V, Radtke G, Dresselhaus M, Chen G. Size effects on the hydrogen storage properties of nanostructured metal hydrides: A review. Int J Energy Res 2007;31(6–7):637–63.

[27] Züttel A, Borgschulte A, Orimo S–I. Tetrahydroborates as new hydrogen storage materials. Scr Mater 2007;56(10):823–8.

[28] Orimo S–I, Nakamori Y, Kitahara G, Miwa K, Ohba N, Towata S, Züttel A. Dehydriding and rehydriding reactions of $LiBH_4$. J Alloys Compd 2005;404–406:427–30.

[29] Sandrock G. A panoramic overview of hydrogen storage alloys from a gas reaction point of view. J Alloys Compd 1999;293–295:877–88.

[30] Züttel A. Materials for hydrogen storage. Materials Today 2003;6(9):24–33.

[31] de Jongh PE, Adelhelm P. Nanosizing and Nanoconfinement: New Strategies Towards Meeting Hydrogen Storage Goals. ChemSusChem 2010;3(12):1332–48.

[32] Schneemann A, White JL, Kang S, Jeong S, Wan LF, Cho ES, Heo TW, Prendergast D, Urban JJ, Wood BC, Allendorf MD, Stavila V. Nanostructured Metal Hydrides for Hydrogen Storage. Chem Rev 2018;118(22):10775–839.

[33] Yu X, Tang Z, Sun D, Ouyang L, Zhu M. Recent advances and remaining challenges of nanostructured materials for hydrogen storage applications. Prog Mater Sci 2017;88:1–48.

[34] Ares J–R, Nevshupa R, Muñoz–Cortés E, Sánchez C, Leardini F, Ferrer I–J, Minh Huy Tran V, Aguey–Zinsou F, Fernández J–F. Unconventional Approaches to Hydrogen Sorption Reactions: Non–Thermal and Non–Straightforward Thermally Driven Methods. ChemPhysChem 2019;20(10):1248–60.

[35] Balaya P. Size effects and nanostructured materials for energy applications. Energy Environ Sci 2008;1(6):645–54.

[36] Crivello JC, Dam B, Denys RV, Dornheim M, Grant DM, Huot J, Jensen TR, de Jongh P, Latroche M, Milanese C, Milčius D, Walker GS, Webb CJ, Zlotea C, Yartys VA. Review of magnesium hydride–based materials: development and optimisation. Appl Phys A 2016;122(2):97.

[37] Shterenberg I, Salama M, Gofer Y, Levi E, Aurbach D. The challenge of developing rechargeable magnesium batteries. MRS Bull 2014;39(5):453–60.

[38] Noritake T, Towata S, Aoki M, Seno Y, Hirose Y, Nishibori E, Takata M, Sakata, M. Charge density measurement in MgH_2 by synchrotron X–ray diffraction. J Alloys Compd 2003;356–357:84–6.

[39] Fichtner M. Nanoconfinement effects in energy storage materials. Phys Chem Chem Phys 2011;13(48):21186–95.

[40] Cheung S, Deng WQ, van Duin ACT, Goddard WA. $ReaxFF_{MgH}$ Reactive Force Field for Magnesium Hydride Systems. J Phys Chem A 2005;109(5):851–9.

[41] Peng B, Li LL, Ji WQ, Cheng FY, Chen J. A quantum chemical study on magnesium(Mg)/magnesium–hydrogen(Mg–H) nanowires, J Alloys Compd 2009;484(1–2):308–13.

[42] Wu XX, Zhang RQ, Yang JL. A first–principles study of the thermodynamic and electronic properties of Mg and MgH_2 nanowires. Phys Chem Chem Phys 2016;18:19412–9.

[43] Mounkachi O, Akrouchi A, Tiouitchi G, Lakhal M, Salmani E, Benyoussef A, Kara A, El Kenz A, Ez–Zahraouy H, El Moutaouakil A. Stability, Electronic Structure and Thermodynamic Properties of Nanostructured MgH_2 Thin Films. Energies 2021;14(22):7737.

[44] Wagemans RW, van Lenthe JH, de Jongh PE, van Dillen AJ, de Jong KP. Hydrogen storage in magnesium clusters: quantum chemical study. J Am Chem Soc 2005;127(47):16675–80.

[45] Banerjee P, Chandrakumar KRS, Das GP. Dehydrogenation characteristics of Mg_nH_{2n} (n = 1–32) nanoclusters: A first–principles DFT study. AIP Conf Proc 2015;1665:050065.

[46] Iyakutti K, Surya VJ, Lavanya R, Vasu V, Rajeswarapalanichamy R, Kawazoe Y. Effects of nanostructures on the hydrogen storage properties of MgH_2–A first principles study. Comput Condens Matter 2022;30:e00643.

[47] Vajeeston P, Sartori S, Ravindran P, Knudsen KD, Hauback B, Fjellvåg H. MgH_2 in Carbon Scaffolds: A Combined Experimental and Theoretical Investigation. J Phys Chem C 2012;116(40):21139−47.

[48] Pedersen AS, Kjøller J, Larsen B, Vigeholm B. Magnesium for hydrogen storage. Int J Hydrogen Energy 1983;8(3):205–11.

[49] Huot J, Liang G, Boily S, Van Neste A, Schulz R. Structural study and hydrogen

sorption kinetics of ball–milled magnesium hydride. J Alloys Compd 1999;293–295:495–500.

[50] Zaluska A, Zaluski L, Ström–Olsen JO. Nanocrystalline magnesium for hydrogen storage. J Alloys Compd 1999;288(1):217–25.

[51] Schulz R, Huot J, Liang G, Boily S, Lalande G, Denis MC, Dodelet JP. Recent developments in the applications of nanocrystalline materials to hydrogen technologies. Mater Sci Eng A 1999;267(2):240–5.

[52] Suryanarayana C. Mechanical Alloying: A Novel Technique to Synthesize Adv Mater Res 2019;2019:4219812.

[53] Huot J, Ravnsbæk DB, Zhang J, Cuevas F, Latroche M, Jensen TR. Mechanochemical synthesis of hydrogen storage materials. Prog Mater Sci 2013;58(1):30–75.

[54] Paskevicius M, Sheppard DA, Buckley CE. Thermodynamic Changes in Mechanochemically Synthesized Magnesium Hydride Nanoparticles. J Am Chem Soc 2010;132(14):5077–83.

[55] Zhang Q, Huang Y, Xu L, Zang L, Guo H, Jiao L, Yuan H, Wang Y. Highly Dispersed MgH_2 Nanoparticle–Graphene Nanosheet Composites for Hydrogen Storage. ACS Appl Nano Mater 2019;2(6):3828–35.

[56] Zhang X, Liu Y, Ren Z, Zhang X, Hu J, Huang Z, Lu Y, Gao M, Pan H. Realizing 6.7 wt% reversible storage of hydrogen at ambient temperature with non-confined ultrafine magnesium hydrides. Energy Environ Sci 2021;14(4):2302–13.

[57] Wiberg E, Bauer R. Der Magnesiumwasserstoff MgH_2. Chem Ber 1952;85(6):593–605.

[58] Becker WE, Ashby EC. Hydrogenolysis of the Grignard Reagent. J Org Chem 1964;29(4):954–5.

[59] Setijadi EJ; Boyer C, Aguey–Zinsou K–F, Remarkable hydrogen storage properties for nanocrystalline MgH_2 synthesised by the hydrogenolysis of Grignard reagents. Phys Chem Chem Phys 2012;14(32):11386-97.

[60] Viyannalage L, Lee V, Dennis RV, Kapoor D, Haines CD, Banerjee S. From Grignard's reagents to well-defined Mg nanostructures: distinctive electrochemical and solution reduction routes. Chem Commun 2012;48(42):5169–71.

[61] Rambhujun N, Aguey–Zinsou K–F. Halide–free Grignard reagents for the synthesis of superior MgH_2 nanostructures. Int J Hydrogen Energy 2021;46(56):28675–85.

[62] Norberg NS, Arthur TS, Fredrick SJ, Prieto AL. Size–dependent hydrogen storage properties of Mg nanocrystals prepared from solution. J Am Chem Soc 2011;133(28):10679–81.

[63] Liu W, Aguey–Zinsou K–F. Size effects and hydrogen storage properties of Mg nanoparticles synthesised by an electroless reduction method. J Mater Chem A 2014;2(25):9718–26.

[64] Sun Y, Aguey–Zinsou K–F. Synthesis of Magnesium Nanofibers by Electroless Reduction and their Hydrogen Interaction Properties. Part Part Syst Charact 2017;34(4):1600276.

[65] Li W, Li C, Ma H, Chen J. Magnesium Nanowires: Enhanced Kinetics for Hydrogen Absorption and Desorption. J Am Chem Soc 2007;129(21):6710–1.

[66] Zhu C, Hayashi H, Saita I, Akiyama T. Direct synthesis of MgH_2 nanofibers at different hydrogen pressures. Int J Hydrogen Energy 2009;34(17):7283–90.

[67] Zhu C, Hosokai S, Matsumoto I, Akiyama T. Shape–Controlled Growth of MgH_2/Mg Nano/Microstructures Via Hydriding Chemical Vapor Deposition. Cryst Growth Des 2010;10(12):5123–8.

[68] Zahiri B, Amirkhiz BS, Mitlin D. Hydrogen storage cycling of MgH_2 thin film nanocomposites catalyzed by bimetallic Cr Ti. Appl Phys Lett 2010;97(8):083106.

[69] Lyu J, Lider AM, Kudiiarov VNJCPB. An overview of progress in Mg-based hydrogen storage films. Chin Phys B 2019;28(9):098801.

[70] Barawi M, Granero C, Díaz-Chao P, Manzano CV, Martin–Gonzalez M, Jimenez-Rey D, Ferrer IJ, Ares JR, Fernández JF, Sánchez C. Thermal decomposition of non–catalysed MgH_2 films. Int J Hydrogen Energy 2014;39(18):9865-70.

[71] Léon A, Knystautas EJ, Huot J, Schulz R. Hydrogenation characteristics of air–exposed magnesium films. J Alloys Compd 2002;345(1):158–66.

[72] Léon A, Knystautas EJ, Huot J, Schulz R. Influence of the evaporation rate and the evaporation mode on the hydrogen sorption kinetics of air–exposed magnesium films. Thin Solid Films 2006;496(2):683–7.

[73] Shimizu R, Kakinokizono T, Gu I, Hitosugi T. Epitaxial Growth of Single–Phase Magnesium Dihydride Thin Films. Inorg Chem 2019;58(22):15354–8.

[74] Krozer A, Kasemo B. Hydrogen uptake by Pd–coated Mg: absorption–decomposition isotherms and uptake kinetics. J Less–Common Met 1990;160(2):323–42.

[75] Higuchi K, Kajioka H, Toiyama K, Fujii H, Orimo S–I, Kikuchi Y. In situ study of hydriding–dehydriding properties in some Pd/Mg thin films with different degree of Mg crystallization. J Alloys Compd 1999;293–295:484–9.

[76] Singh S, Eijt S WH, Zandbergen MW, Legerstee WJ, Svetchnikov VL. Nanoscale structure and the hydrogenation of Pd–capped magnesium thin films prepared by plasma sputter and pulsed laser deposition. J Alloys Compd 2007;441(1):344–51.

[77] Higuchi K, Yamamoto K, Kajioka H, Toiyama K, Honda M, Orimo S–I, Fujii H. Remarkable hydrogen storage properties in three-layered Pd/Mg/Pd thin films. J

Alloys Compd 2002;330-332:526-30.

[78] Qu J, Sun B, Zheng J, Yang R, Wang Y, Li X. Hydrogen desorption properties of Mg thin films at room temperature. J Power Sources 2010;195(4):1190-4.

[79] Domènech–Ferrer R, Gurusamy Sridharan M, Garcia G, Pi F, Rodríguez–Viejo J. Hydrogenation properties of pure magnesium and magnesium–aluminium thin films. J Power Sources 2007;169(1):117–22.

[80] Jain P, Jain A, Vyas D, Verma R, Khan SA, Jain IP. The effects of Ni and Mg_2Ni interlayer on hydrogenation properties of Pd sandwiched Mg films. J Alloys Compd 2011;509(5):2105–10.

[81] Jung H, Cho S, Lee W. A catalytic effect on hydrogen absorption kinetics in Pd/Ti/Mg/Ti multilayer thin films. J Alloys Compd 2015;635:203–6.

[82] Ham B, Junkaew A, Arróyave R, Park J, Zhou HC, Foley D, Rios S, Wang H, Zhang X. Size and stress dependent hydrogen desorption in metastable Mg hydride films. Int J Hydrogen Energy 2014;39(6):2597–607.

[83] Reddy GLN, Kumar S. Hydrogen storage studies in Pd/Ti/Mg films. Int J Hydrogen Energy 2018;43(5):2840–9.

[84] Fry CMP, Grant DM, Walker GS. Catalysis and evolution on cycling of nano–structured magnesium multilayer thin films. Int J Hydrogen Energy 2014;39(2):1173–84.

[85] Zhu M, Gao Y, Che XZ, Yang YQ, Chung CY. Hydriding kinetics of nano–phase composite hydrogen storage alloys prepared by mechanical alloying of Mg and $MmNi_{5-x}(CoAlMn)_x$. J Alloys Compd 2002;330–332:708–13.

[86] Wang H, Ouyang LZ, Peng CH, Zeng MQ, Chung CY, Zhu M. MmM_5/Mg multi-layer hydrogen storage thin films prepared by dc magnetron sputtering. J Alloys Compd 2004;370(1):L4–6.

[87] Wang H, Ouyang LZ, Zeng MQ, Zhu M. Hydrogen sorption properties of Mg/Mm–Ni multi–layer film prepared by thermal evaporation. J Alloys Compd 2004;375(1):313–7.

[88] Ouyang LZ, Wang H, Zhu M, Zou J, Chung CY. Microstructure of MmM_5/Mg multi–layer films prepared by magnetron sputtering. J Alloys Compd 2005;404–406:485–9.

[89] Jangid MK, Singh M. Hydrogenation and annealing effect on electrical properties of nanostructured Mg/Mn bilayer thin films. Int J Hydrogen Energy 2012;37(4):3786–91.

[90] Ostenfeld CW, Johansson M, Chorkendorff I. Hydrogenation properties of catalyzed and non–catalyzed magnesium films. Surf Sci 2007;601(8):1862–9.

[91] Akyıldız H, Özenbaş M, Öztürk T. Hydrogen absorption in magnesium based crystalline thin films. Int J Hydrogen Energy 2006;31(10):1379–83.

[92] Shen C, Aguey–Zinsou K–F. Electrochemical deposited Mg–PPy multilayered film to store hydrogen. Int J Hydrogen Energy 2018;43(49):22385–90.

[93] Hashimoto T, Notomi M. Hydrogen storage properties of Mg–based multilayer films. Mech Eng J 2016;3(4):16–00228.

[94] Wang H, Zhang SF, Liu JW, Ouyang, LZ, Zhu M. Enhanced dehydrogenation of nanoscale MgH_2 confined by ordered mesoporous silica. Mater Chem Phys 2012;136(1):146–50.

[95] Lim DW, Yoon JW, Ryu KY, Suh MP. Magnesium nanocrystals embedded in a metal-organic framework: hybrid hydrogen storage with synergistic effect on physi–and chemisorption. Angew Chem Int Ed 2012;51(39):9814–7.

[96] Nielsen TK, Manickam K, Hirscher M, Besenbacher F, Jensen TR. Confinement of MgH_2 Nanoclusters within Nanoporous Aerogel Scaffold Materials. ACS Nano

2009;3(11):3521–8.

[97] Au YS, Obbink MK, Srinivasan S, Magusin PCMM, de Jong KP, de Jongh PE. The Size Dependence of Hydrogen Mobility and Sorption Kinetics for Carbon–Supported MgH_2 Particles. Adv Funct Mater 2014;24(23):3604–11.

[98] Gross AF, Ahn CC, Van Atta SL, Liu P, Vajo JJ. Fabrication and hydrogen sorption behaviour of nanoparticulate MgH_2 incorporated in a porous carbon host. Nanotechnology 2009;20(20):204005.

[99] Zhang S, Gross AF, Van Atta SL, Lopez M, Liu P, Ahn CC, Vajo JJ, Jensen CM. The synthesis and hydrogen storage properties of a MgH_2 incorporated carbon aerogel scaffold. Nanotechnology 2009;20(20):204027.

[100] Paskevicius M, Tian H–Y, Sheppard DA, Webb CJ, Pitt MP, Gray EM, Kirby NM, Buckley CE. Magnesium Hydride Formation within Carbon Aerogel. J Phys Chem C 2011;115(5):1757–66.

[101] de Jongh PE, Wagemans RWP, Eggenhuisen TM, Dauvillier BS, Radstake PB, Meeldijk JD, Geus JW, de Jong KP. The Preparation of Carbon–Supported Magnesium Nanoparticles using Melt Infiltration. Chem Mater 2007;19(24):6052–7.

[102] Zhao–Karger Z, Hu J, Roth A, Wang D, Kübel C, Lohstroh W, Fichtner M. Altered thermodynamic and kinetic properties of MgH_2 infiltrated in microporous scaffold. Chem Commun 2010;46(44):8353–5.

[103] Jia Y, Sun C, Cheng L, Abdul Wahab M, Cui J, Zou J, Zhu M, Yao X. Destabilization of Mg–H bonding through nano–interfacial confinement by unsaturated carbon for hydrogen desorption from MgH_2. Phys Chem Chem Phys 2013;15(16):5814–20.

[104] Jia Y, Yao X. Carbon scaffold modified by metal (Ni) or non–metal (N) to enhance

hydrogen storage of MgH_2 through nanoconfinement. Int J Hydrogen Energy 2017;42(36):22933–41.

[105] Ma Z, Panda S, Zhang Q, Sun F, Khan D, Ding W, Zou J. Improving hydrogen sorption performances of MgH_2 through nanoconfinement in a mesoporous CoS nano–boxes scaffold. Chem Eng J 2021;406:126790.

[106] Xia G, Tan Y, Chen X, Sun D, Guo Z, Liu H, Ouyang L, Zhu M, Yu X. Monodisperse Magnesium Hydride Nanoparticles Uniformly Self–Assembled on Graphene. Adv Mater 2015;27(39):5981–8.

[107] Cho ES, Ruminski AM, Aloni S, Liu Y–S, Guo J, Urban JJ. Graphene oxide/metal nanocrystal multilaminates as the atomic limit for safe and selective hydrogen storage. Nat Commun 2016;7(1):10804.

[108] Jeon K–J, Moon HR, Ruminski AM, Jiang B, Kisielowski C, Bardhan R, Urban JJ. Air–stable magnesium nanocomposites provide rapid and high–capacity hydrogen storage without using heavy–metal catalysts. Nat Mater 2011;10(4):286–90.

[109] Makridis SS, Gkanas EI, Panagakos G, Kikkinides ES, Stubos AK, Wagener P, Barcikowski S. Polymer-stable magnesium nanocomposites prepared by laser ablation for efficient hydrogen storage. Int J Hydrogen Energy 2013;38(26):11530–5.

[110] Liu M, Zhao S, Xiao X, Chen M, Sun C, Yao Z, Hu Z, Chen L. Novel 1D carbon nanotubes uniformly wrapped nanoscale MgH_2 for efficient hydrogen storage cycling performances with extreme high gravimetric and volumetric capacities. Nano Energy 2019;61:540–9.

[111] Zhu W, Ren L, Lu C, Xu H, Sun F, Ma Z, Zou J. Nanoconfined and in Situ Catalyzed MgH_2 Self–Assembled on 3D Ti_3C_2 MXene Folded Nanosheets with

Enhanced Hydrogen Sorption Performances. ACS Nano 2021;15(11):18494–504.

[112] Bogdanović B, Schwickardi M. Ti–doped alkali metal aluminium hydrides as potential novel reversible hydrogen storage materials. J Alloys Compd 1997;253–254:1–9.

[113] Rafi–ud d, Xuanhui Q, Ping L, Zhang L, Qi W, Iqbal MZ, Rafique MY, Farooq MH, Islam–ud d. Superior Catalytic Effects of Nb_2O_5, TiO_2, and Cr_2O_3 Nanoparticles in Improving the Hydrogen Sorption Properties of $NaAlH_4$. J Phys Chem C 2012;116(22):11924–38.

[114] Meenakshi, Agnihotri D, Jeet K, Sharma H. Improvement in dehydrogenation of MXH_4 where M=Na, Li and X=Al, B confined in CNTs: a DFT investigation. Mater Res Express 2016;3:115013.

[115] Mueller T, Ceder G. Effect of Particle Size on Hydrogen Release from Sodium Alanate Nanoparticles. ACS Nano 2010;4(10):5647–56.

[116] Huang YH, Li P, Wan Q, Zhang J, Li Y, Li RW, Dong XP, Qu XH. Improved dehydrogenation performance of $NaAlH_4$ using $NiFe_2O_4$ nanoparticles. J Alloys Compd. 2017;709:850–6.

[117] Singh S, Eijt SWH, Huot J, Kockelmann WA, Wagemaker M, Mulder FM. The $TiCl_3$ catalyst in $NaAlH_4$ for hydrogen storage induces grain refinement and impacts on hydrogen vacancy formation. Acta Mater 2007;55(16):5549–57.

[118] Zaluska A, Zaluski L, Ström–Olsen JO. Sodium alanates for reversible hydrogen storage. J Alloys Compd 2000;298(1):125–34.

[119] Fichtner M, Canton P, Kircher O, Léon A. Nanocrystalline alanates–Phase transformations, and catalysts. J Alloys Compd 2005;404–406:732–7.

[120] Baldé CP, Hereijgers BP, Bitter JH, de Jong KP. Facilitated hydrogen storage in $NaAlH_4$ supported on carbon nanofibers. Angew Chem Int Ed 2006;45(21):3501–3.

[121] Baldé CP, Hereijgers BP, Bitter JH, de Jong KP. Sodium alanate nanoparticles–linking size to hydrogen storage properties. J Am Chem Soc 2008;130(21):6761–5.

[122] Baldé CP, Leynaud O, Barnes P, Peláez-Jiménez E, de Jong KP, Bitter JH. Towards a structure–performance relationship for hydrogen storage in Ti–doped $NaAlH_4$ nanoparticles. Chem Commun 2011;47(7):2143–5.

[123] Li Y, Fang F, Fu H, Qiu J, Song Y, Li Y, Sun D, Zhang Q, Ouyang L, Zhu M. Carbon nanomaterial–assisted morphological tuning for thermodynamic and kinetic destabilization in sodium alanates. J Mater Chem A 2013;1(17):5238–46.

[124] Ko Y, Lombardo L, Li M, Oveisi E, Yang H, Züttel A. Interfacial Effect between Aluminum–Based Complex Hydrides and Nickel–Containing Porous Carbon Sheets. ACS Appl Energy Mater 2020;3(10):9685–95.

[125] Zheng S, Fang F, Zhou G, Chen G, Ouyang L, Zhu M, Sun D. Hydrogen Storage Properties of Space–Confined $NaAlH_4$ Nanoparticles in Ordered Mesoporous Silica. Chem Mater 2008;20(12):3954–8.

[126] Stephens RD, Gross AF, Van Atta SL, Vajo JJ, Pinkerton FE. The kinetic enhancement of hydrogen cycling in $NaAlH_4$ by melt infusion into nanoporous carbon aerogel. Nanotechnology 2009;20(20):204018.

[127] Nielsen TK, Javadian P, Polanski M, Besenbacher F, Bystrzycki J, Jensen TR. Nanoconfined $NaAlH_4$: Determination of Distinct Prolific Effects from Pore Size, Crystallite Size, and Surface Interactions. J Phys Chem C 2012;116(39):21046–51.

[128] Nielsen TK, Polanski M, Zasada D, Javadian P, Besenbacher F, Bystrzycki J, Skibsted J, Jensen TR. Improved Hydrogen Storage Kinetics of Nanoconfined $NaAlH_4$ Catalyzed with $TiCl_3$ Nanoparticles. ACS Nano 2011;5(5):4056–64.

[129] Li Y, Zhou G, Fang F, Yu X, Zhang Q, Ouyang L, Zhu M, Sun D. De–/re–hydrogenation features of $NaAlH_4$ confined exclusively in nanopores. Acta Mater

2011;59(4):1829–38.

[130] Jeong U, Kim H, Ramesh S, Dogan NA, Wongwilawan S, Kang S, Park J, Cho ES, Yavuz CT. Rapid Access to Ordered Mesoporous Carbons for Chemical Hydrogen Storage. Angew Chem Int Ed 2021;60(41):22478–86.

[131] Adelhelm P, Gao J, Verkuijlen MHW, Rongeat C, Herrich M, van Bentum PJM, Gutfleisch O, Kentgens APM, de Jong KP, de Jongh PE. Comprehensive Study of Melt Infiltration for the Synthesis of $NaAlH_4$/C Nanocomposites. Chem Mater 2010;22(7):2233–8.

[132] Fan X, Xiao X, Shao J, Zhang L, Li S, Ge H, Wang Q, Chen L. Size effect on hydrogen storage properties of $NaAlH_4$ confined in uniform porous carbons. Nano Energy 2013;2(5):995–1003.

[133] Nielsen TK, Javadian P, Polanski M, Besenbacher F, Bystrzycki J, Skibsted J, Jensen TR. Nanoconfined $NaAlH_4$: prolific effects from increased surface area and pore volume. Nanoscale 2014;6(1):599–607.

[134] Palm R, Kurig H, Aruväli J, Lust E. $NaAlH_4$/microporous carbon composite materials for reversible hydrogen storage. Microporous Mesoporous Mater 2018;264:8–12.

[135] Carr CL, Jayawardana W, Zou H, White JL, El Gabaly F, Conradi MS, Stavila V, Allendorf MD, Majzoub EH. Anomalous H_2 Desorption Rate of $NaAlH_4$ Confined in Nitrogen-Doped Nanoporous Carbon Frameworks. Chem Mater 2018;30(9):2930–8.

[136] Lohstroh W, Roth A, Hahn H, Fichtner M. Thermodynamic Effects in Nanoscale $NaAlH_4$. ChemPhysChem 2010;11(4):789–92.

[137] Christian M, Aguey–Zinsou K–F. Destabilisation of complex hydrides through size effects. Nanoscale 2010;2(12):2587–90.

[138] Huang Y, Xia G, Zhang J, Guo Z, Yu X. Graphene–tailored molecular bonds for advanced hydrogen and lithium storage performance. Energy Storage Mater 2019;17:178–85.

[139] Huang Y, Shao H, Zhang Q, Zang L, Guo H, Liu Y, Jiao L, Yuan H, Wang Y. Layer–by–layer uniformly confined Graphene–$NaAlH_4$ composites and hydrogen storage performance. Int J Hydrogen Energy 2020;45(52):28116–22.

[140] Bhakta RK, Maharrey S, Stavila V, Highley A, Alam T, Majzoub E, Allendorf M. Thermodynamics and kinetics of $NaAlH_4$ nanocluster decomposition. Phys Chem Chem Phys 2012;14(22):8160–9.

[141] Gao Q, Xia G, Yu X. Confined $NaAlH_4$ nanoparticles inside CeO_2 hollow nanotubes towards enhanced hydrogen storage. Nanoscale 2017;9(38);14612–9.

[142] Li Z, Yu JZ, Zhang Y, Liu DM, Wang CY, Si TZ, Li YT, Zhang QA. Coupling of nanoconfinement with metallic catalysis in supported $NaAlH_4$ for low–temperature hydrogen storage. J Power Sources 2021;491:229611.

[143] Bhakta RK, Herberg JL, Jacobs B, Highley A, Behrens R, Ockwig NW, Greathouse JA, Allendorf MD. Metal−Organic Frameworks As Templates for Nanoscale $NaAlH_4$. J Am Chem Soc 2009;131(37):13198–9.

[144] Stavila V, Bhakta RK, Alam TM, Majzoub EH, Allendorf MD. Reversible Hydrogen Storage by $NaAlH_4$ Confined within a Titanium–Functionalized MOF-74(Mg) Nanoreactor. ACS Nano 2012;6(11):9807–17.

[145] Wahab MA, Beltramini JN. Catalytic nanoconfinement effect of in-situ synthesized Ni–containing mesoporous carbon scaffold (Ni–MCS) on the hydrogen storage properties of $LiAlH_4$. Int J Hydrogen Energy 2014;39(32):18280–18290.

[146] Zhao Y, Han M, Wang H, Chen C, Chen J. $LiAlH_4$ supported on TiO_2/hierarchically porous carbon nanocomposites with enhanced hydrogen storage

properties. Inorg Chem Front 2016;3(12):1536–42.

[147] Wang L, Rawal A, Quadir MZ, Aguey–Zinsou K–F. Nanoconfined lithium aluminium hydride ($LiAlH_4$) and hydrogen reversibility. Int J Hydrogen Energy 2017;42(20):14144–53.

[148] Cho Y, Li S, Snider JL, Marple MAT, Strange NA, Sugar JD, El Gabaly F, Schneemann A, Kang S, Kang MH, Park H, Park J, Wan LF, Mason HE, Allendorf MD, Wood BC, Cho ES, Stavila V. Reversing the Irreversible: Thermodynamic Stabilization of $LiAlH_4$ Nanoconfined Within a Nitrogen–Doped Carbon Host. ACS Nano 2021;15(6):10163–74.

[149] Varin RA, Chiu C, Czujko T, Wronski Z. Mechano–chemical activation synthesis (MCAS) of nanocrystalline magnesium alanate hydride [$Mg(AlH_4)_2$] and its hydrogen desorption properties. J Alloys Compd 2007;439(1):302–11.

[150] Xiao X, Qin T, Jiang Y, Jiang F, Li M, Fan X, Li S, Ge H, Wang Q, Chen L. Significantly enhanced hydrogen desorption properties of $Mg(AlH_4)_2$ nanoparticles synthesized using solvent free strategy. Prog Nat Sci Mater Int 2017;27(1):112–20.

[151] Morisaku N, Komiya K, Li YZ, Yukawa H, Morinaga M, Ikeda K, Orimo S-I. Synthesis and Decomposition of Pure $Ca(AlH_4)_2$. Adv Mater Res 2007;26–28:869–72.

[152] Pang Y, Liu Y, Gao M, Ouyang L, Liu J, Wang H, Zhu M, Pan H. A mechanical–force–driven physical vapour deposition approach to fabricating complex hydride nanostructures. Nat Commun 2014;5(1):3519.

[153] Züttel A, Rentsch S, Fischer P, Wenger P, Sudan P, Mauron P, Emmenegger C. Hydrogen storage properties of $LiBH_4$. J Alloys Compd 2003;356–357:515–20.

[154] Li,H–W, Yan Y, Orimo S–I, Züttel A, Jensen CM. Recent Progress in Metal Borohydrides for Hydrogen Storage. Energies 2011;4(1):185–214.

[155] CRC Handbook of Chemistry and Physics. In: Rumble JR, editors. Introduction to the 102nd Edition CRC, Taylor&Francis: E–Publishing Inc; 2021.

[156] Wellons, MS, Berseth PA, Zidan R. Novel catalytic effects of fullerene for $LiBH_4$ hydrogen uptake and release. Nanotechnology 2009;20(20):204022.

[157] Hamedoun M, Mounkachi O. Improved thermodynamic properties of doped $LiBH_4$ for hydrogen storage: First–principal calculation. Int J Hydrogen Energy 2019;44(31):16793–802.

[158] Vajeeston P, Ravindran P, Fjellvåg H. Nanostructures of $LiBH_4$: a density–functional study. Nanotechnology 2009;20:275704.

[159] Hazrati E, Brocks G, de Wijs GA. First–Principles Study of $LiBH_4$ Nanoclusters and Their Hydrogen Storage Properties. J Phys Chem C 2012;116(34):18038−47.

[160] Huang Z–Q, Chen W–C, Chuang F–C, Majzoub EH, Ozoliņš V. First–principles calculated decomposition pathways for $LiBH_4$ nanoclusters. Sci Rep 2016;6:26056.

[161] Züttel A, Wenger P, Rentsch S, Sudan P, Mauron P, Emmenegger C. $LiBH_4$ a New Hydrogen Storage Material. J Power Sources 2003;118(1–2):1–7.

[162] Mauron P, Buchter F, Friedrichs O, Remhof A, Bielmann M, Zwicky CN, Züttel A. Stability and Reversibility of $LiBH_4$. J Phys Chem B, 2008;112(3):906–10.

[163] Gross AF, Vajo JJ, Van Atta SL, Olson GL. Enhanced Hydrogen Storage Kinetics of $LiBH_4$ in Nanoporous Carbon Scaffolds. J Phys Chem C 2008;112(14):5651–7.

[164] Fang ZZ, Wang P, Rufford TE, Kang XD, Lu GQ, Cheng HM. Kinetic– and thermodynamic–based improvements of lithium borohydride incorporated into activated carbon. Acta Mater 2008;56(20):6257–63.

[165] Cahen S, Eymery JB, Janot R, Tarascon JM. Improvement of the $LiBH_4$ hydrogen desorption by inclusion into mesoporous carbons. J Power Sources 2009;189(2):902-8.

[166] Ngene P, Adelhelm P, Beale AM, de Jong KP, de Jongh PE. $LiBH_4$/SBA–15 Nanocomposites Prepared by Melt Infiltration under Hydrogen Pressure: Synthesis and Hydrogen Sorption Properties. J Phys Chem C 2010;114(13):6163-8.

[167] Sun T, Liu J, Jia Y, Wang H, Sun D, Zhu M, Yao X. Confined $LiBH_4$: Enabling fast hydrogen release at ~100 °C. Int J Hydrogen Energy 2012;37(24):18920–6.

[168] Liu X, Peaslee D, Jost CZ, Baumann TF, Majzoub EH. Systematic Pore–Size Effects of Nanoconfinement of $LiBH_4$: Elimination of Diborane Release and Tunable Behavior for Hydrogen Storage Applications. Chem Mater 2011;23(5):1331–6.

[169] Surrey A, Bonatto Minella C, Fechler N, Antonietti M, Grafe H–J, Schultz L, Rellinghaus B. Improved hydrogen storage properties of $LiBH_4$ via nanoconfinement in micro– and mesoporous aerogel–like carbon. Int J Hydrogen Energy 2016;41(12):5540–8.

[170] Vellingiri L, Annamalai K, Kandasamy R, Kombiah I. Single–walled carbon nanotubes/lithium borohydride composites for hydrogen storage: role of in situ formed $LiB(OH)_4$, Li_2CO_3 and $LiBO_2$ by oxidation and nitrogen annealing. RSC Adv 2019;9(54):31483–96.

[171] Plerdsranoy P, Kaewsuwan D, Chanlek N, Utke R. Effects of specific surface area and pore volume of activated carbon nanofibers on nanoconfinement and dehydrogenation of $LiBH_4$. Int J Hydrogen Energy 2017;42(9):6189–201.

[172] Guo L, Li Y, Ma Y, Liu Y, Peng D, Zhang L, Han S. Enhanced hydrogen storage capacity and reversibility of $LiBH_4$ encapsulated in carbon nanocages. Int J Hydrogen Energy 2017;42(4):2215–22.

[173] Lai Q, Yang Y, Aguey–Zinsou K–F. Nanoconfinement of borohydrides in hollow carbon spheres: Melt infiltration versus solvent impregnation for enhanced hydrogen

storage. Int J Hydrogen Energy 2019;44(41): 23225–38.

[174] Wang S, Gao M, Xian K, Li Z, Shen Y, Yao Z, Liu Y, Pan H. $LiBH_4$ Nanoconfined in Porous Hollow Carbon Nanospheres with High Loading, Low Dehydrogenation Temperature, Superior Kinetics, and Favorable Reversibility. ACS Appl Energy Mater 2020;3(4):3928–38.

[175] Wu R, Zhang X, Liu Y, Zhang L, Hu J, Gao M, Pan H. A Unique Double–Layered Carbon Nanobowl–Confined Lithium Borohydride for Highly Reversible Hydrogen Storage. Small 2020;16(32):2001963.

[176] Xia G, Tan Y, Chen X, Fang F, Sun D, Li X, Guo Z, Yu X. Oxygen–free Layer–by–Layer Assembly of Lithiated Composites on Graphene for Advanced Hydrogen Storage. Adv Sci 2017;4(9):1600257.

[177] Zhang X, Zhang L, Zhang W, Ren Z, Huang Z, Hu J, Gao M, Pan H, Liu Y. Nano–synergy enables highly reversible storage of 9.2 wt% hydrogen at mild conditions with lithium borohydride. Nano Energy 2021;83:105839.

[178] Sun W, Li S, Mao J, Guo Z, Liu H, Dou S, Yu X. Nanoconfinement of lithium borohydride in Cu–MOFs towards low temperature dehydrogenation. Dalton Trans 2011;40(21):5673–6.

[179] Zang L, Sun W, Liu S, Huang Y, Yuan H, Tao Z, Wang Y. Enhanced Hydrogen Storage Properties and Reversibility of $LiBH_4$ Confined in Two–Dimensional Ti_3C_2. ACS Appl Mater Interfaces 2018;10(23):19598–604.

[180] Fan Y, Chen D, Liu X, Fan G, Liu B. Improving the hydrogen storage performance of lithium borohydride by Ti_3C_2 MXene. Int J Hydrogen Energy 2019;44(55):29297–303.

[181] Guo L, Jiao L, Li L, Wang Q, Liu G, Du H, Wu Q, Du J, Yang J, Yan C, Wang Y, Yuan H. Enhanced desorption properties of $LiBH_4$ incorporated into mesoporous

TiO_2. Int J Hydrogen Energy 2013;38(1):162–8.

[182] Xian K, Nie B, Li Z, Gao M, Li Z, Shang C, Liu Y, Guo Z, Pan H. TiO_2 decorated porous carbonaceous network structures offer confinement, catalysis and thermal conductivity for effective hydrogen storage of $LiBH_4$. Chem Eng J 2021;407:127156.

[183] Wang S, Gao M, Yao Z, Liu Y, Wu M, Li Z, Liu Y, Sun W, Pan H. A nanoconfined–$LiBH_4$ system using a unique multifunctional porous scaffold of carbon wrapped ultrafine Fe_3O_4 skeleton for reversible hydrogen storage with high capacity. Chem Eng J 2022;428:131056.

[184] Xu X, Zang L, Zhao Y, Zhao Y, Wang Y, Jiao L. Hydrogen storage behavior of $LiBH_4$ improved by the confinement of hierarchical porous $ZnO/ZnCo_2O_4$ nanoparticles. J Power Sources 2017;359:134–41.

[185] Xu X, Zang L, Zhao Y, Liu Y, Wang Y, Jiao L. Enhanced dehydrogenation performance of $LiBH_4$ by confinement in porous $NiMnO_3$ microspheres. Int J Hydrogen Energy 2017;42(41):25824–30.

[186] Lai Q, Christian M, Aguey–Zinsou K–F. Nanoconfinement of borohydrides in CuS hollow nanospheres: A new strategy compared to carbon nanotubes. Int J Hydrogen Energy 2014;39(17):9339–49.

[187] Sofianos MV; Sheppard DA; Rowles MR; Humphries TD; Liu S, Buckley CE. Novel synthesis of porous Mg scaffold as a reactive containment vessel for $LiBH_4$. RSC Adv 2017;7(58):36340–50.

[188] Sofianos MV, Sheppard DA, Silvester DS, Lee J, Paskevicius M, Humphries, TD, Buckley CE. Electrochemical Synthesis of Highly Ordered Porous Al Scaffolds Melt–Infiltrated with $LiBH_4$ for Hydrogen Storage. J Electrochem Soc 2018;165(2):D37–42.

[189] Chen X, Li Z, Zhang Y, Liu D, Wang C, Li Y, Si T, Zhang Q. Enhanced Low–

Temperature Hydrogen Storage in Nanoporous Ni–Based Alloy Supported $LiBH_4$. Front Chem 2020;8:283.

[190] Gasnier A, Gennari FC. Graphene entanglement in a mesoporous resorcinol–formaldehyde matrix applied to the nanoconfinement of $LiBH_4$ for hydrogen storage. RSC Adv 2017;7(45):27905-12.

[191] Gasnier A, Luguet M, Pereira AG, Troiani H, Zampieri G, Gennari FC. Entanglement of N–doped graphene in resorcinol–formaldehyde: Effect over nanoconfined $LiBH_4$ for hydrogen storage. Carbon 2019;147:284–94.

[192] Muthu RN, Rajashabala S, Kannan R. Hydrogen storage performance of lithium borohydride decorated activated hexagonal boron nitride nanocomposite for fuel cell applications. Int J Hydrogen Energy 2017;42(23):15586–96.

[193] Zhou H, Zhang L, Gao S, Liu H, Xu L, Wang X, Yan M. Hydrogen storage properties of activated carbon confined $LiBH_4$ doped with CeF_3 as catalyst. Int J Hydrogen Energy 2017;42(36):23010–7.

[194] Li Y, Zhang Q, Fang F, Song Y, Sun D, Ouyang L, Zhu M. Facile self–assembly of light metal borohydrides with controllable nanostructures. RSC Adv 2014;4(2):983–6.

[195] Wang T, Aguey–Zinsou K–F. Controlling the Growth of $LiBH_4$ Nanoparticles for Hydrogen Storage. Energy Technol 2019;7(6):1801159.

[196] Wang T, Aguey–Zinsou K–F. Synthesis of borohydride nanoparticles at room temperature by precipitation. Int J Hydrogen Energy 2021;46(47):24286–92.

[197] Zhang X, Zhang W, Zhang L, Huang Z, Hu J, Gao M, Pan H, Liu Y. Single–pot solvothermal strategy toward support–free nanostructured $LiBH_4$ featuring 12 wt% reversible hydrogen storage at 400 °C. Chem Eng J 2022;428:132566.

[198] Nakamori Y, Miwa K, Ninomiya A, Li H, Ohba N, Towata S–I, Züttel A, Orimo

S-I. Correlation between thermodynamical stabilities of metal borohydrides and cation electronegativites: First–principles calculations and experiments. Phys Rev B 2006;74(4):045126.

[199] Soloveichik GL, Gao Y, Rijssenbeek J, Andrus M, Kniajanski S, Bowman RC, Hwang S–J, Zhao J–C. Magnesium borohydride as a hydrogen storage material: Properties and dehydrogenation pathway of unsolvated $Mg(BH_4)_2$. Int J Hydrogen Energy 2009;34(2):916–28.

[200] Chłopek K, Frommen C, Léon A, Zabara O, Fichtner M. Synthesis and properties of magnesium tetrahydroborate, $Mg(BH_4)_2$. J Mater Chem 2007;17(33):3496–503.

[201] Pitt MP, Webb CJ, Paskevicius M, Sheptyakov D, Buckley CE, Gray EM. In Situ Neutron Diffraction Study of the Deuteration of Isotopic $Mg^{11}B_2$. J Mater Chem C 2011;115(45):22669–79.

[202] Li HW, Kikuchi K, Nakamori Y, Miwa K, Towata S, Orimo S–I. Effects of ball milling and additives on dehydriding behaviors of well–crystallized $Mg(BH_4)_2$. Scr Mater 2007;57(8):679–82.

[203] Pistidda C, Garroni S, Dolci F, Bardají EG, Khandelwal A, Nolis P, Dornheim M, Gosalawit R, Jensen T, Cerenius Y, Suriñach S, Baró MD, Lohstroh W, Fichtner M. Synthesis of amorphous $Mg(BH_4)_2$ from MgB_2 and H_2 at room temperature. J Alloys Compd 2010;508(1):212–5.

[204] Wang X, Xiao X, Zheng J, Huang X, Chen M, Chen L. In–situ synthesis of amorphous $Mg(BH_4)_2$ and chloride composite modified by NbF_5 for superior reversible hydrogen storage properties. Int J Hydrogen Energy 2020;45(3):2044–53.

[205] Li H–W, Kikuchi K, Sato T, Nakamori Y, Ohba N, Aoki M, Miwa K, Towata S–I, Orimo S-I. Synthesis and Hydrogen Storage Properties of a Single–Phase Magnesium Borohydride $Mg(BH_4)_2$. Mater Trans 2008;49(10):2224–8.

[206] Bateni A, Scherpe S, Acar S, Somer M. Novel Approach for Synthesis of Magnesium Borohydride, $Mg(BH_4)_2$. Energy Procedia 2012;29:26–33.

[207] Fichtner M, Zhao–Karger Z, Hu J, Roth A, Weidler P. The kinetic properties of $Mg(BH_4)_2$ infiltrated in activated carbon. Nanotechnology 2009;20(20):204029.

[208] Ampoumogli A, Steriotis T, Trikalitis P, Giasafaki D, Bardaji EG, Fichtner M, Charalambopoulou G. Nanostructured composites of mesoporous carbons and boranates as hydrogen storage materials. J Alloys Compd 2011;509:S705–8.

[209] Wahab MA, Jia Y, Yang D, Zhao H, Yao X. Enhanced hydrogen desorption from $Mg(BH_4)_2$ by combining nanoconfinement and a Ni catalyst. J Mater Chem A 2013;1(10):3471–8.

[210] Wahab MA, Young DJ, Karim A, Fawzia S, Beltramini JN. Low–temperature hydrogen desorption from $Mg(BH_4)_2$ catalysed by ultrafine Ni nanoparticles in a mesoporous carbon matrix. Int J Hydrogen Energy 2016;41(45):20573–82.

[211] Clémençon D, Davoisne C, Chotard JN, Janot R. Enhancement of the hydrogen release of $Mg(BH_4)_2$ by concomitant effects of nano–confinement and catalysis. Int J Hydrogen Energy 2019;44(8):4253–62.

[212] Yan Y, Au YS, Rentsch D, Remhof A, de Jongh PE, Züttel A. Reversible hydrogen storage in $Mg(BH_4)_2$/carbon nanocomposites. J Mater Chem A 2013;1(37):11177–83.

[213] Han M, Zhao Q, Zhu Z, Hu Y, Tao Z, Chen J. The enhanced hydrogen storage of micro–nanostructured hybrids of $Mg(BH_4)_2$–carbon nanotubes. Nanoscale 2015;7(43):18305–11.

[214] Jiang Z, Yuan J, Han H, Wu Y. Effect of carbon nanotubes on the microstructural evolution and hydrogen storage properties of $Mg(BH_4)_2$. J Alloys Compd 2018;743:11–6.

[215] Zhang H, Xia G, Zhang J, Sun D, Guo Z, Yu X. Graphene–Tailored Thermodynamics and Kinetics to Fabricate Metal Borohydride Nanoparticles with High Purity and Enhanced Reversibility. Adv Energy Mater 2018;8(13):1702975.

[216] Jeong S, Heo TW, Oktawiec J, Shi R, Kang S, White JL, Schneemann A, Zaia EW, Wan LF, Ray KG, Liu Y–S, Stavila V, Guo J, Long JR, Wood BC, Urban JJ. A Mechanistic Analysis of Phase Evolution and Hydrogen Storage Behavior in Nanocrystalline $Mg(BH_4)_2$ within Reduced Graphene Oxide. ACS Nano 2020;14(2):1745–56.

[217] Wang Y, Chen X, Zhang H, Xia G, Sun D, Yu X. Heterostructures Built in Metal Hydrides for Advanced Hydrogen Storage Reversibility. Adv Mater 2020;32(31):2002647.

[218] Lai Q, Aguey–Zinsou K–F. Destabilisation of $Ca(BH_4)_2$ and $Mg(BH_4)_2$ via confinement in nanoporous Cu_2S hollow spheres. Sustainable Energy Fuels 2017;1(6):1308–19.

[219] Schneemann A, Wan LF, Lipton AS, Liu Y–S, Snider JL, Baker AA, Sugar JD, Spataru CD, Guo J, Autrey TS, Jørgensen M, Jensen TR, Wood BC, Allendorf MD, Stavila V. Nanoconfinement of Molecular Magnesium Borohydride Captured in a Bipyridine-Functionalized Metal–Organic Framework. ACS Nano 2020;14(8):10294–304.

[220] Liu BH, Li ZP. A review: Hydrogen generation from borohydride hydrolysis reaction. J Power Sources 2009;187(2):527–34.

[221] Retnamma R, Novais AQ, Rangel CM. Kinetics of hydrolysis of sodium borohydride for hydrogen production in fuel cell applications: A review. Int J Hydrogen Energy 2011;36(16):9772–90.

[222] Santos DMF, Sequeira CAC. Sodium borohydride as a fuel for the future. Ren

Sus Energy Rev 2011;15(8):3980–4001.

[223] Muir SS, Yao XD. Progress in sodium borohydride as a hydrogen storage material: Development of hydrolysis catalysts and reaction systems. Int J Hydrogen Energy 2011;36(10):5983–97.

[224] Abdelhamid HN. A review on hydrogen generation from the hydrolysis of sodium borohydride. Int J Hydrogen Energy 2021;46(1):726–65.

[225] Dragan M. Hydrogen Storage in Complex Metal Hydrides $NaBH_4$: Hydrolysis Reaction and Experimental Strategies. Catalysts 2022;12(4):356.

[226] Chrysler offers fuel cell van with soapy twist, http://www.planetark.org/dailynewsstory.cfm/newsid/13671/story.htm; 2001.

[227] Demirci UB, Akdim O, Miele AP. Ten–year efforts and a no–go recommendation for sodium borohydride for on–board automotive hydrogen storage. Int J Hydrogen Energy 2009;34(6):2638–45.

[228] Demirci UB, Akdim O, Andrieux J, Hannauer J, Chamoun R, Miele P. Sodium Borohydride Hydrolysis as Hydrogen Generator: Issues, State of the Art and Applicability Upstream from a Fuel Cell. Fuel Cells 2010;10(3):335–50.

[229] Ouyang LZ, Zhong H, Li H–W, Zhu M. A Recycling Hydrogen Supply System of $NaBH_4$ Based on a Facile Regeneration Process: A Review. Inorganics 2018;6(1):10.

[230] Nunes HX, Silva DL, Rangel CM, Pinto AMFR. Rehydrogenation of Sodium Borates to Close the $NaBH_4$–H_2 Cycle: A Review. Energies 2021;14(12):3567.

[231] Wang T, Aguey–Zinsou K–F. Direct Synthesis of $NaBH_4$ Nanoparticles from $NaOCH_3$ for Hydrogen Storage. Energies 2019;12(23):4428.

[232] Yang H, Lombardo L, Luo W, Kim W, Züttel A. Hydrogen storage properties of various carbon supported $NaBH_4$ prepared via metathesis. Int J Hydrogen Energy

2018;43(14):7108–16.

[233] Li Y, Ding X, Zhang Q. Self–Printing on Graphitic Nanosheets with Metal Borohydride Nanodots for Hydrogen Storage. Sci Rep 2016;6(1):31144.

[234] Peru F, Garroni S, Campesi R, Milanese C, Marini A, Pellicer E, Baró MD, Mulas G. Ammonia–free infiltration of $NaBH_4$ into highly–ordered mesoporous silica and carbon matrices for hydrogen storage. J Alloys Compd 2013;580:S309–12.

[235] Ampoumogli A, Steriotis T, Trikalitis P, Bardaji EG, Fichtner M, Stubos A, Charalambopoulou G. Synthesis and characterisation of a mesoporous carbon/calcium borohydride nanocomposite for hydrogen storage. Int J Hydrogen Energy 2012;37(21):16631–5.

[236] Comănescu C, Capurso G, Maddalena A. Nanoconfinement in activated mesoporous carbon of calcium borohydride for improved reversible hydrogen storage. Nanotechnology 2012;23(38):385401.

[237] Vajo JJ, Skeith SL, Mertens F. Reversible Storage of Hydrogen in Destabilized $LiBH_4$. J Phys Chem B 2005;109(9):3719–22.

[238] Nielsen TK, Bösenberg U, Gosalawit R, Dornheim M, Cerenius Y, Besenbacher F, Jensen TR. A reversible nanoconfined chemical reaction. ACS nano 2010;4(7):3903–8.

[239] Wang K, Kang X, Zhong Y, Hu C, Ren J, Wang P. Unexpected Dehydrogenation Behaviors of the $2LiBH_4$–MgH_2 Composite Confined in a Mesoporous Carbon Scaffold. J Phys Chem C 2014;118(46):26447–53.

[240] Gosalawit–Utke R, Nielsen TK, Saldan I, Laipple D, Cerenius Y, Jensen TR, Klassen T, Dornheim M. Nanoconfined $2LiBH_4$–MgH_2 Prepared by Direct Melt Infiltration into Nanoporous Materials. J Phys Chem C 2011;115(21):10903–10.

[241] Gosalawit–Utke R, Milanese C, Javadian P, Jepsen J, Laipple D, Karmi F,

Puszkiel J, Jensen TR, Marini A, Klassen T, Dornheim M. Nanoconfined $2LiBH_4$–MgH_2–$TiCl_3$ in carbon aerogel scaffold for reversible hydrogen storage. Int J Hydrogen Energy 2013;38(8):3275–82.

[242] Gosalawit–Utke R, Milanese C, Javadian P, Girella A, Laipple D, Puszkiel J, Cattaneo AS, Ferrara C, Wittayakhun J, Skibsted J, Jensen TR, Marini A, Klassen T, Dornheim M. $2LiBH_4$–MgH_2–$0.13TiCl_4$ confined in nanoporous structure of carbon aerogel scaffold for reversible hydrogen storage. J Alloys Compd 2014;599:78–86.

[243] Utke R, Thiangviriya S, Javadian P, Jensen TR, Milanese C, Klassen T, Dornheim M. $2LiBH_4$–MgH_2 nanoconfined into carbon aerogel scaffold impregnated with $ZrCl_4$ for reversible hydrogen storage. Mater Chem Phys 2016;169:136–41.

[244] Ding Z, Zhao X, Shaw LL. Reaction between $LiBH_4$ and MgH_2 induced by high–energy ball milling. J Power Sources 2015;293:236–45.

[245] Ding Z, Lu Y, Li L, Shaw L. High reversible capacity hydrogen storage through Nano–$LiBH_4$ + Nano–MgH_2 system. Energy Storage Mater 2019;20:24–5.

[246] Ding Z, Li H, Shaw L. New insights into the solid-state hydrogen storage of nanostructured $LiBH_4$–MgH_2 system. Chem Eng J 2020;385:123856.

[247] Xia G, Tan Y, Wu F, Fang F, Sun D, Guo Z, Huang Z, Yu X. Graphene–wrapped reversible reaction for advanced hydrogen storage. Nano Energy 2016;26:488–95.

[248] Dansirima P, Thiangviriya S, Plerdsranoy P, Utke O, Utke R. Small hydrogen storage tank filled with $2LiBH_4$–MgH_2 nanoconfined in activated carbon: Reaction mechanisms and performances. Int J Hydrogen Energy 2019;44(21):10752–62.

[249] Plerdsranoy P, Utke R. Ternary $LiBH_4$–MgH_2–$NaAlH_4$ hydride confined into nanoporous carbon host for reversible hydrogen storage. J Phys Chem Solids 2016;90:80–6.

[250] Gao M, Gu J, Pan H, Wang Y, Liu Y, Liang C, Guo Z. $Ca(BH_4)_2$–$LiBH_4$–MgH_2:

a novel ternary hydrogen storage system with superior long-term cycling performance. J Phys Chem A 2013;1(39):12285–92.

[251] Zheng J, Yao Z, Xiao X, Wang X, He J, Chen M, Cheng H, Zhang L, Chen L. Enhanced hydrogen storage properties of high–loading nanoconfined $LiBH_4$–$Mg(BH_4)_2$ composites with porous hollow carbon nanospheres. Int J Hydrogen Energy 2021;46(1):852–64.

[252] Zhao–Karger Z, Witter R, Bardají EG, Wang D, Cossement D, Fichtner M. Influence of Nanoconfinement on Reaction Pathways of Complex Metal Hydrides. Energy Procedia 2012;29:731–7.

[253] Javadian P, Jensen TR. Enhanced hydrogen reversibility of nanoconfined $LiBH_4$–$Mg(BH_4)_2$. Int J Hydrogen Energy 2014;39(18):9871–6.

[254] Javadian P, Sheppard DA, Buckley CE, Jensen TR. Hydrogen storage properties of nanoconfined $LiBH_4$–$NaBH_4$. Int J Hydrogen Energy 2015;40(43):14916–24.

[255] Roedern E, Hansen BRS, Ley MB, Jensen TR. Effect of Eutectic Melting, Reactive Hydride Composites, and Nanoconfinement on Decomposition and Reversibility of $LiBH_4$–KBH_4. J Phys Chem C 2015;119(46):25818–25.

[256] Peru F, Payandeh S, Charalambopoulou G, Jensen TR, Steriotis T. Hydrogen Sorption and Reversibility of the $LiBH_4$–KBH_4 Eutectic System Confined in a CMK–3 Type Carbon via Melt Infiltration. J Carbon Res 2020;6(2):19.

[257] Javadian P, Sheppard DA, Buckley CE, Jensen TR. Hydrogen storage properties of nanoconfined $LiBH_4$–$Ca(BH_4)_2$. Nano Energy 2015;11:96–103.

[258] Plerdsranoy P, Utke R. Confined $LiBH_4$–$LiAlH_4$ in nanopores of activated carbon nanofibers. Int J Hydrogen Energy 2015;40(22):7083–92.

[259] Javadian P, Sheppard DA, Buckley CE, Jensen TR. Hydrogen Desorption Properties of Bulk and Nanoconfined $LiBH_4$–$NaAlH_4$. Crystals 2016;6(6):70.

[260] Chen P, Xiong Z, Luo J, Lin J, Tan KL. Interaction of hydrogen with metal nitrides and imides. Nature 2002;420(6913):302-4.

[261] Xiong Z, Wu G, Hu J, Chen P. Ternary Imides for Hydrogen Storage. Adv Mater 2004;16(17):1522–5.

[262] Luo W. ($LiNH_2$–MgH_2): a viable hydrogen storage system. J Alloys Compd 2004;381(1):284–7.

[263] Chu H, Xiong Z, Wu G, He T, Wu C, Chen P. Hydrogen storage properties of Li–Ca–N–H system with different molar ratios of $LiNH_2$/CaH_2. Int J Hydrogen Energy 2010;35(15):8317–21.

[264] Xiong Z, Wu G, Hu J, Liu Y, Chen P, Luo W, Wang J. Reversible Hydrogen Storage by a Li–Al–N–H Complex. Adv Funct Mater 2007;17(7):1137–42.

[265] Hu J, Xiong Z, Wu G, Chen P, Murata K, Sakata K. Hydrogen releasing reaction between $Mg(NH_2)_2$ and CaH_2. J Power Sources 2006;159(1):116–9.

[266] Pinkerton FE, Meisner GP, Meyer MS, Balogh MP, Kundrat, MD. Hydrogen Desorption exceeding ten weight percent from the new quaternary hydride $Li_3BN_2H_8$. J Phys Chem B 2005;109(1):6–8.

[267] Chen P, Xiong Z, Wu G, Liu Y, Hu J, Luo W. Metal–N–H systems for the hydrogen storage. Scr Mater 2007;56(10):817–22.

[268] Ichikawa T, Isobe S, Hanada N, Fujii H. Lithium nitride for reversible hydrogen storage. J Alloys Compd 2004;365(1):271–6.

[269] Yamane A, Shimojo F, Hoshino K, Ichikawa T, Kojima Y. Cluster size effect on hydrogen desorption process from Li_nH_n–NH_3 hydrogen storage system. J Alloys Compd 2011;509S:S728–31.

[270] Seip TAT, Olsen RA, Løvvik OM. Surfaces and Clusters of $Mg(NH_2)_2$ Studied by Density Functional Theory Calculations. J Phys Chem C 2009;113(52):21648–56.

[271] Shaw LL, Ren RM, Markmitree T, Osborn W. Effects of mechanical activation on dehydrogenation of the lithium amide and lithium hydride system. J Alloys Compd 2008;448:263–71.

[272] Yao JH, Shang C, Aguey–Zinsou KF, Guo ZX. Desorption characteristics of mechanically and chemically modified $LiNH_2$ and ($LiNH_2$+LiH). J Alloys Compd 2007;432(1):277–82.

[273] Osborn W, Markmaitree T, Shaw LL, Hu J–Z, Kwak J, Yang Z. Low temperature milling of the $LiNH_2$+LiH hydrogen storage system. Int J Hydrogen Energy 2009;34(10):4331–9.

[274] Varin RA, Jang M, Polanski M. The effects of ball milling and molar ratio of LiH on the hydrogen storage properties of nanocrystalline lithium amide and lithium hydride ($LiNH_2$+LiH) system. J Alloys Compd 2010;491(1):658-67.

[275] Varin RA, Jang M. The effects of graphite on the reversible hydrogen storage of nanostructured lithium amide and lithium hydride ($LiNH_2$+1.2LiH) system. J Alloys Compd 2011;509(25):7143–51.

[276] Yang J, Li D, Fu H, Xin G, Zheng J, Li X. In situ hybridization of $LiNH_2$–LiH–$Mg(BH_4)_2$ nano-composites: intermediate and optimized hydrogenation properties. Phys Chem Chem Phys 2012;14(8):2857–63.

[277] Xia G, Li D, Chen X, Tan Y, Tang Z, Guo Z, Liu H, Liu Z, Yu X. Carbon–coated Li_3N nanofibers for advanced hydrogen storage. Adv Mater 2013;25(43):6238–44.

[278] Wood BC, Stavila V, Poonyayant N, Heo TW, Ray KG, Klebanoff LE, Udovic TJ, Lee JRI, Angboonpong N, Sugar JD, Pakawatpanurut P. Nanointerface–Driven Reversible Hydrogen Storage in the Nanoconfined Li–N–H System. Adv Mater Interfaces 2017;4(3):1600803.

[279] Xiong Z, Hu J, Wu G, Chen P, Luo W, Gross K, Wang J. Thermodynamic and

kinetic investigations of the hydrogen storage in the Li–Mg–N–H system. J Alloys Compd 2005;398(1):235–9.

[280] Liang C, Liu Y, Fu H, Ding Y, Gao M, Pan H. Li–Mg–N–H-based combination systems for hydrogen storage. J Alloys Compd 2011;509(30):7844–53.

[281] Liu Y, Zhong K, Luo K, Gao M, Pan H, Wang Q. Size–dependent kinetic enhancement in hydrogen absorption and desorption of the Li-Mg-N-H system. J Am Chem Soc 2009;131(5):1862–70.

[282] Xie L, Liu Y, Li G, Li X. Improving Hydrogen Sorption Kinetics of the $Mg(NH_2)_2$−LiH System by the Tuning Particle Size of the Amide. J Phys Chem C 2009;113(32):14523–7.

[283] Xia G, Tan Y, Li D, Guo Z, Liu H, Liu Z, Yu X. Hierarchical Porous $Li_2Mg(NH)_2$@C Nanowires with Long Cycle Life Towards Stable Hydrogen Storage. Sci Rep 2014;4(1):6599.

[284] Xia G, Chen X, Zhao Y, Li X, Guo Z, Jensen CM, Gu Q, Yu X. High–Performance Hydrogen Storage Nanoparticles Inside Hierarchical Porous Carbon Nanofibers with Stable Cycling. ACS Appl Mater Interfaces 2017;9(18):15502–9.

[285] Xia G, Chen X, Zhou C, Zhang C, Li D, Gu Q, Guo Z, Liu H, Liu Z, Yu X. Nano–confined multi–synthesis of a Li–Mg–N–H nanocomposite towards low–temperature hydrogen storage with stable reversibility. J Phys Chem A 2015;3(24):12646–52.

Table 1

Synthesis process and hydrogen storage properties of nanostructured MgH_2/Mg

Synthesis process	Raw materials	Particle size	Desorption temperature (°C)	ΔH (kJ·mol^{-1} H_2)	E_a (kJ·mol^{-1})	Hydrogen desorption performance	Hydrogen absorption performance	Cycle number	Capacity retention (%)	Ref.
	bulk MgH_2	20–30 µm	> 300	70~78	140–160	5 wt.%–2000 s–350 ºC	3 wt.%–2000 s–300 °C–10 bar			[48,49]
Mechanical milling	MgH_2	> 100 nm	T_{peak} = 380		des: 120	7 wt.%–600s–350 °C	7 wt.%–6.5 min–300 °C–10 bar			[51]
Mechanical milling	2LiH+$MgCl_2$	7 nm	ΔT_{eq} = 6 (1 bar H_2)	des: 71.22 ± 0.49						[54]
Mechanical milling	2LiH+$MgCl_2$ with graphene nanosheets	3 nm	T_{onset} = 255 T_{peak} = 350		des: 118.9	5.1 wt.%–20 min –325 °C	5.2 wt.%–10 min –250 °C–20 bar	5	100	[55]
Ultrasound–driven liquid–solid phase metathesis	2LiH+$MgCl_2$	4–5 nm	T_{onset} = 30 T_{peak} = 84 T_{eq} = 215 (1 bar H_2)	des: 59.5	abs: 28 des: 80	6.7 wt.%–60 h–30 ºC	6.7 wt.%–360 min–30 °C–30 bar	50	99.3	[56]
Thermal reduction	Bu_2Mg under H_2 atmosphere	30 nm	T_{peak} = 355			6.8 wt.%–2 h –250 ºC				[59]

Thermal reduction	Cp_2Mg with potassium biphenyl	25–38 nm			abs: 115–122 des: 126–160	6.2 wt.%–5 min–375 ºC	6.5 wt.%–60 s–300 °C–10 bar			[62]
Thermal reduction	Bu_2Mg with lithium	8 nm	T_{peak} = 355	abs: 63.5 ± 1.8		5 wt.%–100 min–300 ºC	0.9 wt.%–5 h–120 °C –30 bar			[63]
Thermal reduction	Bu_2Mg with calcium	0.4–4 µm/40 nm	T_{peak} = 360	abs: 67.6 ± 5.3 des: 103.1 ± 2.7		2.4 wt.% –200 min–350 ºC	2.3 wt.% H_2–20 min–300 °C–30 bar			[64]
Vapor deposition	Mg	30–170 nm		des: 65.3	abs: 33.5 des: 38.8	3.28 wt.%–30 min–300 ºC	2.93 wt.%–30 min–200 °C–20 bar	50	100	[65]
Thermal evaporation deposition	Mg	30 µm				6 wt.%–140 min–350 ºC	6 wt.%–200 min–350 °C–10 bar			[71]
Vacuum evaporation deposition	Mg	30 µm/5 cm				7.5 wt.%–100 min–350 ºC	6 wt.%–70 min–350 °C–10 bar			[72]
	Mg	380–800 nm		abs: 60.7±6. des: 71±4.2						[74]

Wet impregnation and thermal decomposition	di–n–butylmagnesium ordered mesoporous silica (SBA-15)	5–10 nm	T_{onset} = 127 T_{peak} = 267			3 wt.%–20 h–350 ºC				[94]
Wet impregnation and thermal decomposition	$MgCp_2$ and MOF(SNU–90)	44–88 nm					0.15 wt.% H_2–40 min–52 °C–80 bar			[95]
Wet impregnation and thermal reduction	Bu_2Mg Nanoporous scaffold	22 nm	T_{onset} = 175 T_{peak} = 368							[96]
Melt infiltration	MgH_2 Carbon Aerogels	< 20 nm	T_{onset} = 140 T_{peak} = 368				1.5 wt.%–15 min–300 °C–18 bar	4	100	[97]
Wet impregnation and thermal reduction	Bu_2Mg activated carbon fibre	< 3 nm	T_{peak} = 325	abs: 63.8±0.5	des: 142.8±2	5 wt.%–210 min–290 ºC				[102]
Wet impregnation and thermal reduction	Bu_2Mg ordered mesoporous carbon	1-2 nm	T_{onset} = 50 T_{peak} = 350 T_{eq} = 250 (1 bar H_2)	abs: 55.4±3.1	des: 125.3±1.5	5.5 wt.%–8 h–300 ºC	4 wt.%–7 min–300 °C–20 bar	4	100	[103]
Wet impregnation and thermal reduction	Bu_2Mg N doped CMK–3/Ni doped CMK-3	4.5-10 nm	T_{onset} = 50 T_{peak} = 350		N–des: 116.2±1.8 Ni–des: 107.6±1.2	N–doped: 5 wt.%–1 h–300 °C Ni–doped: 7.5 wt.%–2 h–300 °C	Ni: 6.5 wt.%–2 h at 200 °C–20 bar. N: 7.5 wt.%–2 h–200 °C–20 bar.			[104]

Wet impregnation and thermal reduction	Bu_2Mg Mesoporous CoS nano–boxes scaffold	5–10 nm	T_{peak} = 305	abs: 65.6 ± 1.1 des: 68.1 ± 1.4	abs: 57.4 ± 2.2 des: 120.8 ± 3.2	1.67 wt.%–1000 s–300 ºC	1.67 wt.%–2 h–175 °C–32 bar			[105]
Solvothermal method	Bu_2Mg Ni–Graphene	5.7 nm	T_{peak} = 201		abs: 22.7 des: 64.7	5.4 wt.%–30 min–250 ºC	5.4 wt.%–10 min –200 °C–30 bar	100	99.2	[106]
Solvothermal method	Cp_2Mg lithium naphthalenide Reduced graphene oxide	3–4 nm			abs: 60.8 des: 92.9	6 wt.%–60 min–300 ºC	6.5 wt.%–2 h–200 °C–15 bar	25	100	[107]
Solvothermal method	Cp_2Mg lithium naphthalenide PMMA	~5 nm		abs: 25 des: 79		4 wt.%–60 min–200 ºC	5.97 wt.%–30 min–200 °C–35 bar			[108]
Laser–assisted ablation	Mg PMMA	< 7 nm				5 wt.%–30 min–250 ºC	5.5 wt.%–20 min–250 °C–25 bar			[109]
Solvothermal method	Bu_2Mg carbon nanotubes	5–10 nm	T_{onset} = 220 T_{peak} = 350	des: 74.99	abs: 68.92 des: 97.97	5.5 wt.%–30 min–300 ºC	5.79 wt.%–5 min–250 °C–80 bar	10	100	[110]

Table 2

Synthesis process and hydrogen storage properties of nanostructured $NaAlH_4$ and $LiAlH_4$.

Synthesis process	Raw materials	Particle size	Desorption temperature (°C)	ΔH (kJ·mol^{-1} H_2)	E_a (kJ·mol^{-1})	Hydrogen desorption performance	Hydrogen absorption performance	Cycle number	Capacity retention (%)	Ref.
	bulk $NaAlH_4$	1–5 μm	T_{onset} = 178	1 step: 39.9 2 step: 48.5	1 step: 116.2 2 step: 149.3	0.2 wt.%–180 min–150 °C				[113, 116]
Mechanical milling	$NaAlH_4$	> 100 nm				3 wt.%–120 min–160 °C	4 wt.%–2 h–130 °C–90 bar			[118]
Wet impregnation	$NaAlH_4$ in THF carbon nanofiber	2-10 nm	T_{peak} = 70		58					[121]
Wet impregnation	$NaAlH_4$ in THF mesoporous carbon	< 2 μm	T_{onset} = 160	1 step: 19.9 2 step: 17.3	1 step: 88 ± 10 2 step: 99 ± 21 3 step: 136 ± 8	25~250 °C, 4.4 wt.%				[123]
Wet impregnation	$NaAlH_4$ in THF Ordered mesoporous silica	~10 nm	T_{onset} = 160 T_{peak} = 175			3 wt.%–60 min–180 °C	2 wt.%–1 h–180 °C–55 bar			[125]

Melt infiltration	$NaAlH_4$ Carbon aerogels	4–100 nm	T_{onset} = 75 T_{peak} = 171		30~140 °C–3.5 wt.%		4	53.8	[127]
Melt infiltration	$NaAlH_4$ $TiCl_3$ doped carbon aerogels	17 nm	T_{onset} = 33 T_{peak} = 125		25~170 °C–2.8 wt.%	2 wt.%–10 h–160 °C–100 bar	4	54	[128]
Melt infiltration	$NaAlH_4$ ordered mesoporous carbon	~3.5 nm		46 ± 5	5.1 wt.%–40 min–190 °C	4.8 wt.%–10 h–150 °C–70 bar	15	80	[129]
Wet impregnation	$NaAlH_4$ in THF with N–doped ordered mesoporous carbon	1–2 nm	T_{onset} <50 T_{peak} = 80	1 step: 114.2 2 step: 121					[130]
Melt infiltration	$NaAlH_4$ Uniform porous carbon	4 nm	T_{onset} = 100 T_{peak} = 153	69.7 ± 3.8	25~170 °C–3.9 wt.%	3.5 wt.%–6 h–120 °C–110 bar	4	90	[132]
Melt infiltration	$NaAlH_4$ Ti–doped CO_2–activated aerogels	< 20 nm	T_{onset} = 25 T_{peak} = 91		30~175 °C–4.5 wt.%	3.5 wt.%–10 h–160 °C–90–93 bar	4	65.8	[133]
Wet impregnation	$NaAlH_4$/$LiAlH_4$ in THF with carbon nanotubes	~10 nm	T_{onset} = 60/25 T_{peak} = 220/120	45 ± 2					[137]
Wet impregnation	$NaAlH_4$ in THF with graphene nanosheets	12.4 nm	T_{onset} = 100 T_{peak} = 153	68.23	5.6 wt.%–40 min–160 °C		20	98	[138]
Melt infiltration	$NaAlH_4$ CeO_2 hollow nanotubes	< 50 nm	T_{onset} = 75 T_{peak} = 130	76.32	5.09 wt.%–30 min–180 °C				[141]

Wet impregnation	$NaAlH_4$ in THF with nanoporous Raney Ni	3 nm	T_{onset} = 85 T_{peak} = 130	20	3.7 wt.% –20 min–180 °C	3 wt.%–8 h–150 °C–70 bar	15	60	[142]
Melt infiltration	$NaAlH_4$ Titanium–doped MOF	1–10 nm	T_{onset} = 50	57.4 ± 2.4	3.5 wt.%–150 min–180 °C	3.9 wt.%–2 h–150 °C–105 bar	4	87	[144]
Wet impregnation	$LiAlH_4$(liquid) Ni–doped mesoporous carbon scaffold	1 nm	T_{onset} = 66 T_{peak} = 154	39.67	3.68 wt.%–20 min–180 °C				[145]
Wet impregnation	$LiAlH_4$ in THF TiO_2 porous carbon	< 100 nm	T_{onset} = 64 T_{peak} = 115	47.1 ± 3.5	4.3 wt.%–40 min–130 °C				[146]
Wet impregnation	$LiAlH_4$ in ethyl ether N–doped CMK–3	<10 nm	T_{onset} = 126						[148]

Table 3

Synthesis process and hydrogen storage properties of nanostructured $LiBH_4$

Synthesis process	Raw materials	Particle size	Desorption temperature (°C)	E_a ($kJ \cdot mol^{-1}$)	Hydrogen desorption performance	Hydrogen absorption performance	Cycle number	Capacity retention (%)	Ref.
	bulk $LiBH_4$	50 μm	T_{peak} = 495	156 ± 20	1 wt.%–350 min–300 °C	2.7 wt.%–350 min–350 °C–100 bar	5	~15.4	[161,162,197]
Melt infiltration	$LiBH_4$ nanoporous carbon scaffolds	13/25 nm	T_{onset} = 230 T_{peak} = 381	103 ± 4	300 °C, 12.5 wt.%/h		3	>50	[163]
Wet impregnation	$LiBH_4$ in THF with activated carbon scaffolds	< 5 nm	T_{onset} = 220 T_{peak} = 300		250–300 °C, 9 wt.%/h	6.6 wt.%–24 h–300 °C–50 bar	2	~50	[164]
Wet impregnation	$LiBH_4$ in MTBE with Mesoporous carbon scaffolds	~4 nm	T_{onset} = 200 T_{peak} = 335		3.4 wt.%–90 min–300 °C				[165]
Wet impregnation	$LiBH_4$ in THF with ordered mesoporous silica	6.7 nm	T_{onset} = 45 T_{peak} = 92		8.5 wt.%–10 min–105 °C				[167]
Melt infiltration	$LiBH_4$ Micro/mesoporous aerogel-like carbon	< 9 nm	T_{onset} = 200 T_{peak} = 310			3 wt.%–3 h–300 °C–100 bar			[169]

Melt infiltration	$LiBH_4$ Activated carbon nanofiber	<20 nm	T_{onset} = 275 T_{peak} = 305				4	50	[171]
Melt infiltration	$LiBH_4$ Carbon nanocages	< 30 nm	T_{onset} = 200 T_{peak} = 320	113.5	4.4wt.%–500 s–400 °C	3.5 wt.%–1000 s–400 °C–50 bar	4	78	[172]
Melt infiltration	$LiBH_4$ Porous hollow carbon nanospheres	< 30 nm	T_{onset} = 200 T_{peak} = 356	93.9	8.1 wt.%–25 min–350 °C	4.3 wt.%–5 min–400 °C–100 bar	5	63	[174]
Melt infiltration	$LiBH_4$ Double–layered carbon nanobowl	< 100 nm	T_{onset} = 225 T_{peak} = 353	121.4	9 wt.%–20 h–350 °C	7 wt.%–200 min–300 °C–100 bar			[175]
Solid-gas reaction and solid-liquid reaction	C_4H_9Li+H_2+B_2H_6 graphene	~4 nm	T_{onset} = 200 T_{peak} = 346	119.6	9.7 wt.%–60 min–340 °C		5	80	[176]
Solvothermal	C_4H_9Li+H_2+$C_6H_{15}NBH_3$ Ni–graphene	5–10 nm	T_{onset} = 130 T_{peak} = 285	106	9.2 wt.%–175 min–300 °C	9.2 wt.%–200 min–300 °C–100 bar	100	92.4	[177]
Wet impregnation	$LiBH_4$ in THF with Ti_3C_2 MXene		T_{onset} = 172.6 T_{peak} = 322.8	94.44	9.6 wt.%–1 h–380 °C	6.5 wt.%–24 h–300 °C–95 bar	3	52	[179]
Wet impregnation	$LiBH_4$ in THF with porous TiO_2	< 12 nm	T_{onset} = 220 T_{peak} = 330		4.0 wt.%–30 min–350 °C	2.1 wt.%–60 min–400 °C–46 bar			[181]
Melt infiltration	$LiBH_4$ Core–shell nano–TiO_2 decorated porous amorphous carbon	< 10 nm	T_{onset} = 224 T_{peak} = 318	91.5	7.3 wt.%–60 min–350 °C		20	61	[182]
Melt infiltration	$LiBH_4$ Porous carbon wrapped Fe_3O_4 skeleton	< 50 nm	T_{onset} = 175 T_{peak} = 325	108.1	7.8 wt.%–30 min–350 °C	7.6 wt.%–60 min–450 °C–100 bar	20	80	[183]

Wet impregnation	$LiBH_4$ in THF with Hierarchical porous $ZnO/ZnCo_2O_4$ nanoparticles	< 3 nm	T_{onset} = 169 T_{peak} = 275	120.22	7.8 wt.%–30 min–350 °C				[184]
Wet impregnation	$LiBH_4$ in THF with porous $NiMnO_3$ microspheres	< 5 nm	T_{onset} = 150 T_{peak} = 300	129.8	2.8 wt.%–60 min–300 °C				[185]
Wet impregnation	$LiBH_4$ in THF with nanoporous Ni–based alloy	< 5 nm	T_{onset} = 70	11.4	9.4 wt.%–5 min–300 °C	8 wt.%–600 min–450 °C–80 bar	2	98	[189]
Melt infiltration	$LiBH_4$ Activated carbon modified by CeF_3		T_{onset} = 170 T_{peak} = 320	108	11.8 wt.%–500 s–350 °C		4	79	[193]
Solvothermal	$C_4H_9Li+H_2+C_6H_{15}NBH_3$	50-60 nm	T_{onset} = 190	147 ± 2.2	11.3 wt.%–300 min–350 °C	12 wt.%–350 min–400 °C–100 bar	5	75	[197]
Mechanical milling	$2LiBH_4+MgCl_2$	> 100 nm	T_{onset} = 120 T_{peak} = 352	120.01	5.5 wt.%–250 min–350 °C		4	70	[204]
Mechanical milling	$2NaBH_4+MgCl_2$		T_{onset} = 227 T_{peak} = 365		14.4 wt.%–25~527 °C	6.1 wt.%–350 min–270 °C–400 bar			[205]
Wet impregnation	$Mg(BH_4)_2$ in diethyl ether with activated carbon composites	< 2 nm	T_{onset} = 150 T_{peak} = 317	176	6 wt.%–170~500 °C				[207]
Wet impregnation	$Mg(BH_4)_2$ with Ni–CMK3 nanoscaffold	< 3 nm	T_{onset} = 75 T_{peak} =155	16.18	4.5 wt.%–40 min–155 °C				[209]

Wet impregnation	$Mg(BH_4)_2$ in THF with Ni-mesoporous carbon	< 3 nm	T_{onset}=44 T_{peak}= 141	21.3	6 wt.%–20 min–350 °C		[210]
Mechanical milling	MgH_2+B_2H_6 Carbon		T_{onset} = 100 T_{peak} = 160	102 ± 6		30%–270 °C–150 bar	[212]
Solvent method	$Mg(BH_4)_2$ Carbon nanotubes	2-6 nm	T_{onset} = 76 T_{peak} = 117	14.36	3.79 wt.%–10 min–117 °C	2.5 wt.%–10 h–350 °C–100 bar	[213]
Mechanical milling	2$NaBH_4$+$MgCl_2$ Carbon nanotubes	30-50 nm	T_{onset} = 120 T_{peak} = 150	130.2	6.04 wt.%–2000 s–300 °C	2.46 wt.%–2 h–300 °C–120 bar	[214]

Table 4

Synthesis strategies and hydrogen storage properties of nanostructured metal-N-H combination systems.

Synthesis process	Raw materials	Particle Size	Desorption temperature (°C)	ΔH ($kJ\cdot mol^{-1}\cdot H_2$)	Ea ($kJ\cdot mol^{-1}$)	Hydrogen desorption performance	Hydrogen absorption performance	Cycle number	Capacity retention (%)	Ref.
Hand milling	$LiNH_2$+LiH	>50 μm	T_{peak} = 308	65.6	163.76	200–450 °C, 8.1 wt.%				[271]
Mechanical milling	$LiNH_2$+1.2LiH	~10 nm	T_{onset}=183.4 T_{peak}=239.2	62.4	57.5					[272-275]
Plasma metal reaction and nucleation growth	2Li+NH_3+LiH+$NaBH_4$+$MgCl_2$+ diethyl ether	200–400 nm	T_{onset}=105 T_{peak}=150	1 step: 8.4 ± 0.3 2 step: 39.4 ± 0.6 3 step: 32.4 ± 1.2	1 step: 60.7 ± 4.2 2 step: 17.8 ± 1.6 3 step: 19.0 ± 1.1			3	86	[276]
Electrospinning	Li_3N+$2H_2$	100 nm	T_{onset}=100 T_{peak}=250	65	25.07	7.4 wt.%–120 min–200 °C	8 wt.%–10 min–200 °C–35 bar	10	73	[277]
Wet impregnation and thermal reduction	Li + NH_3 Nanoporous carbon	<3 nm	T_{onset}=150				2 wt.%–10 min–250 °C–100 bar	10	100	[278]

Mechanical milling	$1Mg(NH_2)_2$–$2LiNH_2$	100–200 nm	T_{onset}=150		51.6	50 %–159 min–160 ℃	4 wt.%–50 min–227 ℃–80 bar			[281,282]
Electrospinning and thermal reduction	NH_4MgCl_3+LiN_3+H_2 Carbon nanowires	4 nm	T_{onset}=78 T_{peak}=113		24.5	5.5 wt.%–60 min–135 ℃		20	94.6	[283]
Electrospinning, thermal reduction and wet impregnation	$Mg(C_4H_9)_2$+$2H_2$+$2NH_3$+Li_3N Carbon nanofibers	4.2 nm	T_{onset}=80 T_{peak}=118	35.7 ± 0.5	37.2	4.5 wt.%–40 min–135 ℃	4 wt.%–20 min–135 ℃–30 bar	50	100	[284]
Wet impregnation and thermal decomposition	$3LiN_3$+$MgCl_2$+H_2+2,2–trifluoroethanol Double–shelled hollow carbon spheres	9 nm	T_{onset}=90 T_{peak}=123		47.5	5 wt.%–60 min–135 ℃	4.2 wt.%–20 min–135 ℃–35 bar	20	91	[285]